6. ENGINEERING OPTIONS

Mark S. Tillack
Charles G. Bathke
Michael Billone
James P. Blanchard
Leslie Bromberg
Thomas J. Dolan
Laila A. El-Guebaly
J. Stephen Herring
Hesham Y. Khater
Farrokh Najmabadi
Alexei L. Radovinsky
Robert Schleicher
Dai-Kai Sze
Lester M. Waganer
Clement P. C. Wong

Contents

6.1. INTRODUCTION 6-1

6.2. FERRITIC STEEL DESIGNS 6-2

6.2.1. Overview 6-2

6.2.2. Design Options 6-3

6.2.3. Material Properties 6-5

6.2.4. Ability to Meet Requirements 6-12

6.2.5. Key Issues and R&D Needs 6-26

6.3. VANADIUM DESIGNS 6-33

6.3.1. Overview 6-33

6.3.2. Design Options 6-34

6.3.3. Material Properties 6-58

6.3.4. Ability to Meet Demo Requirements 6-68

6.3.5. Key Issues and R&D Needs 6-71

6.4. SILICON-CARBIDE COMPOSITE DESIGNS 6-78

6.4.1. Design Options 6-78

6.4.2. Key Issues 6-79

6.5. MAGNET SYSTEMS 6-80

6.5.1. PF Fault Analysis 6-80

6.5.2. TF Fault Analysis 6-83

6.5.3. Cryostat and Dewar Design 6-86

6.5.4. Structural Effects of Large Access Port 6-92

6.6. SUMMARY AND CONCLUSIONS 6-100

REFERENCES 6-102

6. ENGINEERING OPTIONS

6.1. INTRODUCTION

Through its successful operation, the U.S. Fusion Demo must be sufficiently convincing that a utility or independent power producer will choose to purchase one as its next electricity generating plant. A fusion power plant which is limited to the use of presently-proven technologies is unlikely to be sufficiently attractive to a utility unless fuel shortages and regulatory restrictions are far more crippling to competing energy sources than currently anticipated. In that case, the task of choosing an appropriate set of engineering technologies today involves trade-offs between attractiveness and technical risk. In general, more advanced concepts appear more attractive but entail critical issues which must be addressed through R&D programs prior to a commitment to construct the Demo.

The Starlite project has assembled a set of requirements for commercial power plants based on projections of customer needs 25-50 years from now. Based on these, a clear and self-consistent definition of a Demo power plant has been identified (see Sec. 1). The Demo requirements provide goals for engineering components which are very challenging to meet. Safety and environmental requirements severely limit material choices. Performance requirements provide strong incentives to operate at high coolant outlet temperature. Reliability requirements may be the most difficult to meet. Design solutions must be simple, incorporate adequate performance margins, and be tested fully prior to Demo operation.

The range of design options for fusion power plants is limited, and has been examined in numerous studies during the past 25 years. Previous studies have shown that advanced low-activation ferritic steel, vanadium alloy, or SiC/SiC composites are the most credible candidates for the primary in-vessel structural material. An assessment of engineering design options has been performed using these three materials and the associated in-vessel component designs which are compatible with them.

The choice of structural material constrains many aspects of the designs. These assessments include consideration of all design aspects related to the choice of structural material, and not only the characteristics of the structural material itself. Material choices for the structures, breeder and multiplier, shield, and coolants are all considered.

Special attention is given to the first wall, blanket, shield, divertor, magnets, and the support systems required to operate them. For each class of designs, their ability to meet the Demo requirements is summarized and the key issues are assessed.

In principle, the ability to meet the mission requirements is the only important attribute for determining the attractiveness of a design concept. However, fusion is still in a developmental stage in which large uncertainties remain in the performance predictions, particularly for those concepts which offer the greatest potential for a more attractive product. In addition, some conceptual designs are forced to extrapolate from the existing database or project future improvements in order to obtain performance levels which are expected to provide a sufficiently attractive product. Therefore, it is essential for any comprehensive assessment to include consideration of the critical issues which, if not resolved successfully, will lead to the concept failing to meet its mission requirements. In some cases, the remaining uncertainties are so large that a self-consistent design may be impossible, given the basic system parameters which characterize tokamak power plant operation. In other cases, the power plant would likely operate, but under reduced performance levels, reduced lifetime, or uncompetitive cost.

The goal of the Starlite assessments is to identify the design option which meets the minimum requirements with the lowest uncertainty in fulfilling the mission of Demo.

6.2. FERRITIC STEEL DESIGNS

6.2.1. Overview

Unlike vanadium alloys and SiC composites, ferritic steel is compatible with several different coolants, and can be used effectively with either solid ceramic breeders or liquid metals. Steel is by far the most developed material option. Intimate knowledge of the limitations of this class of alloys must be balanced against the uncertainties which exist in the behavior of V-alloys and SiC/SiC composites.

Four aspects of the top-level mission requirements have been given special attention in the assessment: maintainability, thermal conversion efficiency and performance limitations (which impact cost), the trade-off between material costs and performance, and activation. These were determined to be most significant as discriminators between the various design options.

Two key issues were selected for special attention: consequences of the loss of ductility and ferromagnetism effects. Ductility under irradiation is viewed as the most serious

unknown. Ferromagnetism causes important operational problems, but these were viewed as solvable if an appropriate R&D program were carried out.

The results of the assessment indicate that ferritic steel remains a potential power plant structural material within a certain restricted range of performance. The requirements for waste disposal are likely to be met with low-activation variants of ferritic steel, such that this was not considered to be a major discriminating factor. Its ability to meet the minimum requirement for competitive cost of electricity is one of the most serious concerns. The relatively restricted temperature range of operation and relatively low thermal conductivity limit the fusion core power density and the net plant conversion efficiency, leading to larger machines with more restrictive power density limits. In addition, it is highly unlikely that steel could be used in the divertor unless the heat flux can be maintained much lower than current projections. In that case, an alternate technology must be identified, further complicating the system. Safety implications of ferritic steel were not adequately assessed, and should be given special attention in future studies.

Ferritic steel components have fewer critical issues as compared with other material candidates. However, the loss of ductility under irradiation is potentially a feasibility issue. Existing irradiation experiments performed in the temperature range of 250–400 °C in mixed-spectrum reactors result in ductile-to-brittle transition temperature (DBTT) values of about 250 °C under conditions with simultaneous neutron damage and helium generation. Similar testing in fast reactors at $T \geq 365$ °C with neutron damage, but very little helium production, results in DBTT less than 0 °C for some alloys. Without fully understanding the role of He in raising the DBTT, it is difficult to extrapolate these results to a fusion spectrum which is characterized by about 10 appm-He/dpa at the plasma surface of the first wall. What is clear, however, is that special precautions would be required if ferritic steels embrittle in a fusion reactor as they do in a mixed-spectrum reactor and the risk of failure may be significantly higher in power plants which use a brittle structural material.

6.2.2. Design Options

During the time period of 1975–1990, ferritic steels were a leading candidate for the structural material in U.S. fusion power plant conceptual design studies (*e.g.,* Blanket Selection and Comparison Study, BCSS [1]). These alloys were considered attractive materials for use with solid-breeder ceramics and helium coolants, although they are compatible as well with water and liquid-metal coolants. Since that time, U.S. conceptual design studies (*e.g.,* ARIES [2, 3]) have evolved towards higher temperature, lower

activation structural materials such as vanadium alloys and SiC composites. This trend has been encouraged by the programmatic impetus to fully exploit the inherent safety and environmental potential of fusion, as well as to deliver an economically more competitive product.

Ferritic steels remain the leading structural material in European and Japanese conceptual design studies and R&D programs. Both groups are committed to ferritic steels, and they have developed their own special alloys for fusion applications. The European Union (E.U.) has developed and tested alloys MANET-1 and MANET-2, which are similar to the Fe-12Cr-1MoVW commercial alloy HT-9. Currently they are working on lower-activation higher-performance versions of these alloys. Researchers in Japan have developed reduced activation ferritic steels designated as F82H, JFL-1, JFL-2 and JFL-3. These steels contain 7–9 wt.% Cr, about 2 wt.% W and small amounts of V and Ta. In a collaborative research effort among the three parties (U.S., E.U., and Japan), the International Energy Agency (IEA)-sponsored Ferritic/Martensitic Steels Working Group has selected the modified F82H steel for large-scale production and testing [4]. The Russian Federation (RF) also will participate in future IEA-sponsored developmental efforts involving ferritic steels.

Proposed solid-breeder designs have involved a variety of shapes and geometries for the ferritic steel structural material. For example, a leading BCSS design calls for the solid breeder to be encased in ferritic steel plates with He cooling on the outside of the plates [1]. European concepts have been proposed for both the breeder-in-tube (BIT) and breeder-outside-tube (BOT) design concepts [5]. In addition to the solid-breeder concepts, the E.U. has proposed both a self-cooled lead-lithium design within a He-cooled, box-like, ferritic steel structure and a water-cooled design (with lead-lithium breeder) with the coolant flowing through ferritic steel tubes within the rectangular channels of the box-like structure [6]. For the helium-cooled designs, the maximum allowable structure temperature is set at 550 °C. For ferritic steel in contact with liquid lead-lithium, the maximum allowable interface temperature is about 450 °C. No serious design has been developed for ferritic steel and self-cooled Li. Within the E.U. and Japan, there is a concern about the safety implications of using lithium coolant, regardless of the structural material. Within the U.S., vanadium alloys are considered to be far superior to ferritic steel as a structural material for use with liquid lithium coolant.

6.2.3. Material Properties

Traditional ferritic steels considered for use as structural materials in a fusion reactor first-wall, blanket and divertor fall into two composition categories: Fe-(10–12)Cr-1Mo and Fe-(7–9)Cr-1Mo, where the numbers are in wt.%. Unlike austenitic stainless steels, they contain a higher amount of carbon (0.08–0.2 wt.%). The excess of carbon induces a martensitic phase transformation during cooling which, analogous to cold-working, results in a high strength, low-ductility material. The material is then heat treated at 650-760 °C for 0.5–2.5 hours to achieve an optimum combination of strength and ductility. The resulting structure is referred to as martensitic/ferritic and is distinguished from the γ-Fe microstructures of austenitic steels.

The higher chrome alloys have been modified to include additions of V and W (*e.g.,* the commercial HT-9 is a Fe-12Cr-1MoVW higher strength alloy). The lower chrome alloys have been modified by additions of V and Nb (*e.g.,* Fe-9Cr-1MoVNb) to increase the strength of these alloys. Because of the concerns regarding radioactivity of the alloying elements Mo, Nb and Ni, reduced-activation versions of the traditional and modified ferritic steels have been developed for fusion applications. In particular, W, V, and Ta are substituted for the Mo and the Nb, while Mn is substituted for most of the Ni. As a class of materials, these will be referred to as Fe-9Cr-2WVTa, where the 9Cr is a generic representation of alloys with 7–9 wt.% Cr and 2WVTa refers to 2 wt.% W with small amounts of V and Ta.

Several aspects of the basic material behavior of these alloys are summarized below. The temperature range of operation is very important in determining the thermal and mechanical performance of in-vessel components. Ferritic steel is limited in both the upper and lower allowable temperatures, as described in Sec. 6.2.3.1. Neutron irradiation affects the basic material properties, thus restricting the service life of in-vessel components. The existing database relating to irradiation effects is summarized in Sec. 6.2.3.2. Sec. 6.2.3.3 describes some of the advantages of the use of steel due to well-developed industrial capabilities, and Sec. 6.2.3.4 reviews some of its attractive nuclear characteristics.

Based on the performance of these materials, design temperature windows of 250–550 °C for use with a He coolant and 285–450 °C (interface) for use with Pb-Li coolant have been recommended. The lower temperature limit is based on a ductile-to-brittle transition temperature (DBTT) for irradiated ferritic steel of 250 °C (except with PbLi, where the melting point must be respected).

6.2.3.1. Temperature limits

The temperature window for ferritic steels is limited on both the upper and lower ends. Based on the data available to date for Fe-12Cr-1MoVW and Fe-9Cr-1MoVNb alloys, the lower temperature limit would have to be set at about 250 °C for ferritic steels. This assumes that the design allowable stresses account for the reduced ductility in this regime and that there is an adequate design margin for stresses induced during shut-down and during off-normal events (*e.g.,* seismic) while the reactor is at temperatures below 250 °C.

However, there still would be concern about the behavior of the embrittled material during shut-down events. The embrittlement can be partially reversed by periodic annealing of the structural components at 400–500 °C during shut-down. This may or may not be a practical solution. It is hoped that continued development and testing of the reduced-activation Fe-9Cr-2WVTa steels will result in a decrease in the minimum allowable operation temperature. This remains to be demonstrated for fusion-relevant neutron damage and He levels.

If the reduced-activation ferritic steels [Fe-(7–9)Cr-2WVTa] are demonstrated to have performance superior to the above alloys up to 100 dpa with 100–1000 appm He and down to temperatures lower than the current data base for these steels (365 °C), then the minimum operating temperature can be lowered. Also, in future work, the minimum operating temperature should be based on fracture toughness data (which is not available) rather than DBTT and on the more sophisticated ASME rules. While Charpy DBTT data are adequate for screening purposes, they are not adequate for design analyses.

The upper temperature limit of 550 °C commonly used in E.U. and Japanese design studies with He coolant is well-established, based on the decreasing tensile and creep strength of ferritic steels with increasing temperature. Fig. 6.2-1 shows the ultimate tensile strength, along with the allowable design stress, for Fe-12Cr-1MoVW and Fe-9Cr-1MoVNb, as compared to values for the E.U. 316L(N) steel. Irradiation produces a hardening or increase in this allowable stress for temperatures below 450 °C, but a softening above about 550 °C (see Fig. 6.2-2). It is unlikely that advances made in optimizing the chemistry and heat-treatment of the reduced-activation alloys will result in a substantial improvement in this upper temperature limit. However, the upper temperature limit is design-dependent. Designs with lower operational stresses can tolerate higher temperatures.

In the case of liquid metal coolants and/or breeders, compatibility concerns would limit the maximum interface temperature to below 550 °C. Values near 450 °C are com-

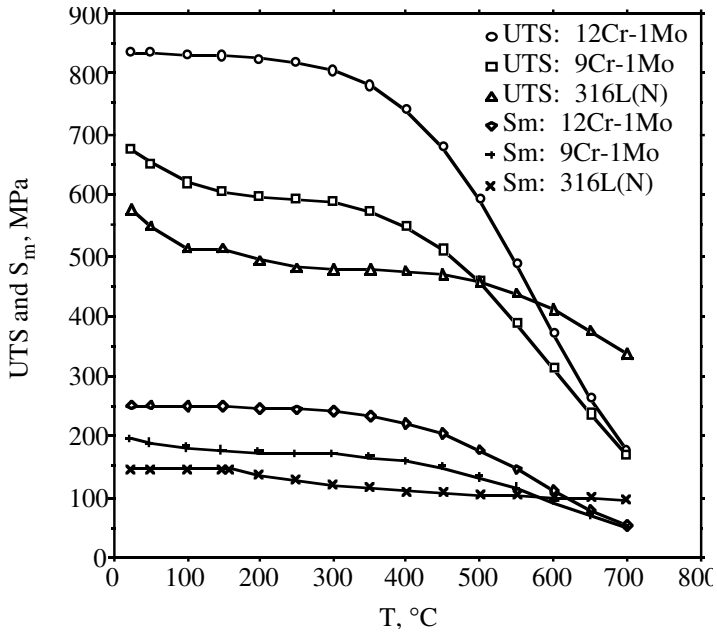

Figure 6.2-1. Ultimate tensile strength (UTS) and maximum allowable primary stress (S_m) for unirradiated steels: Fe-12Cr-1MoVW (*e.g.,* HT-9), Fe-9Cr-1MoVNb, and annealed 316L(N).

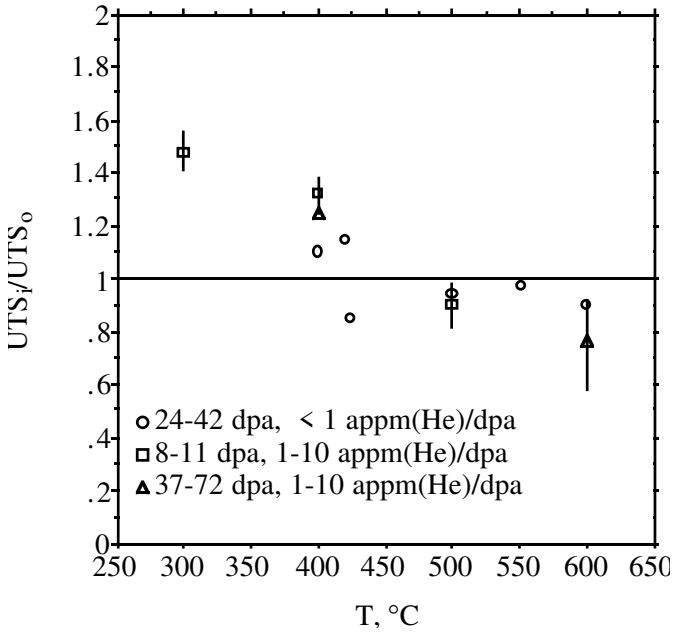

Figure 6.2-2. The change in the ultimate tensile strength (UTSi) of irradiated Fe-12Cr-1MoVW and Fe-9Cr-1MoVNb ferritic steels relative to the unirradiated ultimate tensile strength (UTSo).

monly used for ferritic steel in contact with liquid Pb-Li. Higher temperatures would be allowed for a ferritic-steel/Li interface, but no designs for this combination of materials have been developed. However, as with vanadium alloys, ferritic steels would need an insulating coating to minimize the MHD pressure drop. If such a coating were to be developed for ferritic steels, then the compatibility of the ferritic-steel/coating/liquid-metal system would determine if there would be a limit on the interface temperature.

The 550 °C upper temperature limit results in gross thermal efficiencies for the blanket region of about 37% for a direct He Brayton cycle and about 45% for a supercritical Rankine steam cycle. It is unlikely that improvements in the reduced-activation alloys would change the upper temperature limit significantly. Also, given the anticipated divertor surface heat loads, ferritic steels would not be practical for the structural material in this component. This represents about 20% of the thermal power of the reactor. Either an acceptable higher-performance material must be found, or the overall plant efficiency would be limited to less than 80% of the blanket efficiency.

6.2.3.2. Irradiation database and R&D needs

Problems associated with the traditional and modified stainless steels are being addressed within the IEA-sponsored Working Group on Ferritic/Martensitic Steels, as well as within the three participating parties. The problems being addressed are: activation associated with Mo, Nb, and Ni; low tensile and impact ductility for irradiation below about 400 °C; and, to a lesser extent, loss of tensile and creep strength, particularly at temperatures above 550 °C. Optimization of the chemical composition and the thermomechanical heat treatment of this class of alloys is being performed in an attempt to develop better ferritic steels for fusion applications. The focus of the IEA effort is the modified F82H steel (Fe-8Cr-2WVTa), which has lower activation as compared to other alloys within this class which contain Mo and Nb.

An extensive study of the irradiation effects on Fe-12Cr-1MoVW and Fe-9Cr-MoVNb was conducted under the fission reactor programs. The performance of these alloys is quite good in the fast-fission-reactor temperature range of 400–600 °C, particularly when tested in a fast-fission neutron environment. For example, the increase in ductile-to-brittle-transition temperature (DBTT) tends to saturate at about 10 dpa to maximum values of 50–150 °C when irradiated at 390 °C, with the Fe-9Cr-1MoVNb showing the lower increases. However, when these same alloys are irradiated in mixed-spectrum reactors, with and without extra Ni added to simulate fusion-relevant He/dpa ratios, at temperatures in the range of 300–400 °C, increases in DBTT as high as 270 °C have

been observed. It is still debated within the materials community whether the ductility loss in the thermal- and mixed-spectrum reactor radiations is due to helium embrittlement, helium-assisted precipitation-induced embrittlement, and/or defect and precipitation hardening [7]. While the consequences for fusion applications greatly depend on the hardening mechanisms (first-wall ferritic-steels will experience helium generation on the order of 10 appm/dpa) it is not clear how to resolve this issue without a fusion neutron source.

Preliminary results on a reduced-activation Fe-9Cr-2WVTa alloy indicate DBTT values well below room temperature up to 30 dpa when irradiated in a fast-fission reactor at T $\geq$ 365 °C [8]. It remains to be demonstrated that the DBTT remains sufficiently low up to higher fluences (*e.g.,* 100 dpa), with up to 10 appm/dpa He generation, in the temperature range of 250–400 °C. In the near-term, this may require testing of the new reduced-activation alloys in thermal- and mixed-spectrum reactors such as HFR and HFIR, concurrent with development of techniques to determine more directly the causes of the embrittlement previously observed after irradiation in these reactors.

While some ferritic steels (*e.g.,* Fe-9Cr-1MoVNb and Fe-12Cr-1MoVW) are code-qualified, the new steels being developed may need to be further characterized to achieve the same status. Once an alloy has been identified as promising from a performance perspective, it is necessary to generate a data base for use in determining design and allowable stresses. At a very minimum, the following data are needed:

1. A large number of data points for yield strength, ultimate tensile strength and ductility of the unirradiated material at room temperature for different grades, lots and heats of this material;

2. Enough data points at higher temperatures to establish a temperature trend curve; and

3. Enough data points for irradiated material at these same temperatures to establish a hardening and softening trend curve.

These data would be sufficient to establish limits on primary membrane stresses, primary bending stresses and secondary thermal stresses during short-time steady-state (*i.e.*, non-cyclic) operation. Fracture toughness data would be needed to establish limits on peak stresses at geometric discontinuities and cracks. Cyclic operation and/or high temperature operation would require additional data on creep strength, fatigue strength and creep-fatigue interaction. If, as expected, the mechanical properties of the new ferritic

steels fall within the scatter bands of the data for the code-qualified ferritic steels, then no additional effort is needed in this area.

6.2.3.3. Manufacturing capabilities

Ferritic steel has advantages over advanced structural materials (*e.g.,* vanadium alloys) due to its large installed industrial manufacturing and fabrication capability both in the United States and abroad. Large nuclear grade components are currently being manufactured with ferritic steel. There is capability to manufacture all types of commonly fabricated shapes including plates, sheets, wire, and forgings. All the standard fabrication processes are well documented, including cutting, forming, welding, forging, and heat treating. The unirradiated physical properties are well known and suitably documented.

Even if the blanket and the plasma-facing components are to be made from alternative structural materials, parts of the shielding and ex-reactor components are likely to be constructed of ferritic steel in order to save on the cost. In this case, additional problems may arise due to the transition between different material systems, involving changes in mechanical properties and corrosion of dissimilar materials. These problems would be eliminated in a system using a single material.

Ferritic steels are more difficult to weld than austenitic stainless steels because of the care needed before and after welding. Typically, a pre-weld treatment is needed to increase toughness by heating to $\lesssim 400\,^{\circ}\mathrm{C}$ for a sufficient time. A post-weld heat treatment is needed to temper the welded joint by heating to $760\,^{\circ}\mathrm{C}$ for 2.5 hours and then cooling at a controlled rate. While all forms of welding can be used with ferritic steels, ion-beam and laser-beam welding in an inert atmosphere are preferred because they limit the heat-affected zone and the degree of chemical interaction.

The reduced-activation modifications to ferritic steels for fusion application are anticipated to have minimal effect on manufacturing capabilities or processes. Thermophysical properties are not expected to change in any significant way. The mechanical properties may be affected to some degree, but not necessarily in a detrimental way. However, once a developmental alloy has been selected, it is important to demonstrate the fabricability and weldability of such an alloy.

6.2.3.4. Nuclear characteristics

Steels in general possess attractive nuclear characteristics compared to other candidate structural materials. For instance, steel has the best shielding capability after tungsten, and is superior to V and SiC in attenuating radiation. This property is important for the economics of fusion power plants as it helps reduce the overall size and cost of the machine. A savings of 10–20 cm in the shield is achievable by employing steel instead of V or SiC as the shielding material (Sec. 6.2.3.4). Another attractive feature of steel is the ability to multiply the neutron energy. The energy multiplication of steel is significantly larger than that of SiC and comparable to that of V. This feature should enhance the power balance and, when combined with the superior shielding properties of the steel, will improve the economics of the fusion power plant.

The structural materials used in the first wall and blanket of fusion power plants will require frequent replacement due to radiation damage considerations. The cumulative damage levels in the structure at the projected first wall and blanket end-of-life are compared for ferritic steel, V, and SiC in Table 6.2-I for a typical 5 MW/m^2 neutron wall loading. It is assumed that the first wall and blanket will be replaced upon reaching 150 dpa (displacements per atom) in both ferritic steel and V, and 3% burn-up in SiC. The dpa limits for ferritic steel and V are based primarily on extrapolations of swelling and irradiation creep data. It remains to be demonstrated that the mechanical properties are adequate up to such high exposure levels. Based on the assumptions in Table 6.2-I, the ferritic steel, V, and SiC structures of the first wall and blanket should be replaced after 2.4, 2.4, and 2.6 full power years of operation, respectively. As indicated, V generates

Table 6.2-I.
Cumulative Damage Level for the First Wall
at the End-of-Life of the First Wall and Blanket

	ferritic steel	V	SiC
Damage rate (dpa)	150	150	160
He Production (appm)	1,980	980	43,030
H Production (appm)	6,640	4,670	16,090

the lowest amount of He and H gases while SiC has a relatively high gas production level which could deteriorate the thermo-mechanical properties of the composites. Note that the He/dpa ratios in the first wall structures of fusion power plants are 13, 7, and 270 for ferritic steel, V, and SiC, respectively.

6.2.4. Ability to Meet Requirements

The choice of primary in-vessel structural material impacts the ability of the device to meet most, if not all, of the top-level requirements. These include safety, environmental and economic attributes. Our examination focused on a limited set of these, with particular attention to those which may serve to discriminate between different material choices. We concentrated on (1) attributes which impact the ability of the plant to meet economic goals, including maintainability, thermal conversion efficiency and economic tradeoffs between improved performance and the cost of fabricated structures, and (2) activation attributes which impact the ability of the device to meet the waste-disposal and no-evacuation requirements.

6.2.4.1. Maintainability

Maintenance of the ferritic steel structures requires special procedures, particularly if rewelding of components is required. The irradiated ferritic structural material will have both radiation damage and transmuted helium within the base material. Upon rewelding, these helium atoms migrate to the grain boundaries and cause problems of poor reweld performance. Special processes must be developed to reliably weld irradiated materials. Post-weld heat treatment will be required for re-welded ferritic steels. (The same may also prove true for vanadium alloys, but the data base is too limited to allow a conclusion at this time.) If the ductile-to-brittle transition temperature is too high, the component to be maintained may be in a brittle condition or the handling temperature must be raised. If hydrogen from the plasma has permeated the material, hydrogen embrittlement may cause handling or life-limiting problems. Annealing may solve or minimize some of the above problems, but this imposes another step in the maintenance process.

The activation level of the structural materials within the plasma chamber also influences the design and lifetime of the chamber and hot cell maintenance equipment. They have to be designed to handle the background radiation levels inside the chamber and

the hot cell. A ferritic steel which has been optimized for low-activation and a low DBTT can probably be acceptably maintained.

6.2.4.2. Thermal conversion efficiency

Because of large capital cost, it is essential for fusion plants to operate with relatively higher thermal efficiency in order to achieve a competitive cost of electricity. Ferritic steel has been examined with respect to its effectiveness as a structural material for power conversion systems and the heat transport systems that form an integral part of the power conversion process. The heat transport systems include the first wall and blanket, which transport roughly 80% of released fusion energy as heat, and the divertor, which transports most of the remaining energy.

Ferritic steels are compatible with helium coolant in all respects. There is no corrosion concern nor is there a concern with helium ingress causing embrittlement. Likewise, ferritic steels are compatible with water/steam, provided water chemistry is controlled in a manner typical for steam power plants. There is a small concern over the compatibility of ferritic steel with lithium at higher temperatures. Ref. [1] suggests a maximum interface temperature between 535 and 550 °C for lithium velocities between 1.5 and 0.5 m/s in a ferritic steel circuit.

The temperature limit (550 °C for use with a plasma facing component) presents a significant concern with respect to heat transfer, especially for very high heat flux conditions, as is the case for the divertor. For both the first wall and the divertor, the coolant must be cold enough to provide a sufficient temperature difference (ΔT) to enable the heat flux to be transferred to the coolant without exceeding the ferritic steel temperature limit on the plasma facing surface. The ΔT is composed of two parts, the ΔT through the ferritic steel wall (assumed to be 2 mm thick) and the film ΔT. Table 6.2-II summarizes ΔT values for plasma-facing components made of ferritic steels and various coolants. Table 6.2-II shows that the total δT's are so large for the peak heat flux condition on the divertor that the heat transfer is either not physically possible or practical for any of the heat transport fluids. Therefore, ferritic steel is not suitable as a candidate material for the divertor, unless the peak heat flux is significantly reduced.

Considering maximum structure and interface temperatures, ferritic steel can be used for the first wall with practical values of bulk coolant outlet temperature limited to 490–500 °C. At this temperature a direct helium Brayton cycle would have a maximum gross efficiency of 37%–38%. A direct supercritical-steam Rankine cycle could achieve a gross

efficiency of nearly 45% and a lithium cooled first wall with an intermediate loop and a supercritical Rankine cycle could achieve a maximum gross efficiency of 42%–43%. In the latter case, an intermediate loop is required because of tritium generation in the first wall lithium heat transport circuit and compatibility concerns between lithium and water.

Although the efficiencies are respectable for first-wall heat-to-power conversion, this represents only 80% of the total fusion power. Another material (*e.g.,* vanadium) would have to be used for divertor heat-to-power conversion in order to convert the divertor

Table 6.2-II.
Temperature Drop across In-Vessel Components
(Ferritic Steel Structure[(a)] and Various Coolants)

	Helium		Water		Lithium	
	Peak	Avg.	Peak	Avg.	Peak	Avg.
Divertor:[(b)]						
Wall ΔT (°C)	391	79	391	79	(*c*)	79
Film ΔT (°C)	160	59	(*c*)	76	190	34
Total ΔT (°C)	551	138	(*c*)	155	(*c*)	113
First Wall:[(d)]						
Wall ΔT (°C)	39	28	39	28	39	28
Film ΔT (°C)	32	23	38	31	17	12
Total ΔT (°C)	71	51	77	59	56	40

(*a*) For a 2-mm thick structure.

(*b*) For a peak and average heat flux of 5.0 and 1.0 MW/m^2, respectively.

(*c*) Not physically possible because ΔT is so large as to require the coolant to be in solid phase.

(*d*) For a peak and average heat flux of 0.5 and 0.3 MW/m^2, respectively.

heat loads efficiently. The impact of the thermal conversion efficiency on the cost of electricity is explored in the next section.

6.2.4.3. Cost assessment

In-vessel components constitute a significant fraction of the total cost of a magnetic fusion power plant (∼10%). Therefore, it is desirable to employ inexpensive structural materials. The achievable cost of fabricated structures is still a subject of debate. The complexity of the structures, impurity levels, tolerances and inspection quality can have a large impact. In this section, the trade-offs between ferritic steel and vanadium-based power plants are examined to help understand under which conditions advanced materials offer significant improvements to the cost of electricity.

Vanadium alloys are relatively new structural alloys. To date, there have not been major industrial applications to support their development. The three basic costing elements for a fusion structural material (production cost of different product forms, fabrication cost, and installation) are still to be developed for V-alloy. Therefore, there is no statistical information available to project a reliable unit cost. Only a rough estimate on the lower and upper bounds of the unit cost can be made. Based on the application of advanced structural materials for fusion devices, the product form cost will amount to about 30% of the unit cost of the final component, including labor. Taking the 1995 cost of advanced Ni-based structural materials as a starting point, the product form cost is about $100/kg. If this is assumed to be the same for V-alloy, then the lower bound unit cost can be assumed to be about $300/kg. A recently placed DIII-D contract for the V-4Cr-4Ti alloy material necessary for the upper divertor in the Radiative Divertor Program (RDP) shows a finished V-alloy component cost of about $600/kg. For a power plant, this unit cost is expected to be lower due to increased experience far into the future.

Our analysis is based on the unit cost of the V-alloy structure at $300/kg, ferritic steel structure (MHT-9) at $68/kg, and Tenelon filler at $25/kg in constant 1992 dollars. It should be noted that the cost of ferritic steel structures is also uncertain as large-scale industrial infrastructure for these material does not exist.

The assessment was performed on a "systems level" using the ARIES System Code (ASC). To provide a common basis for comparison, the ARIES-II design concept was adopted. ARIES-II is a second-stability tokamak with a radiative divertor and "close-in" cryostat (wrapping around the outboard TF coil legs). All design variants are required

to provide a net electric output of 1000 MWe. The effect of reduced efficiency is to increase the size of both in-vessel and ancillary systems in order to produce the additional thermal power to reach 1000 MWe. Reduced power density mainly affects the size of the in-vessel components and coils. The system optimization also maintained a fixed aspect ratio $A = 4$, plasma $\beta = 3.4\%$ and peak allowable field at the TF coil of 16 T. Taking advantage of the low neutron flux in the shield, the original ARIES-II design was adjusted by replacing the 15% V structure in the outer layers of the shield by steel. A 5% V coolant cladding is kept for coolant compatibility. By making this change, the cost of the vanadium in the shield (which represents a major cost item) has been reduced substantially as compared with earlier designs. The structures in the first wall, blanket, and reflector are still made entirely of vanadium. The presence of steel in the shield is not expected to prevent the plant from meeting the Class-C waste disposal or safety requirements.

To simulate a steel design in the ASC, the V structure simply was replaced with ferritic steel. The U.S. has not developed a serious power plant design using ferritic steel in many years (since STARFIRE [10]). Recent work in Europe [5, 6] was used to determine the appropriate range of thermal conversion efficiencies to use. It is true that there will be many differences between the ferritic-steel and V designs in terms of radial dimensions, energy multiplication, pumping power, power conversion system, level of safety assurance (LSA) rating, *etc.*, but these differences (which include both positive and negative effects) were not factored into this analysis.

Different options for steel power plants were assessed with simple economic models that have net thermal efficiencies of 30% and 35%. A 35% thermal efficiency might be expected with a helium-cooled system, whereas a lower efficiency of 30% corresponds more closely to a water cooled (with Li_2O breeder) system [5, 6]. Higher efficiencies may be possible with advanced designs, but the analysis here is based on existing European Demo blanket designs.

The lower power density of steel has been enforced by limiting the peak neutron wall loading to ≤ 4 MW/m^2. This limitation is design-dependent, and is based on engineering judgment. Perhaps more importantly, first-wall surface heat flux is constrained to $\leq$ 0.5 MW/m^2 (Table 6.2-II). Based on the ARIES-II reference design, peaking factors on the wall loading and surface heat flux of 1.75 and 1.2 were used, respectively. The surface heat flux peaking factor assumes peaking of only the bremsstrahlung heat flux (edge plasma heat loads on the first wall and divertor are still highly uncertain). For vanadium, engineering limits on power density are not reached in the reference design.

The end-of-life first-wall fluence used for the comparison is 15 MW-y/m^2 for both ferritic steels and V. This is based on a 200 dpa limit. These values are highly uncertain, given the absence of high-fluence data. In addition, they are likely to be dependent on the operating conditions, such as stress levels. Given a fixed fluence lifetime, the component operating life depends only on the wall loading. Operating lifetime affects the replacement cost and also the availability (less frequent replacement lowers the annual replacement cost and increases the expected availability). Operation at lower power density results in slower neutron damage accumulation, thus extending the operating life of components. Assuming the time to repair and replace components is not changed, this leads to higher availability. The cost of electricity (COE) is inversely proportional to the plant availability factor, which is expected to be dominated by the planned outages for regular in-vessel component replacement. Therefore, one expects a lower power density system to benefit from this effect with a reduced COE. A second, but more subtle effect on availability results from the fact that systems pushed to higher power density are likely to suffer from higher failure rates. This effect has been ignored in this analysis, as it is difficult at this time to quantify such an effect.

The gross thermal conversion efficiency used here is the ratio of the gross electric power divided by the total useful thermal power generated in the fusion power core. It does not include plant recirculating power factors. The key operating parameters which determine the maximum achievable gross efficiency are the maximum allowed material design temperatures and stresses. Lower efficiencies for ferritic steels result from both lower temperature limits and lower thermal stress factors.

For the coolant options under consideration, the V/Li self-cooled design utilizes an intermediate heat exchanger for the control of tritium leakage, and is coupled to a Rankine cycle. Efficiencies as high as 49% have been predicted, but a more conservative value of 46% is adopted here assuming a lithium coolant outlet temperature of 610 °C. For the helium-cooled option, a similar gross thermal efficiency can be reached with the Rankine cycle. Even though a secondary loop is not required, the maximum Rankine cycle efficiency is controlled by the thermodynamic properties of the steam side.

For the ferritic steel designs, the thermal conversion efficiency was varied parametrically to determine the minimum goals for COE to be comparable with V systems. It is very important to consider the loss of useful thermal power in a ferritic steel divertor. The divertor power accounts for up to 25% of the heat removed from the power core, including neutron, thermal radiation, and transport power. High-heat-flux components using steel are likely to be constrained to operate with low coolant temperature, thus reducing the gross thermal efficiency of the plant substantially.

Table 6.2-III lists the major device parameters adopted from ARIES-II. The COE for the modified V system (with steel used in the shield) is 3 mill/kWh less than the previous reference case (with vanadium structure throughout). Table 6.2-IV summarizes the economic results for the ferritic steel cases. In the case with unconstrained wall loading, the COE is competitive with the V plant at a reasonable efficiency of 35%. However, in order to account for the lower conversion efficiency, the code has optimized by increasing the peak power density to over 5 MW/m^2 (and peak surface heating to nearly 0.5 MW/m^2).

Table 6.2-III.
Major Parameters of Modified ARIES-II Design

Net electric power (MW)	1,000
Useful thermal power (MW)	2,570
Gross thermal efficiency	46%
Major radius (m)	5.60
Peak/average wall load (MW/m^2)	5.1/2.9
Peak/Average first-wall heat flux (MW/m^2)	0.37/0.31
On-axis toroidal field (T)	8.0
Maximum field at the coil (T)	15.9
Fusion power density (MW/m^3)	4.8
First wall and blanket cost (M$)	54
Vacuum vessel cost (M$)	51
Shield cost (M$)	256
Total direct capital cost (M$)	2,048
First wall and blanket replacement cost (mill/kWh)	4.0
Cost of electricity (mill/kWh)	71

Table 6.2-IV.
Impact of Gross Thermal Efficiency on the Performance of the Ferritic Steel Designs

	Unconstrained neutron wall loading				Constrained neutron wall loading			
Gross thermal efficiency [(b)]	0.25	0.30	0.35	0.40	0.25	0.30	0.35	0.40
Net electric power (MW)	1,000	1,000	1,000	1,000	1,000	1,000	1,000	1,000
Major radius (m)	6.52	6.24	6.00	5.80	9.08	8.16	7.48	6.96
Peak wall load (MW/m^2)	7.7	6.9	6.2	5.7	4.0	4.0	4.0	4.0
Peak first-wall heat flux (MW/m^2)	0.57	0.50	0.46	0.42	0.29	0.30	0.30	0.30
On-axis toroidal field (T)	8.5	8.4	8.2	8.1	6.6	6.8	7.0	7.1
Maximum field at the coil (T)	15.9	15.9	15.9	16.0	11.2	11.9	12.5	13.0
Fusion power density (MW/m^3)	6.2	5.8	5.4	5.2	2.3	2.6	2.8	3.0
First wall and blanket cost (M$)	26	24	22	21	43	37	32	28
Vacuum vessel cost (M$)	69	64	59	55	132	107	90	78
Shield cost (M$)	261	242	226	214	443	377	326	289
Total direct capital cost (M$)	2,398	2,206	2,067	1,975	2,718	2,431	2,235	2,098
Replacement cost[(b)] (mill/kWh)	3.8	3.0	2.5	2.1	2.9	2.4	2.1	1.9
Cost of electricity (mill/kWh)	81	74	70	67	89	80	74	70

(*a*) Including the pumping power.

(*b*) For first wall, blanket, and reflector.

The effect of imposing a wall-loading constraint on the ferritic-steel designs is to increase the size by 25%–30% and the COE by 6.2%–7.7%, as shown in Table 6.2-IV. Comparing all designs at a common LSA = 2 rating, a wall-loading constrained steel design must attain a 39% thermal conversion efficiency to have a COE comparable to that for the modified V design. A 34% gross thermal efficiency (ratio of gross electric to total thermal power) is required for the unconstrained wall-loading steel design to be comparable in cost to the improved V design. If the ferritic steel system is unable to meet the LSA = 2 rating, the difference between the COE of the FS and V systems will become larger. The full range of cases examined here have a net COE between 70–80 mill/kWh. This is a significant, but not definitive difference. In the modified ARIES-II design, the fusion power core cost does not dominate the COE; therefore savings obtained by further minor adjustments are not expected to save more than a few mill/kWh.

6.2.4.4. Activation of ferritic steels

The safety characteristics of fusion power plants are directly related to the choice of structural materials. Low activation ferritic/martensitic steels are the most attractive alloys because they produce only low-level waste (Class C) at the end of the life. Detailed activation analyses were performed to identify the safety, environmental and rad-waste characteristics of five different ferritic steel alloys: HT-9, low activation (modified) HT-9, the IEA modified F82H steel (9Cr-2WVTa), and the leading European Community candidates, MANET-2, and LA12TaLC alloys. Several activation-related issues were investigated for each of the steel alloys: activity, decay heat, and biological hazard potential (BHP). The waste disposal ratings (WDR) of each of the alloys at the end of its lifetime were also evaluated.

Structure Activity, Decay Heat, and Biological Hazard Potential. The neutron flux used for the activation calculation was generated by the one-dimensional discrete ordinates neutron transport code ONEDANT [11]. A 46-group neutron and 21-group gamma coupled cross-section library containing P_3 Legendre expansions of the scattering cross sections based on the ENDF/B-V basic data files was used in the transport calculations. The activation calculations were conducted using the DKR-ICF computer code [12] with activation cross sections taken from the new USACT93 [13]. The USACT93 library is based on neutron transmutation cross section and isotopic radioactive decay data from the ENDF/B-VI and EAF3 files. The neutron transmutation data is in a 46-group structure format. All materials were assumed to stay in the reactor for 3

full power years (FPY). The biological hazard potentials were calculated using the maximum permissible concentration limits in air for the different isotopes according to the NRC regulations specified in 10CFR20 [14]. A scalable average neutron wall loading of 1 MW/m^2 was used in the analysis.

Figures 6.2-3 to 6.2-8 shows that all of the ferritic and martensitic steel alloys produce identical amount of radioactivity during the first 10 years following shutdown. The short-term radioactivity induced in steel is generally dominated by ^{56}Mn ($T_{1/2} = 2.6$ h), ^{54}Mn ($T_{1/2} = 312$ d), ^{51}Cr ($T_{1/2} = 27.7$ d), and ^{55}Fe ($T_{1/2} = 2.73$ y). The intermediate-term radioactivity is dominated by ^{55}Fe, ^{54}Mn, ^{60}Co ($T_{1/2} = 5.27$ y), and ^{3}H ($T_{1/2} = 12.7$ y). The ^{55}Fe and ^{54}Mn isotopes, which are produced by the transmutation of iron, dominate the radioactivity during the first few years following shutdown. The long-term radioactivity is dominated by ^{53}Mn ($T_{1/2} = 3.7 \times 10^6$ y), ^{14}C ($T_{1/2} = 5,730$ y), ^{93}Nb ($T_{1/2} = 16.1$ y), and ^{94}Nb ($T_{1/2} = 2 \times 10^4$ y). The two ferritic alloys, IEA modified F82H and modified HT-9, as well as the low activation martensitic alloy, LA12TaLC, result in lower levels of long-term radioactivity due to their low niobium impurity content.

Rad-waste Classification. The structure activation results were utilized in the rad-waste classification performed using the WDR computer code [15]. The rad-waste of all alloys was evaluated according to both the NRC 10CFR61 [16] and Fetter [17] waste disposal concentration limits.

There are three different classes of rad-waste under U.S. regulations. The most stringent requirements are for Class A, segregated waste. The major hazard of this class of waste is to the individuals responsible for handling it. However, such waste is not considered to be hazardous following the loss of institutional control over the disposal site. The 10CFR61 regulations assume that the waste-disposal site will remain under administrative control for 100 years and that the dose at the site due to an inadvertent intruder at the end of the 100 year period is less than 500 mrem/y.

Class C intruder waste allows for higher concentrations of rad-waste. Class C waste must be packaged and buried such that it will not pose a hazard to an inadvertent intruder after the 100 year institutional period is over. Class C waste is assumed to be stable for 500 years.

The waste-disposal rating (WDR) is defined as the sum of the ratio of the concentration of a particular isotope to the maximum allowed concentration of that isotope taken over all isotopes and for the particular class. If the calculated WDR ≤ 1 when Class A limits are used, the rad-waste should qualify for Class A. If the WDR is > 1 when Class A

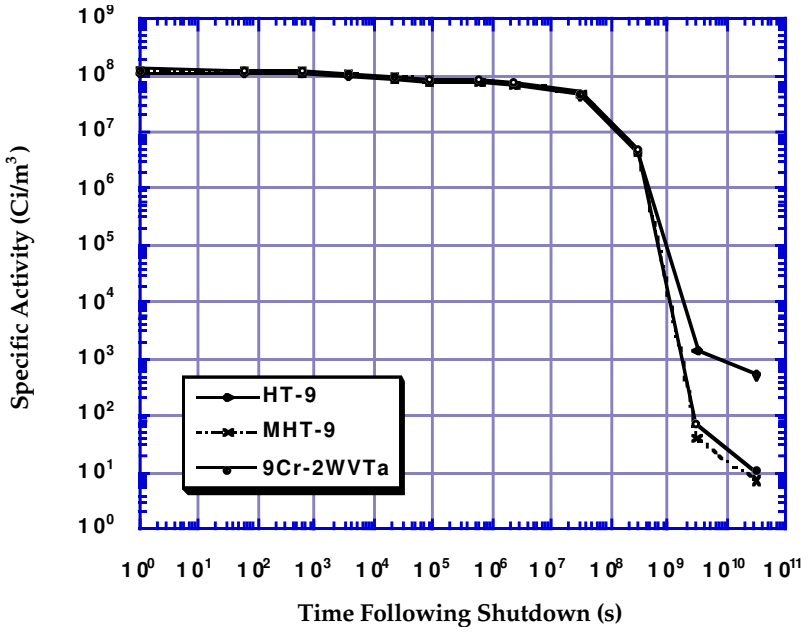

Figure 6.2-3. Activities induced in different ferritic steel candidates.

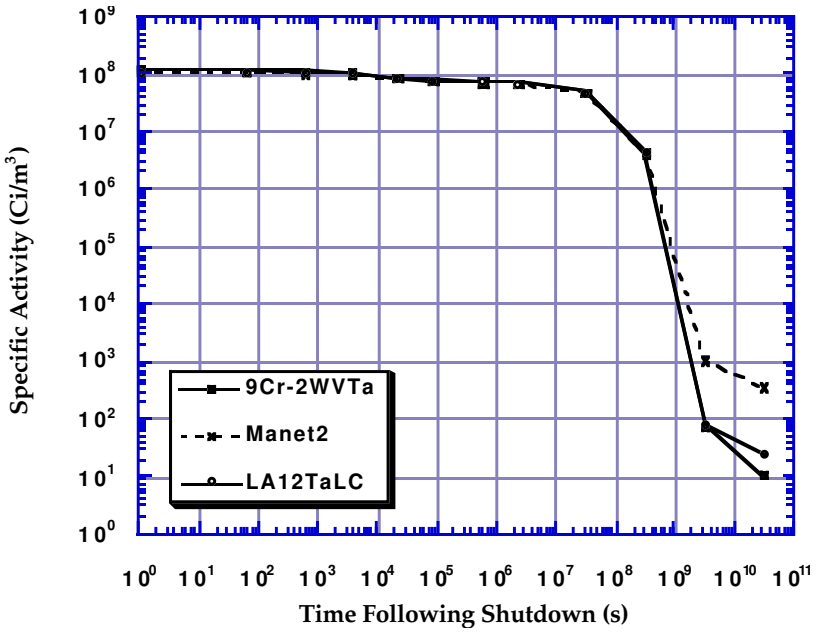

Figure 6.2-4. Activities induced in the F82H alloy and the leading martensitic steel candidates.

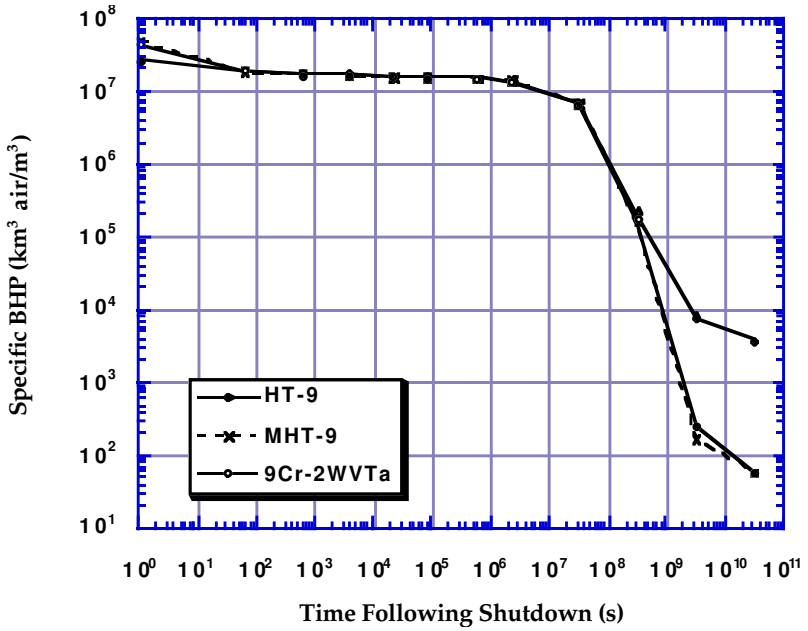

Figure 6.2-5. BHP induced in different ferritic steel candidates.

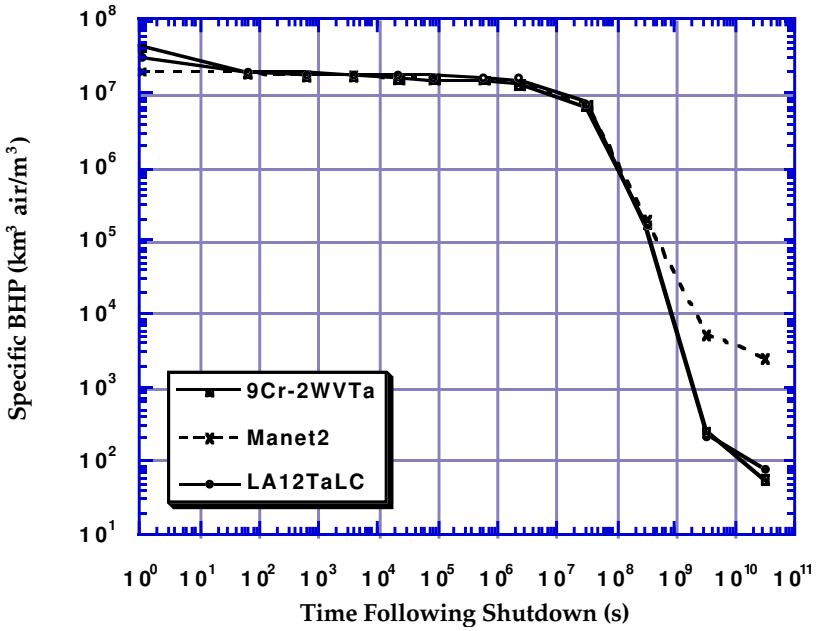

Figure 6.2-6. BHP induced in the F82H alloy and the leading martensitic steel candidates.

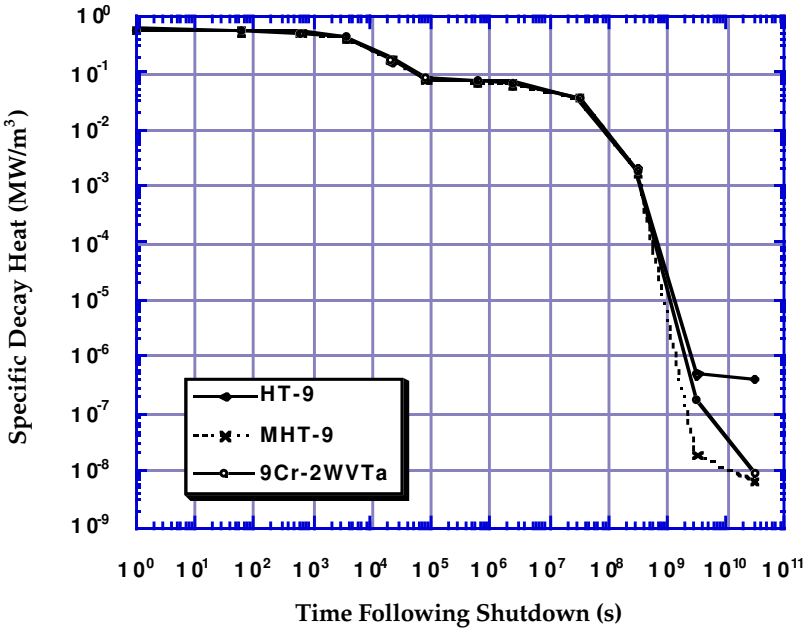

Figure 6.2-7. Decay heat induced in different ferritic steel candidates.

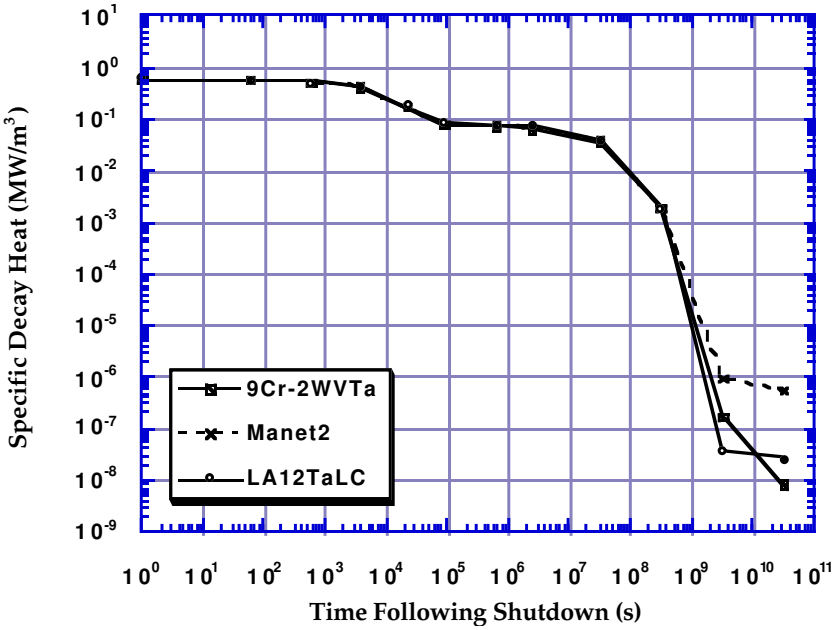

Figure 6.2-8. Decay heat induced in the F82H alloy and the leading martensitic steel candidates.

limits are used but ≤ 1 when Class C limits are used, then the waste is termed Class C . If WDR > 1 when Class-C limits are used, it implies that the rad-waste does not qualify for shallow land burial.

Fetter developed a modified version of the NRC intruder model to calculate waste disposal limits for a wider range of long-lived radionuclides that are of interest for fusion researchers than the few that currently exist in the current 10CFR61 regulations. Fetter's model included more recent transfer coefficients and dose conversion factors. However, while the NRC model limits the whole body dose to 500 mrem or the dose to any single organ (one of seven body organs) to 1.5 rem, Fetter limits are based on the maximum dose to the whole body only.

Specific activities calculated by the DKR-ICF code were used to calculate the waste disposal ratings for each alloy. The waste disposal ratings for Class A and Class C low-level waste are shown in Table 6.2-V. The 10CFR61 Class A WDR is given after a waiting period of about 10 years to allow for the specific activity of short-lived nuclides

Table 6.2-V.
Waste Disposal Ratings for Several Ferritic/Martensitic Steels$^{(a,b)}$

	HT-9	MHT-9	F82H	MANET-2	LA12TaLC
Class A$^{(c)}$	1.83×10^3	9.56	9.93	2.43×10^3	90.3
	^{94}Nb (97%)	^{3}H (60%)	^{3}H (50%)	^{94}Nb (99%)	^{94}Nb (87%)
Class C$^{(c)}$	178	0.187	0.156	240	8.12
	^{94}Nb (99%)	^{94}Nb (92%)	^{94}Nb (55%)	^{94}Nb (100%)	^{94}Nb (97%)
Class C$^{(d)}$	196	6.62	9.2	264	7.92
	^{94}Nb (90%)	^{192m}Ir (70%)	^{108m}Ag (98%)	^{94}Nb (99%)	^{94}Nb (99%)

(a) For first wall exposed to 1 MW/m^2 neutron wall load for 3 FPY.

(b) In each case, the dominant isotope and its contribution to WDR is given.

(c) Based on 10CFR61 regulations.

(d) Based on Fetter's estimates.

($T_{1/2} \leq 5$ y) to drop below 7,000 Ci/m^3. The 7,000 Ci/m^3 limit is 10 times larger than the limit specified by the NRC for Class A disposal of short-lived nuclides of an unspecified waste form. In comparison with other isotopes for which limits are given for different waste forms, the factor of 10 is used for isotopes contained in metal waste. Since the NRC regulations do not specify any limit for short-lived activity for Class C waste, the Class C WDR values were calculated after a 1-year cooling period for both 10CFR61 and Fetter limits.

Table 6.2-V shows that the IEA modified F82H and the modified HT-9 alloys qualify for Class C according to the NRC limits. None of the steel alloys would qualify for disposal as Class C according to Fetter limits. However, reducing the Ir and Nb impurities in MHT-9 and Ag in F82H by a factor of > 10 would qualify both steels as class C waste according to both NRC and Fetter's limits. Finally, it is important to keep in mind that the waste disposal ratings given in Table 6.2-V are only for the first wall. The corresponding blankets should have lower waste disposal ratings, as they are exposed to lower neutron flux. Disposing the first wall and blanket together should also allow for lower waste disposal ratings than those given in the table.

6.2.5. Key Issues and R&D Needs

Two issues were selected for special attention due to their high degree of uncertainty and/or large impact on the system attributes: loss of ductility and its consequences, and ferromagnetism issues. As a result of the analysis, ductility was viewed as the most serious concern. Ferromagnetism causes important operational problems, but these were viewed as design dependent and soluble.

6.2.5.1. Loss of ductility and its consequences

There are three types of ductility that are used in assessing material performance. The first type that is commonly used in design codes is the tensile ductility, which is measured in the standard tensile test at modest strain rates. A particular measure of ductility, uniform elongation (UE), is used in design codes to classify materials according to ductile (UE $\geq 5\%$), semi-brittle ($1 <$ UE $< 5\%$) or brittle (UE $\leq 1\%$). A second type of ductility is the measure of the uniform strain at failure in a standard creep test, which generally involves strain rates much lower than those used in tension tests. This parameter is important for high temperature operation. The third type of ductility is a measure of the ability of a material to absorb impact loads. As such, it involves high

strain rates. This third type really should be expressed as a strain energy or fracture toughness. However, as the Charpy test is often used, the information obtained is usually given as a ductile-to-brittle transition temperature (DBTT) and an upper-shelf energy (*i.e.*, the maximum energy absorbed when the material is behaving in a ductile mode).

Correlations have been established between Charpy test results and fracture toughness for austenitic stainless steels, but not for ferritic steels. In design codes, the fracture toughness is used to limit the peak stress in the regions of stress concentration. The Charpy test is used to define a nil-ductility temperature which is similar to, but not equal to, the DBTT. The ASME code simplistic rules require that steel pressure vessels be operated at a temperature (dependent on assumed flaw size) greater than the nil-ductility temperature. The Charpy test is also used to monitor the change in ductility of surveillance samples of pressure vessel material as the irradiation progresses. In the following, the ferritic-steel ductility data obtained from tensile tests (UE) and Charpy tests (DBTT) are reviewed. The implications of such data are also discussed.

Tensile-Test Ductility. The uniform elongation of unirradiated Fe-9Cr-1MoVNb and Fe-12Cr-1MoVW generally decreases with increasing temperature from 5%–10% at room temperature to 1%–3% at 550 °C (see Fig. 6.2-9). Above 550 °C, the uniform elongation increases as the material softens. These values are low compared to austenitic stainless steels (20%–30%) in the same temperature range. However, in reviewing the details of the ASME code design rules, such low ductility would not result in a reduction of the allowable design stresses.

Exposure to a neutron environment, particularly in the temperature range of 25–400 °C, results in a loss in ductility of these alloys (Fig. 6.2-10). The decrease in ductility appears to be more significant when the materials are tested in mixed-spectrum reactors, particularly if extra Ni has been added to enhance He production. The data in Fig. 6.2-10 indicated by < 1 He/dpa (1 appm He/dpa) are fast-reactor data, while all other points are obtained after irradiation in mixed-spectrum reactors. The decreases in ductility below 1% would require very careful design analysis to determine if a reduction in allowable stresses would be warranted.

With regard to the uniform elongation of the reduced-activation Fe-9Cr-2WVTa alloys, most of the data reported in the literature pertain to total, rather than uniform, elongation which makes comparisons difficult. However, one reported data set shows that after irradiation in a fast-neutron spectrum (FFTF) at 420 °C, the uniform elongation is 3%–8%. These tests would not include the effects of any significant He generation, nor would they be indicative of the behavior at lower temperatures.

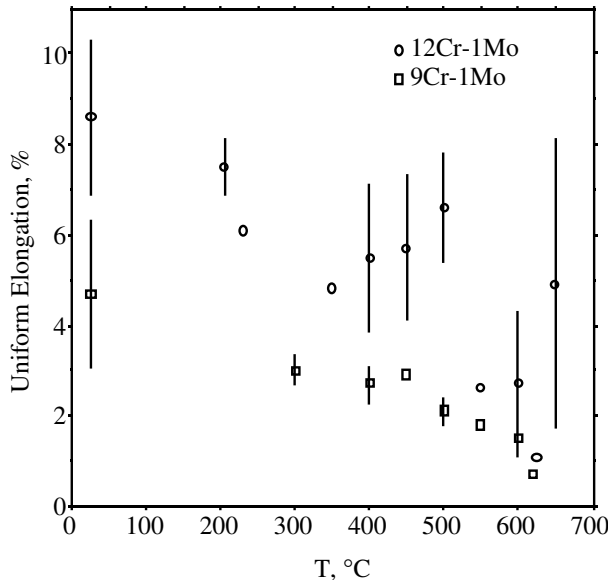

Figure 6.2-9. Uniform elongation as a function of temperature for unirradiated ferritic steel alloys Fe-12Cr-1MoVW and Fe-9Cr-1MoVNb. Results include many different heat treatments and variations in the details of the chemical composition.

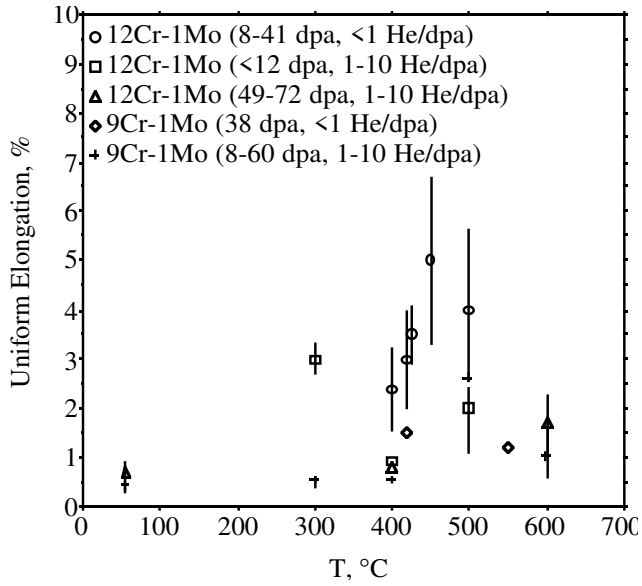

Figure 6.2-10. Uniform elongation as a function of temperature for irradiated ferritic steel alloys Fe-12Cr-1MoVW and Fe-9Cr-1MoVNb. Results include many different heat treatments and variations in the details of the chemical composition.

Ductile-to-Brittle Transition Temperature (DBTT). The DBTT for unirradiated Fe-12Cr-1MoVW alloys falls into the range of –50 to 0 °C. For Fe-9Cr-1MoVNb, the range is –80 to 20 °C. The results are highly dependent on the thermo-mechanical heat treatment used during fabrication and the size and shape of the specimen. The Fe-(7–9)Cr-WVTa have some of the lowest DBTTs reported for ferritic steels: –40 to –90 °C, which is part of the reason for such optimism regarding these materials.

The DBTT values for irradiated materials are somewhat perplexing in that there appears to be a strong correlation between the increase in DBTT and He generation, as well as neutron damage measured in displacements per atom (dpa). Fig. 6.2-11 shows a wide range of data with the Fe-12Cr-1MoVW irradiated at 400 °C with 1–10 appm He/dpa having a DBTT value as high as 330 °C. In general, most data points are below 250 °C. It is encouraging to note that the reduced-activation Fe-9Cr-2WVTa shows no significant increase in DBTT for irradiation up to 13 dpa with negligible He generation. To add to the complexity of trying to interpret the effects of helium generation, more recent data at $\leq$ 2.5 dpa and $\leq$ 3.5 appm He, show increases of 150–180 °C in DBTT after irradiation at 300-400 °C for Fe-12Cr-1MoVW and 60–75 °C for Fe-9Cr-1MoVNb under

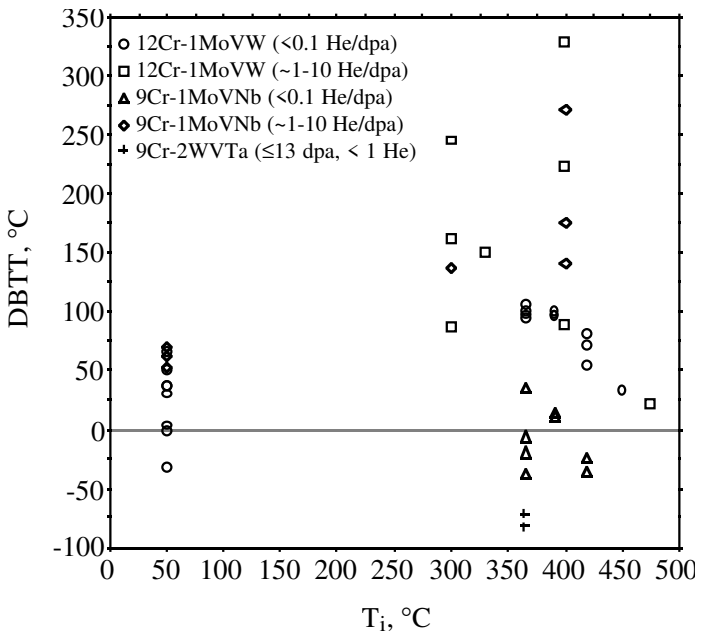

Figure 6.2-11. Ductile to Brittle Transition Temperatures (DBTT) for Fe-12Cr-1MoVW, Fe-9Cr-1MoVNb and reduced-activation Fe-9Cr-2WVTa ferritic steels irradiated to neutron damage levels of $<$ 43 dpa and He contents $<$ 400 appm. He contents are in appm.

the same conditions [7]. The resulting absolute values of DBTT are 100–150 °C for the Fe-12Cr-1MoVW alloy and 30–45 °C for the Fe-9Cr-1MoVNb alloy.

The design consequences of a high DBTT are serious because based on ASME guidelines, the minimum operating temperature would have to be set at a higher temperature, which is dependent on wall thickness and assumed undetected crack length. The issue of allowable stresses would have to be examined carefully to determine the effects of reduced tensile ductility on operating load limits. There would still be some concern about the behavior of such a material during shut-down to room temperature. In addition to shut-down stresses (*e.g.,* reversals in thermal stresses and residual stresses caused by creep and plastic deformation), there is the possibility of seismic or other loads during shut-down. Thus, although it is not a strict design code requirement, the "safety margin" increases significantly as the DBTT is decreased to below room temperature.

There are two approaches to the DBTT problem that are being pursued. The E.U. team is considering the possibility and desirability of heat treating the steel periodically to 400–500 °C during shut-down to partially anneal out some of the irradiation-induced hardening. The other approach, which is the one being adopted by the IEA Working Group, is to optimize the chemical composition and thermo-mechanical heat treatment to decrease the irradiated DBTT value. Success has been achieved in doing this up to 30 dpa at 365 °C in a fast-reactor environment. It remains to be demonstrated that the DBTT values remain low to higher neutron damage levels with He generation and down to lower operating temperatures. Progress also can be realized in this area by using fracture toughness data in place of Charpy DBTT data and the sophisticated ASME design criteria in place of the simplistic rules.

6.2.5.2. Ferromagnetism issues

Another family of concerns regarding the use of ferritic steels in magnetic fusion is related to the interaction of ferromagnetic materials with magnetic fields. The concerns include effects on field ripple, perturbations of the poloidal field, and magnetic loads on the structure. Each of these issues has been investigated previously [18] and the results of those previous studies are summarized here. In general these studies have concluded that proper design can mitigate these issues, such that they should not be considered as feasibility concerns, but rather R&D issues. These previous studies did not consider certain important issues, so areas of future work are identified at the end of the section to guide design studies which choose to adopt ferritic steels as a structural material.

Field ripple. Field ripple (non-uniformity in toroidal field) occurs in all toroidal systems because the toroidal field coils are discrete. The concern with the use of ferritic steel structures in tokamaks is that the ferromagnetic materials will enhance the ripple. If this increase is significant, particle losses will be enhanced and the disruption frequency may be increased.

Lechtenberg *et al.* [18] have conducted sample ripple calculations for three conceptual designs: STARFIRE [10], TNS [19], and ETF [20]. These calculations incorporated a ferritic steel which had a saturation magnetization of 1 T which was reached when the ambient field was 2 T. A square blanket penetration of 0.5 m was included in the analysis. For these designs, the ripple peaked at around 0.2% with a non-ferromagnetic blanket and substituting a ferromagnetic blanket increased the peak to around 0.3% (with the penetration included). An axisymmetric ferromagnetic blanket caused no discernible difference in the ripple. It is the penetrations – asymmetries – that cause perturbations in the field ripple. It was concluded this level of increase in the ripple is not significant.

Poloidal field perturbation. A related effect of the use of ferromagnetic materials in tokamaks is the perturbation of the poloidal field. Lechtenberg *et al.* [18] found that poloidal field perturbations peaked at approximately 3% when a ferromagnetic blanket was added to STARFIRE. They concluded that this is excessive but active control of the poloidal field coils could alleviate this problem. They further concluded that this would not add complexity to the tokamak design because tokamaks would probably include active poloidal field control for plasma stability and position control. An additional concern here is the delay of the control field penetration caused by the ferromagnetic structure. As before, this concern is thought to be alleviated by the saturation of the steel magnetization. This issue is included in the list of action items at the end of this section, because there is no clear evidence that a 3% perturbation in the poloidal field is acceptable. Realistic limits for poloidal field variations must be determined.

Ferromagnetic loads. The use of ferromagnetic materials in tokamaks introduces a set of loads that are not an issue for other materials. These are the magnetic loads induced on the structure by the magnetic fields in the device. Simple, cylindrical models of STARFIRE and ETF have been derived; they predict static magnetic pressures of approximately 0.5 MPa in the ferromagnetic structure. This should be easily manageable in a tokamak blanket. Unfortunately, the issue cannot be dismissed this easily. Of greater concern are the forces induced on pipes and ducts which pass through regions of high field gradients.

Lechtenberg *et al.* [18] calculated the stresses on a coolant pipe passing between the outer legs of the toroidal field coils. The magnetization field was calculated using the GFUN3D code and the stresses were calculated using MODSAP, a finite element code. The pipe was assumed to be 4 m long, with an 8.25 cm outer diameter and a 0.75 cm wall thickness. The material used was HT-9. The distance from the pipe to the center of the adjacent magnet was varied from 80 to 140 cm. At a distance of 86 cm from the magnet center, the calculated force in the pipe peaked at approximately 7,000 N/m, with the force acting transverse to the pipe and with the peak force occurring about 50 cm from one end of the pipe.

The stresses induced in the pipe by these forces are calculated to be approximately 175 MPa. This is a substantial stress for HT-9 structures. Fortunately this stress can be reduced by providing additional supports to the pipe. In fact, addition of a single support at an optimal location in the pipe reduces this stress to less than 30 MPa. This is a reasonable stress and should not appreciably affect the life of this component. These forces and their associated stresses can be further reduced by moving the pipe further from the center of the adjoining magnet.

Issues Requiring Further Study If future design studies consider the use of ferritic steels, the following issues should be clarified in order to ensure reliable and effective use of these materials:

- The effect of realistic blankets on field ripple should be assessed. This should include asymmetries and realistic penetrations.
- The allowable perturbation in the poloidal field should be determined.
- The interaction of the transient magnetic fields, *e.g.,* during start-up and disruptions, with the ferromagnetic structure should be assessed (*e.g.,* forces, delays in field penetration, impact on the vertical stability feed-back system).
- The loads and stresses on a realistic blanket and associated ducting, piping, and manifolds should be re-evaluated. This can be done with existing, commercial finite element codes.
- The stored energy associated with the magnetization of these materials and their effects on source terms for safety calculations should be assessed.

6.3. VANADIUM DESIGNS

6.3.1. Overview

Vanadium alloys have been included in many fusion R&D programs throughout the world due to their potential for improved thermomechanical performance, safety advantages, and possibly longer lifetime. As with ferritic steel designs, our assessment considered the ability of vanadium-based designs to meet the essential mission requirements of a fusion Demo, as well as the uncertainties which currently exist.

The use of vanadium restricts the use of some materials (such as for the coolant and breeder) due to compatibility. For example, water is not considered a viable candidate as the coolant. Design options using both lithium and helium as coolant are described and used for the assessments of the first-wall and blanket, divertor, shielding and heat transport loop.

The assessment of blanket options concentrated on the use of lithium as breeder. Two coolant options were considered: self-cooled lithium and high-pressure helium. Several previous design studies [1, 3, 21–24] have provided detailed descriptions of the self-cooled concept, such that only a cursory review of the design concept is repeated here. The He-cooled blanket option is relatively less studied, and therefore a much more thorough description of that class of design concepts has been provided. Liquid Pb-Li is a possible candidate for the breeder and/or coolant, but U.S. R&D programs do not currently support this option.

Three power plant requirements were selected for more detailed examination. First, the estimated high cost of vanadium is a major concern. The improved performance must offset the higher capital and replacement costs for the in-vessel components (as compared to steels). Strategies for minimizing the quantity of vanadium, maximizing the lifetime and replacing (or recycling) components are addressed. Second, accident safety and waste management are examined to determine whether the Demo requirements can be met. Finally, reliability and availability are briefly surveyed. All design concepts will have a difficult development path to meet the very stringent utility requirements on availability.

Three of the critical issues associated with the use of vanadium have been examined. The materials data base for vanadium alloys is small, but growing. An extensive review of the state of our knowledge of vanadium properties is provided in Sec. 6.3.3 and in the Appendix. Some of the important material-related issues include tensile and creep

behavior under irradiation, compatibility with coolants and breeders, and fabrication. Tritium recovery and control is the second issue examined. Recovery methods from lithium have been developed, but the stringent requirements for impurity control (to prevent degradation of the vanadium properties) leads to special concerns. Finally, the possibility of vanadium recycling was explored as a possible means to offset the high cost of the material.

While uncertainties in the potential attractiveness of vanadium systems is acknowledged, it was decided to develop the V/Li system for the detailed conceptual design phase which followed these assessments. The ultimate potential of fusion depends on our ability to provide high performance systems with minimal safety and environmental impacts. Vanadium systems appears to offer the chance to meet this challenge.

6.3.2. Design Options

Several systems in the fusion power core may use vanadium structure, including the blanket and first wall (Sec. 6.3.2.1 through 6.3.2.3), divertor and other plasma facing components (Sec. 6.3.2.4), shield (Sec. 6.3.2.5), and primary heat transport loop (Sec. 6.3.2.6).

6.3.2.1. Self-cooled lithium blanket design

The self-cooled lithium breeder blanket with a vanadium alloy structure has been evaluated as the reference design of many studies [1,3,21–24]. This concept provides several inherent characteristics that enhance the attractiveness of fusion as an energy source. Since lithium serves as both breeder and coolant, a simple integrated first wall/blanket design configuration with a single pass, poloidally oriented coolant flow has been developed. This concept makes use of an electrically insulated coolant channel to reduce the MHD-related pressure drops. This provides for a low pressure blanket and heat transport system which, combined with the simple configuration, should substantially contribute to high reliability. All in-core complexity related to tritium recovery is eliminated since tritium can be recovered from a small side stream off the external coolant loop. Also, concerns relating to coolant-breeder interaction are not an issue with lithium both as breeder and coolant.

The lithium-vanadium system also provides several inherent safety features. Because of the very high solubility of tritium in lithium, containment of tritium during normal operation does not appears to be a critical issue. Also, the relatively high tritium concentration in lithium ($\sim$ 1 appm) results in a modest size of tritium recovery system.

The low blanket pressure (< 1 MPa for design with insulator coating), high heat capacity, and thermal conductivity of lithium and relatively low afterheat in this system provides substantial advantages in the event of a loss-of-flow accident (LOFA). Design solutions developed to improve safety include the use of an inert gas to eliminate lithium-air reaction and the use of a lithium-cooled shield and in-vessel components to eliminate potential lithium-water reaction.

As in all systems, the vanadium-lithium concept exhibits a few inherent characteristics that must be accommodated by special design solutions to provide an attractive engineering system. Dominant among those are: (1) Chemical reactivity of lithium with air and water, and (2) Liquid-metal MHD effects. Lithium at high temperatures will react with water and air. This is the inherent chemistry of lithium and cannot be changed. However, there are design solutions to minimize the occurrence of those accidents. The use of inert cover gas and the elimination of water from the power plant core will reduce the possibility that these reactions will occur. Even if those reactions happened, the consequence may be acceptable. Detailed analyses of lithium fires have been carried out in the past using the LITFIRE code. The conclusion was that the temperature would be raised to ∼1,000 °C in a lithium-air fire. All safety evaluations were based on this temperature excursion. Even with those conditions, a high safety rating was achieved.

The MHD effects associated with the motion of a conducting liquid metal in a conducting coolant channel result in a pressure drop. This pressure drop is proportional to the wall thickness. Thus, increasing the structural fraction to accommodate the pressure will be of no use, since the pressure drop only increases further. In typical tokamak power plant designs, the MHD pressure drop for the inboard regime of a tokamak results in pressure stresses beyond the material limits. To reduce this MHD pressure drop, some form of insulating wall is required, either with a direct coating or with a sandwich-type structure. The reference design for the U.S. ITER breeding blanket and ARIES-II both have a direct coating. This coating development is still in a very early stage.

The cross-section of a Li/V blanket is shown in Fig. 6.3-1. The first wall is a continuous 2-mm thick plate. The first wall coolant channels are rectangular ducts 10 mm × 50 mm in cross section. The radial direction of the first wall channel must be made as small as possible to improve heat transfer. (If MHD turbulence can improve heat transfer, the dimension of the first wall channel could be relaxed.) The radial dimension of the back channels can be much larger. The velocity in the breeding zone ducts decreases with increasing radial position. This provides a uniform coolant exit temperature. Tailoring of the velocity to the location of the zone can be accomplished with ducts whose radial dimension increases with distance from the first wall.

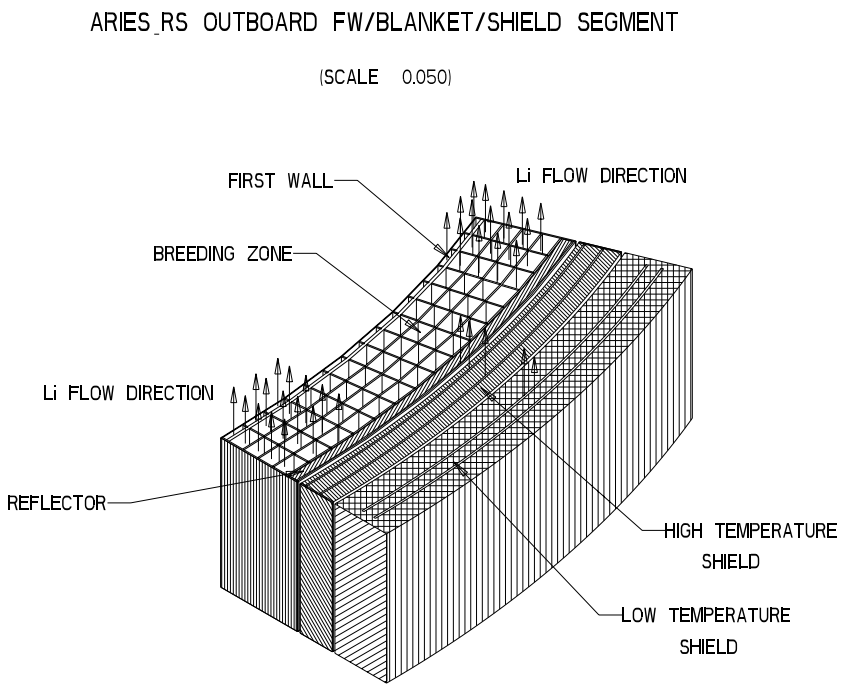

Figure 6.3-1. Cross-section of a self-cooled, lithium/vanadium blanket.

A major advantage of a self-cooled system, as depicted in Fig. 6.3-1, is that there is no heat transfer surface inside the blanket. The fusion energy is directly deposited within the coolant, that the design of a heat exchanger within the confines of the blanket geometry is not required. Also, the only pressure containment surface will be the first wall. Thus, the frequency of coolant leakage can be greatly reduced. This effect will be discussed later in this report.

6.3.2.2. Helium-cooled blanket design

The motivation for the use of helium as the blanket coolant is its potential for high thermal efficiency, safety, and waste disposal advantages. Helium has thermodynamic and transport properties that allow high temperature and hence high efficiency operation. It is a natural match with the Brayton power conversion cycle. Helium chemical inertness and non-activation significantly reduce the risk of chemical safety and coolant waste disposal. In order to realize these advantages, the design must overcome the relatively low volumetric specific heat of helium, which usually leads to a high-pressure system. When combined with the use of V-alloy, the design must also successfully address the issue of coolant impurity control.

Three representative helium-cooled blanket designs have been reviewed for use with V-alloy. They are the helium-cooled ITER blanket design, the reference Safety and Environmental Assessment of Fusion Power [26] blanket design and the helium-cooled, lithium breeder V-alloy (He-Li-V) design developed for this study.

The helium-cooled, V-alloy blanket proposed for ITER [25] is similar to that illustrated in Fig. 6.3-2. It is a poloidal flow co-axial tube, molten Li-breeder design, with narrow modules that could fit the narrow vertical maintenance opening of the 1993 ITER-EDA design. This design focused on addressing the question of reliability when high pressure helium (18 MPa) is used. All piping joints are located outside of the vacuum vessel. Co-axial tubes were used to increase design reliability. Both tubes are designed to take the full helium pressure and only the inner tube was pressurized. The annulus between tubes was filled with liquid metal (Na or Li) for leak detection. It addresses many of the design issues, but not the issue of material compatibility between V-alloy and helium impurities.

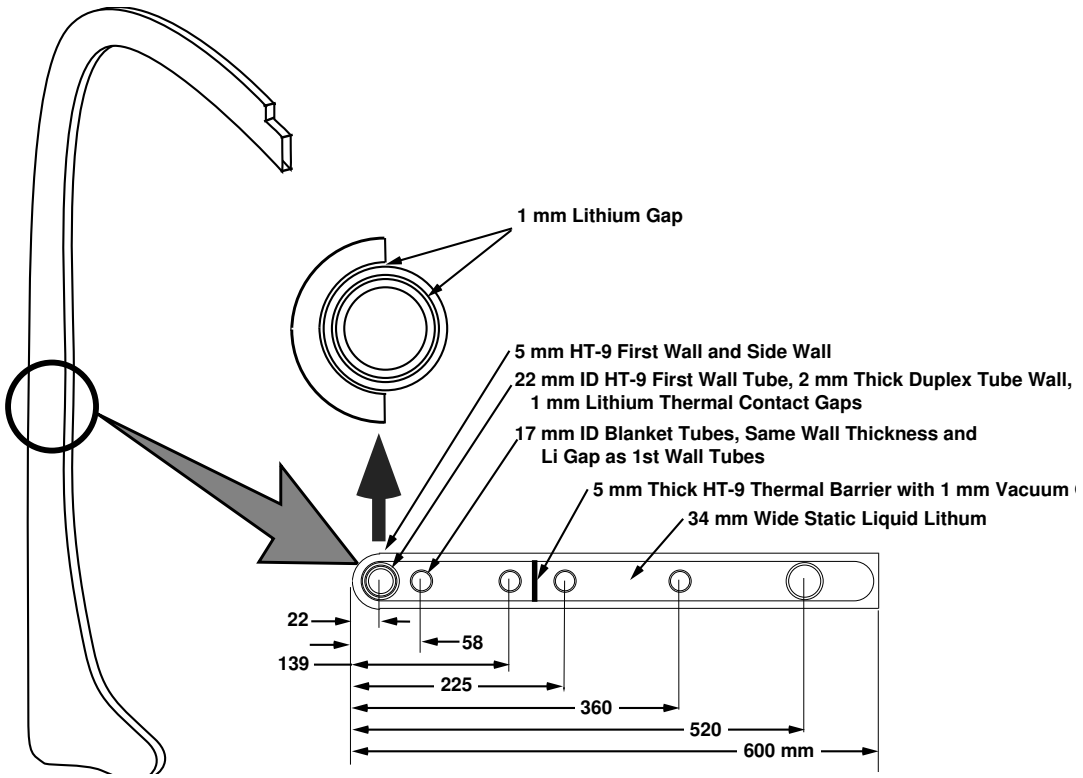

Figure 6.3-2. The He-Cooled ITER Blanket Module which uses HT-9 as structural material (a similar V-alloy design has been developed).

The second design is the reference design for the SEAFP reactor study [26]. This is a poloidal flow, co-axial tube, Li_2O breeder-in-tube (BIT) design, as shown in Fig. 6.3-3. As indicated, the solid breeder Li_2O is also used to fill in the space between the tubes. Helium coolant flows in the annulus between the co-axial tubes. The key focus of the SEAFP design is to ensure public acceptance and take into account the operating requirements of utilities. The issue of material compatibility between Li_2O/V-alloy and helium impurities/V-alloy is proposed to be resolved by a coating of sub-micron thick SiC or Al_2O_3.

The third design is cooled by helium and uses liquid lithium as the breeder (He-Li-V). This design is discussed in detail in the next section. Selected parameters of Ref-SEAFP and He-Li-V designs are given in Table 6.3-I.

Figure 6.3-3. Reference SEAFP design.

Table 6.3-I.
Selected Input and Output Parameters
for the He-Li-V and Ref-SEAFP Designs

	He-Li-V	Ref-SEAFP
Major Radius (m)	6.75	9.4
Minor Radius (m)	1.5	2.09
Fusion power (MW)	1,925	3,000
Average surface heat flux (MW/m^2)	0.336	0.3–0.4
Average neutron loading (MW/m^2)	2.9	2.1
Structural material	V-alloy	V-5Ti
Helium pressure (MPa)	18	9
Outlet helium temperature (°C)	650	560
Power conversion type	Brayton-DCGT	Rankine
Neutron multiplier	None	None
Tritium breeder	Li	Li_2O
Tritium breeding ratio	1.402 (1-D)	1.17 (3-D)
Outboard module width (m)	1.086	1.46
Inboard modules width (m)	1.021	1.44

6.3.2.3. The He-Li-V blanket design

To avoid the problems of compatibility between V-alloy and oxygen bearing materials (*e.g.,* solid breeders), the option of using Li as the tritium breeding material was reviewed. This approach also eliminates all the design difficulties related to the use of solid breeders, such as fabrication of sphere-pac or sintered pellets, uniform filling of solid, loss of volume due to void fraction, radiation damage, solid-to-solid contact resistance, sphere-pac settling, thermal ratcheting effects, and the tritium purge flow system. This

design also takes advantage of the high thermal conductivity of lithium, thereby allowing relatively large spatial separation between cooling tubes.

The He-Li-V blanket is a toroidal flow, single wall tube design as illustrated in Figs. 6.3-4 and 6.3-5. The Li is slowly circulated for tritium extraction and, therefore, MHD insulation may not be necessary. The blanket module consists of blanket boxes connected to the coolant plenum and structural support. As shown, the tube plates can be formed by embedding (sandwiching) the coolant tubes in two V-alloy sheets (*e.g.,* by the HIP process or by diffusive bonding). This is similar to the ferritic steel solid breeder design proposed by Kernforschungszentrum, Karlsruhe [27]. These plates form the support of the cooling tube and are also the supporting structure of the breeder box, including the first wall. Between the cooling tube plates, the module is filled with molten lithium maintained at atmospheric pressure, connected to a common channel, and then to the free surface of each poloidal sector (not shown in Fig. 6.3-5). The coolant is routed from the back poloidal plenum to cool the first wall and then re-routed to cool the rest of the blanket. This routing scheme is selected to optimize the coolant outlet temperature in order to achieve the highest possible thermal conversion efficiency.

A major-radius model neutronics calculation was performed for the He-V-Li design. The material volume fractions were determined after two iterations between the configurational design, scoping thermal-hydraulics and neutronics calculations. Zone 1 (first wall and first layer of breeder) is 3 cm thick for inboard and outboard blankets and Zone 2 (the rest of the blanket) are 28 cm and 48 cm, respectively, for the inboard and outboard blankets. The composition of Zone 1 for both inboard and outboard is 7.3% V-alloy, 79.2% lithium, and 13.5% void. The compositions of zone 2 are 7.0% V-alloy, 91.6% lithium, and 1.4% void. The results indicate that the 1-D tritium breeding ratio is 1.402 and the total nuclear heating is 16.02 MeV per D-T neutron. A detailed radial power density distribution for the outboard was used for the scoping heat transfer calculation.

Based on the neutronics results, scoping calculations were performed to assess the coolant and materials' maximum temperatures and the frictional pressure drops for the blanket and first wall. The primary and secondary stresses of the first wall were estimated by the simple model of a circular tube. Peak surface and neutron wall loading assumptions were used for the maximum temperature calculations. Table 6.3-II shows that the design can meet temperature, structural design, and performance limits.

Figure 6.3-6 shows a schematic of the blanket coupled with a direct helium Brayton cycle for power production. With an outlet temperature of 650 °C, a gross efficiency of 46% can be attained. Reasons for this high value are: (1) No intermediate heat exchange

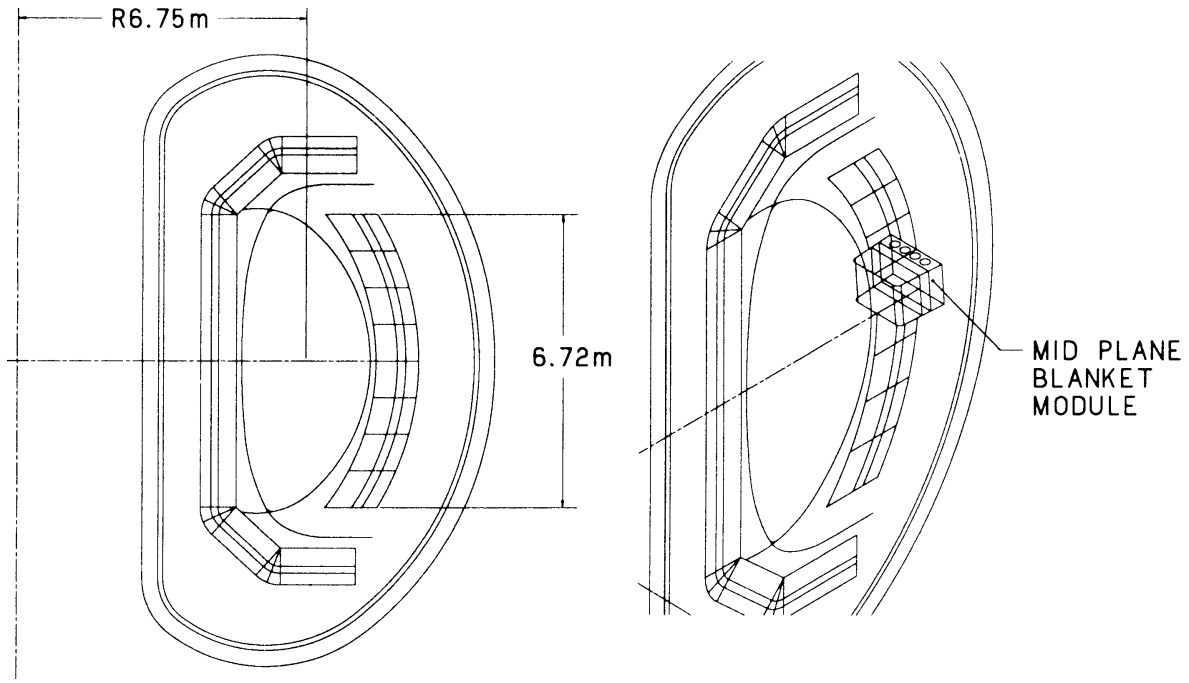

Figure 6.3-4. Cross section of a tokamak with a He-Li-V blanket.

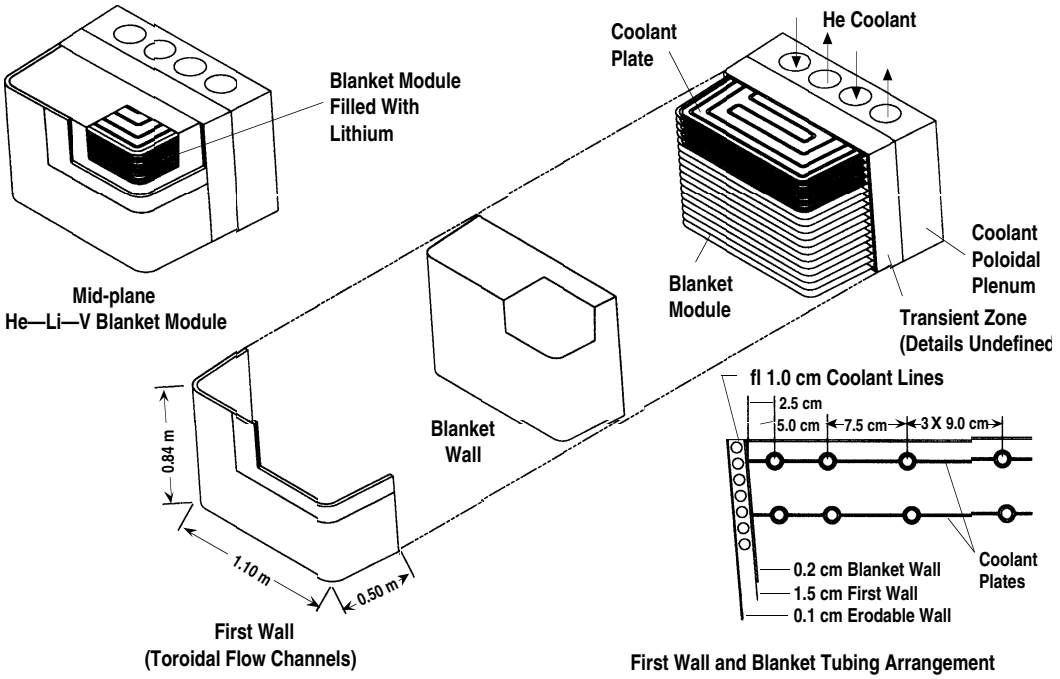

Figure 6.3-5. Details of the He-Li-V blanket module.

Table 6.3-II.
The He-Li-V Thermal-Hydraulic Parameters[(a)]

Helium pressure (MPa)	18.6
Helium inlet temperature (°C)	400
Helium outlet temperature (°C)	650
Surface heat flux (MW/m^2)	0.484
Peak-to-average ratio (outboard)	1.44
Peak-to-average ratio (inboard)	1.0
Neutron wall loading (MW/m^2)	4.83
Peak-to-average ratio (outboard)	1.67
Peak-to-average ratio (inboard)	1.0
Inside diameter of first-wall tubes (mm)	10
Inside diameter of blanket tubes (mm)	15
Tube wall thickness (mm)	2
Blanket side wall thickness (mm)	2
First-wall temperature (°C)	611
First-wall frictional pressure drop (kPa)	52
Blanket front wall maximum temperature (°C)	657
Blanket front wall frictional pressure drop (kPa)	100
First-wall primary stress (MPa)	47
First-wall total stress (primary + secondary) (MPa)	94
Gross thermal efficiency	46%

(*a*) See Fig 6.3-5 for other dimensions.

equipment is required, (2) The high pressure reduces blanket pressure losses, and (3) A 96% effective recuperator with low pressure loss reduces cycle irreversibilities.

One of the main advantages of the helium cooled blanket is its potential to achieve much higher helium outlet temperature and hence higher thermal efficiency. Figure 6.3-7 shows the relationship between gross thermal efficiency and temperature/pressure for a helium cooled blanket coupled to a Brayton cycle. A gross thermal efficiency of 60% can be achieved with a helium outlet temperature in the range of 1,100 °C. This is well within the capabilities of current gas turbines which operate at temperatures in the range of 1,200–1,300 °C. However, it will require an advanced blanket material such as metal matrix composite or improved SiC/SiC composite.

It should be noted that in comparing the Rankine and Brayton cycles, even when they have the same gross efficiency and pumping power, the net thermal efficiency of the Brayton cycle system will be a few points higher since the coolant pressure drop is already included in the DCGT system calculation.

Fig. 6.3-7 also illustrates the importance of gas pressure on cycle efficiency. Above 12 MPa, performance becomes a relatively weak function of pressure. Below that value, the pressure losses through the blanket become a dominant effect. Therefore in the next design iteration, the coolant pressure will need to be optimized for blanket void fraction, gross efficiency, and pressure loss considerations.

Materials Issues Both helium and lithium are compatible with V-alloy through the entire proposed temperature range of the He-Li-V design. However, when helium is used as the coolant with V-alloy, the interaction of impurities in He (O or H) with V-alloy was identified as a critical issue in the BCSS study [1]. There has been no systematic program to address this issue. Some experimental data exist but mostly at relatively high concentrations of moisture ($\sim$ 100 ppm) content, atmospheric pressure oxygen, or air at high temperature. Therefore, it is important to review gas-cooled fission reactor experience and identify the design differences between the fission and fusion power plant in the control of impurity ingress. Two additional approaches can also be applied to mitigate this issue if the conventional method of impurity extraction and control of impurities ingress proved to be inadequate.

Impurity removal. The technology for impurity cleanup in helium coolant loops has been well demonstrated in operating gas-cooled, fission reactors. Experience in the U.S. and Europe has demonstrated systems with reliable cleanup of impurity particulate, moisture, and gases using systems readily available to the blanket cooling application.

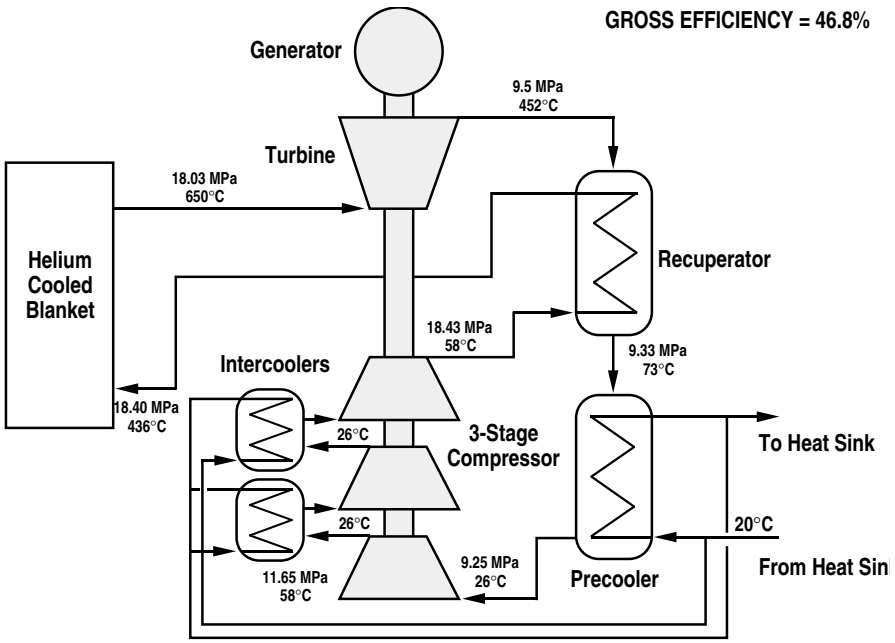

Figure 6.3-6. Fusion Demo Plant Direct Helium Brayton Cycle Power Conversion.

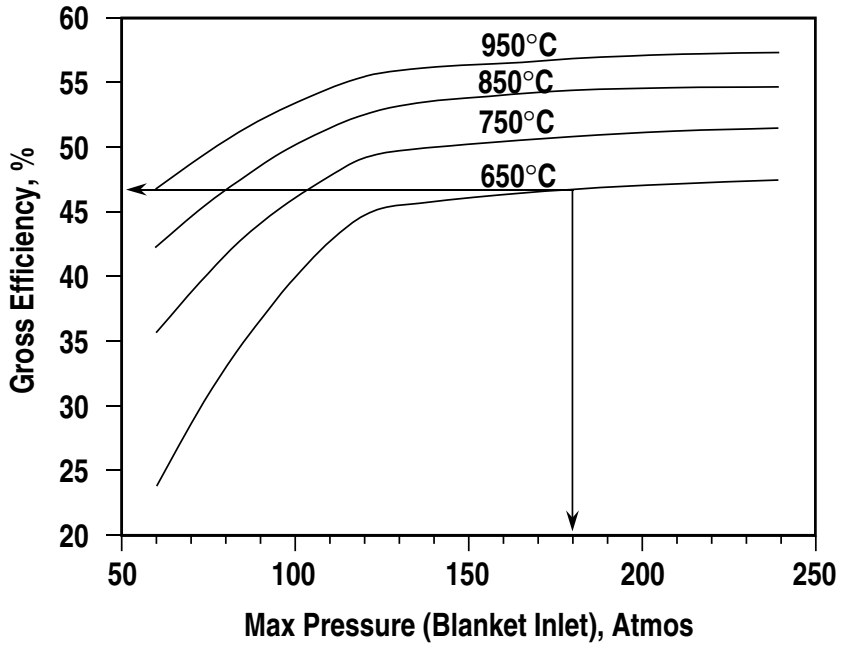

Figure 6.3-7. Demo direct Brayton cycle efficiency as a function of maximum helium pressure and temperature.

The helium purification system takes a side stream of the primary coolant from the discharge of the high pressure compressor discharge, provides essentially 100% cleanup of the helium, and returns the purified coolant to the compressor suction. A typical helium purification train similar to what could be deployed as a part of a blanket cooling system, consists of four factory-fabricated process modules. The modules and their functions are as follows:

- High temperature filter/absorber. The first stage of the purification process consists of an activated charcoal bed followed by a metallic filter elements. Condensible metallic impurities are removed from the helium stream by absorption and chemisorption on the activated charcoal, acting to filter out particulate. Particulate (*i.e.,* dust) is mechanically trapped by both the charcoal bed and metallic filter elements.

- Oxidizer. In the next purification stage, hydrogen, tritiated hydrogen and carbon monoxide are oxidized to water and carbon dioxide for subsequent removal. Oxidation takes place at elevated temperatures as the helium passes through an appropriate catalyst bed.

- Dryer. Water (including tritiated water) and carbon dioxide are essentially completely removed at this stage by a molecular sieve. In the event of high tritium levels, separate water and carbon dioxide absorber cartridges could be utilized.

- Low temperature absorber. The remaining gaseous impurities such as nitrogen and any methane are removed as the He stream passes through a liquid nitrogen-cooled, activated charcoal bed.

Systems processing more than 2,000 kg of helium per hour are well within existing experience base and would provide rapid coolant turnover, perhaps on the order of one to several hours, if so required.

Control of impurity ingress. In addition to cleanup, helium purity is dependent on impurity ingress. Precluding or tightly controlling impurity ingress is requisite to maintaining coolant purity. Experience with U.S. and European helium-cooled reactors have demonstrated the practicality of achieving low impurity levels. Table 6.3-III illustrates observed impurity levels during reactor operations in the five helium-cooled reactors built to date. Impurity sources in these reactors included water from high pressure, high temperature steam generators, impurities within graphite fuel and reflector blocks, impurities

Table 6.3-III.
Impurity Concentrations in Several Helium-Cooled Fission Reactors

	H_2O	H_2
Dragon (U.K.)	0.1	1
Peach Bottom (U.S.)	0.5	10
AVR (Germany)	0.1	10
Fort St. Vrain (U.S.)	< 1	2.6
THTR (Germany)	< 0.01	0.8

trapped within fibrous insulating materials and circulator bearing lubricants (oil or water). Despite the presence of these sources, low impurity levels were achievable in each of the systems. In particular, operating data from the German Thorium Hochtemperatur Reaktor (THTR) (the most recently completed of these plants) shows oxidant (water) levels to be less than their very low measurement threshold.

In a He-V-Li blanket cooling system, each of these sources are eliminated. Steam generators are eliminated by adoption of the high efficiency Brayton Cycle (gas turbine). This system is hermetically sealed to prevent any leakage during operation, but if a leak should occur, helium at a minimum of 9 MPa would leak out rather than air leak in. Molecular counter-diffusion of O_2 through the leak (low pressure) would be insignificant. Likewise, leakage of water from the precooler or intercooler is precluded by the fact that the pressure of the helium (9 MPa) is far greater than the water (0.2–0.3 MPa). Any leak would rapidly be detected by the presence of helium in the water. Graphite blocks and fibrous insulation for the fission reactor are not required in a blanket cooling system. This eliminates significant sources of helium impurities. Finally, the maturation of magnetic bearing technology eliminates the potential for ingress of rotating machine lubricants.

It is likely that there will be oxide contaminated surfaces in the helium system, especially the power conversion system which is constructed from high alloy steels which develop oxide films. This source of impurity will be diminished significantly with the continuous operation of the purification system.

Hence, the lack of ingress sources, coupled with a continuously operating purification system, suggests that impurity levels very much lower (perhaps several orders of magnitude) than those observed in helium-cooled reactors might reasonably be expected.

Surface modification. Since at this time there is no experimental data to demonstrate the equilibrium concentration of low level impurities in the helium primary loop of the He-V-Li blanket design and the sensitivity of V-alloy compatibility in this environment, it is reasonable to investigate various ways to mitigate the problem if warranted.

A possible way to make the V-alloy compatible with impurities is by way of surface modification. Surface modification to address V-alloy chemical compatibility has been investigated by various scoping studies [28–30]. In one case, aluminum was used to modify the surface of V-5Cr-5Ti to make an Al rich surface region of the V-alloy. This aluminized V-alloy had dramatically increased oxidation resistance at temperatures to 575 °C in air when compared to standard V-5Cr-5Ti material [28]. At 575 °C, the parabolic oxidation rate for aluminized V-5Cr-5Ti was 1/7 the rate as that observed for V-4Cr-4Ti. In another case, chromium surface modification was used for a V-15Cr-5Ti alloy to dramatically increase oxidation resistance, relative to standard V-15Cr-5Ti, upon exposure to He containing 100 vppm H_2O at temperatures to 650 °C [29,30]. Chromium surface modified V-15Cr-5Ti gained 2% as much weight as V-15Cr-5Ti upon exposure to He containing 100 vppm H_2O at 650 °C for 400 h. Studies such as these show the merit of surface modification of V-alloy structural material to enhance chemical compatibility.

It can be envisioned that for surface modification, if necessary, 10–20 μm layer of Si, Al or Y can be surface impregnated to the V-alloy surface facing the high pressure helium. Silicon and aluminum are semi-metals whereas yttrium is a refractory metal. Silicon is an attractive element with regard to surface modification of V-alloy material because of its high melting point and because, once SiO_2 is formed on silicon from surface oxidation, the SiO_2 layer is self-protecting. Silicon oxide does not allow oxygen to penetrate and react with underlying silicon metal. In addition, silicon oxide is a fairly impermeable barrier to hydrogen and does not react with hydrogen [30].

Aluminum will behave similarly to silicon if used as a protective surface barrier for the V-alloy. Aluminum is more ductile than silicon, however aluminum by itself melts at 660 °C. Yttrium is more of an unknown with regard to use as a surface barrier to prevent chemical attack of V-alloy material. Yttrium does form very stable oxides that may be self-protecting for underlying material as is the case with silicon. It has already been shown that V-alloy material can be produced successfully to have a 5–15 μm Al rich surface layer [28]. Surface aluminized V-5Cr-5Ti prepared by ANL showed a reduction

in tensile ductility from 23% to 13% and no catastrophic embrittlement of the alloy after exposure for 1000 h at 500 °C in air. This preliminary result is very encouraging for surface modified V-alloy structural materials.

Oxidation resistant V-alloy. Another approach to make the V-alloy compatible with impurities is to develop an oxidation resistant V-alloy. Researchers have already experimented with additions of up to 1% by weight Si, Al, and Y to bulk V-5Cr-5Ti and V-15Cr-25Ti materials [31]. They have observed a degree of solution-strengthening and enhanced oxidation resistance for these bulk modified V-alloys based on measurements performed. Oxide layers formed during exposure to pure O_2 at 400 °C were found to be cohesive during this work.

Design with High Pressure Helium. A system pressure of 18 MPa is relatively high but by no means unusual by modern industrial standards. For example, hundreds of superheated steam systems operate in the range of 17–20 MPa and supercritical steam systems operate in the range of 24 MPa. Natural gas line pumping units operate at pressures to 27.5 MPa.

Two considerations are very important. First, the incidence of small leaks must be very low. Second, if a small leak occurs, it must not rapidly propagate to a large leak before action is taken. It is important to note that the probability of a leak is a weak function of gas pressure. Rather, it is mainly a function of the incidence of undetected critical flaws and a crack propagation mechanism such as creep or high or low cycle fatigue. Stresses from these mechanisms are much greater than primary (pressure induced) stresses. Current design practice, used in the utility and process industries, employs established calculational procedures to determine critical flaw sizes and inspection techniques to detect the presence of critical flaws. This approach has resulted in highly reliable operation of high pressure systems.

There are at least two methods to evaluate the probability of failure. The first method is used when we have neither the design nor the necessary properties of the relevant material. The failure rate is projected from the operating experience of similar combinations of materials and design conditions. The usefulness of the result to a specific design depends very much on the assumptions made in the extrapolation of data. The second method is to use projected irradiated properties of the relevant structural material and to use fracture mechanics to project the result. The accuracy of the second method depends on the degree of conservatism in selecting the key material properties.

T. D. Marshall [32] used the first method to evaluate the failure rates of the in-vessel ITER tubing made of different materials and coolants. Operating experience failure rates and data for Nb and Ti were used to represent Zr and V. Failure data for Ti and water coolant and reliability K-factors were used to make a projection for the vanadium and helium system. An average failure rate of 3.1×10^{-10} (m-hr)$^{-1}$ and an average rupture failure rate of 3.1×10^{-11} (m-hr)$^{-1}$ were found for water, helium, and lithium as coolants and from Be to Zr as structural materials including V-alloy.

A more specific evaluation based on the second method was performed by General Atomics on a similar helium-cooled, V-alloy design. The "leak-before-break" assessment utilized by the utility and process industries was used to evaluate the probability of rupture [33]. This leak-before-break assessment should be applied to any pressurized cooling media, including the lithium self-cooled option. The approach is to show that an incipient leak can be detected and terminated before a large rupture occurs. From knowledge of the baseline condition of the component and type of failure mechanisms, material properties and anticipated operating loads can be used to predict the distribution of times between crack initiation from a given flaw size and leak and between leak and break. This enables us to design our in-service inspection procedures and safety instrumentation to prevent ruptures from occurring in key components (*e.g.,* fissile reactor primary coolant piping or vessels, and the divertor, blanket and first wall for the fusion system).

In 1993, General Atomics applied the technique of leak-before-break assessment on the helium-cooled blanket design for ITER [33]. The material used was V-alloy, the helium pressure was set at 20 MPa, and the helium-cooling tubes were designed to 100,000 full power shots. This large number of cycles is a much more severe requirement than what is required for our Demo design, which should be much less than 50 cycles for a 5-year life first wall. In this ITER blanket design exercise, conservative assumptions were made in the calculations of crack propagation. A value of K_{IC} reduced by irradiation to 40 MPa-m$^{1/2}$ was assumed for the critical crack length calculation. (This is the irradiated lower shelf value for HT-9. It is a conservative value for V-alloy because of its superior ductility at higher temperature.) Analyses were performed for different ITER tubes at different loading conditions. The surface loadings were for the cases of 0.35 and 1 MW/m^2. Results showed that an initial undetected flaw of less than 0.9 mm depth would not produce leakage in less than 100,000 cycles (*i.e.,* each burn cycle equal to 1000 s). This is a large initial flaw and can be assumed to have a very low probability of occurrence because manufacturing techniques and quality-control (QC) inspection would not allow such a flaw to exist in the base material. In addition, results also showed nearly all the failure scenarios met the leak-before-break criteria. Only in the case where the co-axial

tube inter-space was pressurized (20 MPa) and the loading was 1 MW/m^2 would brittle failure result (*i.e.,* tube burst, fracture toughness exceeded). No threshold K_I was used, *i.e.*, crack growth was assumed to occur even at very low stress levels. These results are encouraging, especially when applied to the less stringent Demo design, with considerable fewer cycles. It indicates that a robust design can be achieved by ensuring that both fracture mechanics and ASME Boiler and Pressure Vessel code requirements are met.

Therefore, under normal operating conditions, the following general observations can be made:

1. Helium will not leak unless there is a physical hole or crack; *i.e.*, no leakage can occur by diffusion.
2. A cost-effective non-destructive inspection technique must be available (*e.g.,* ultra sound or computerized tomography with further development to reduce cost) to examine all the key pressure bearing components before, during, and after installation. (Such inspection techniques are available with the capability of detecting axial and circumferential flaws of 0.1 mm in weld and base metal tubes and components.)
3. The leak-before-break condition must apply to both tubes and joints.
4. The key to this design approach is to have reliable irradiated material data (where K_{IC} is the most important property) needed to carry out the leak-before-break assessment. Before this material data is available, parametric studies can be performed to scope the problem for different design options.

Detection of helium leakage. To ensure the application of the leak-before-break technique and to avoid cooling tube bursting, it is necessary to derive a detection technique for helium leakage for the He-Li-V design.

At 2000 MW of fusion power, helium is generated in the lithium breeder at the rate of 406 g/d, *i.e.*, about 0.0047 g/s. Therefore, it may be difficult to detect small leaks by monitoring the helium levels in the Li breeder. One solution is to add dopant to the primary coolant. However, no doping materials have been identified that will be reliable and will not add significant radiation into the coolant stream. From the technique of leak-before-break scenarios, it may be possible to detect the amount of additional helium ingress from the coolant stream without reaching the critical flaw size of about 0.9 mm. Based on the observation that the helium leakage rate is proportional to the flaw characteristic length squared, a flaw size in the range of 0.1 to 0.5 mm diameter (less

than the critical flaw size of 0.9 mm) will lead to a helium leakage rate in the range of 0.05 to 1.2 g/s, respectively. This means that helium leakage from the primary coolant can be detected based on the much larger generation of helium from the leaking tube before the flaw size becomes critical. The response time for leak detection and termination will have to be verified and coordinated with a specific blanket configuration and the response of the passive fail-safe fast-activating valves.

Impact of tube rupture. As part of the safety evaluation, even with the low probability of helium leakage and the fast response of leak detection without leading to any tube breakage, the scenario of tube failure still needs to be evaluated. This is to show that, even with a tube failure in the blanket, the consequences are acceptable within anticipated low frequency of occurrence.

Two approaches can be taken to design for the possibility of tube rupture. The first one is to design the blanket structure to withstand the full helium pressure. This approach is taken by the European DEMO BOT, ferritic steel, solid breeder blanket design [27], operating at a gas pressure of 8 MPa. For the He-Li-V design, an 18-MPa blanket module would have to be configured to withstand this pressure for a duration shorter than or equal to the response time for valving off the failed blanket module without catastrophic investment impact. With the higher strength and lower neutron absorption of V-alloy over ferritic steel, this approach may be credible. Note that the selection of 18 MPa helium pressure is a scoping design point. Various trade off studies will need to be performed between helium pressure and performances of different areas, *e.g.*, thermal hydraulics, neutronics design, structural design, and economics.

The second approach is to design the module with a plenum and relief mechanisms to minimize damage (if any). For this approach a free surface of liquid lithium could be used and a dump tank of lithium could be envisioned to delay the impact of module over-pressurization. The viability of this approach may be in question due to the same liquid metal MHD effect that is hindering the lithium self-cooled design. Very possibly some local damage can occur. It will still be tolerable provided the frequency of occurrence is low (0.001/y). Based on the robust design approach, this frequency of occurrence should be achievable.

Furthermore, we must show that a tube failure inside the blanket will not cause major investment damage (damage that will cause major downtime of a year or more). The blanket module design consists of 1,760 tubes, with inner diameters of 1.5 cm and length of 2.5 m. The tubes are manifolded in two groups with fail-safe isolation valves. Passive isolation within 0.1–0.5 seconds should be achievable according to instrumentation experts from General Atomics. If a tube rupture occurs, helium will flow into the module,

causing distortion. The total helium leaked is determined by the leakage until the valve closes and the equilibration of the volume in the tubes with the volume in the module. Assuming a pressure of 8 MPa (taking the Ref. [27] helium-cooled design as an example) of the limit which would not cause catastrophic burst of the module, the total volume of helium leaked into the module at 8 MPa is ~ 0.5 m^3. Most of the leakage occurs from helium within the system coming into equilibrium. This means that the module would deform by 0.5 cubic meters. This volume deformation is about 11% of the total volume of the 1 m wide, 0.5 m deep, and 8 m high module. We have to design for the lithium displacement of this volume before a configuration change of the module would occur. This requirement does not seem to be excessive, but it will have to be demonstrated.

Consequence of helium release into the confinement building. For complete safety evaluation, the potential consequences of a complete loss of helium volume should be analyzed. An estimate can be made by scaling the results from the ITER design [25]. For this ITER design, preliminary safety assessments of various pipe failure conditions were performed. At a system helium pressure of 19 MPa, with a volume of 150 m^3, T_{in} at 35 °C, and T_{out} at 350 °C, the energy content is 4.2 GJ. The helium volume at atmospheric pressure is 28,000 m^3. Assuming an ITER crane hall volume of 150,000 m^3, the pressure in this hall after release of helium is < 19 kPa (without any relief), and the confinement building would be at < 35 °C.

Based on the above, we can make estimates for the Demo design as follows. The blanket He volume is ~ 120 m^3. External systems are included by doubling the inside volume to 240 m^3. With a 150,000 m^3 confinement hall volume [25], the pressure on the wall will be < 31 kPa. The energy content is ~ 5.3 GJ. Therefore, the confinement building temperature following a complete loss of coolant will be ~ 39°C. If the entire helium coolant is leaked into the vacuum chamber (with a volume of 3,300 m^3), the helium pressure would be 1.4 MPa which is large but not excessive. To mitigate the potential damage, a passive pressure release valve can be designed into the vacuum system if necessary.

Maturity of helium-cooling technology. Commercial fission gas-cooled reactors have been operating in Europe and in the U.S. for more than 1,000 reactor-years (primarily CO_2), providing experience with gas circulators and heat exchanges. In addition, five helium Brayton cycle systems have been constructed and operated. Developmental helium-cooled reactors like Peach Bottom were successfully demonstrated and a commercial reactor has been operated. High temperature helium test loop experience has been obtained in facilities in the U.S., Japan, Germany, Russia and France. These indicate the technology of helium-cooling is relatively matured. Even though the development

of gas-cooled commercial fission reactors has been relatively slow, considerable advances have been made in the last 20 years. This can be understood from the development of the passively-safe Modular High Temperature Gas-cooled Reactor (MHTGR) and the Director Cycle Gas Turbine GT-HTGR reactor designs. For the development of a gas-cooled Demo design, we should be able to take advantage of the significant saving we can realize by making use of the existing technology of helium gas cooling, which is a relatively matured power plant technology.

6.3.2.4. Divertor and in-vessel component options

As an engineering system, the in-vessel components, including the divertor design requirements are: (1) to handle the high average and maximum surface heat flux while optimizing the coolant outlet temperature and minimizing the pumping power, (2) to use a surface material which minimizes the sputtering erosion and maximizes the component life-time, (3) to use a sound and simple mechanical design to provide high reliability and allow ease of maintenance, (4) to withstand a few disruptions, and (5) to have a vacuum pumping system to match the requirements of ash removal and density control of the divertor and impurity control of the plasma-core and divertor channels/plates. In the following, we evaluate the feasibility of using V-alloy to remove the maximum heat flux of 5 MW/m^2 for both lithium and helium coolants and review the status of using V-alloy as the plasma facing material.

Thermal-hydraulic evaluation. As a scoping feasibility study, only a simple 2-m long tube with 2-mm coating of W was used for this evaluation. The cooling tube was used to remove the impinging average surface heat flux of 1 MW/m^2 and maximum surface heat flux of 5 MW/m^2. Only surface heat fluxes impinging onto the divertor surfaces were considered (the contribution of the volumetric power generation would be less than 10% of the surface heat flux). The maximum V-alloy design temperature limit of 700 °C and the primary and primary plus secondary stress limits of $S_{mt} = 105$ MPa and $3S_{mt} = 315$ MPa, respectively, at fluence of 200 dpa, were used as our design guidelines [1].

Adjustable parameters are the tube diameter, wall thickness, and the coolant inlet and outlet temperatures. The coolant flow rate was defined by the selected coolant inlet and outlet temperatures and the average power intercepted by the projected surface area of each coolant tube. With the knowledge of coolant volume flow rate and tube inside diameter, the coolant velocity, heat transfer coefficients, tube wall, and sacrificial wall temperature gradients were calculated. The maximum tube temperature was then

determined as the sum of the bulk coolant temperature, the film drop temperature, and solid material temperature gradients. These calculations were applied to both coolant options.

The first option is the lithium-cooled design. The lithium coolant operates in a magnetic field strength of 7 T, with a tube diameter of 1 cm. The Hartmann number of the design is 4,702, which is well into the laminar regime indicated by Gardner [34]. Therefore a Nusselt number of $Nu = 7$ was used for the calculation. This value of Nu was determined from laminar pipe flow in a transverse magnetic field with uniform wall heat flux; therefore, to compensate for the one-sided heat transfer, a flow diversion design such as helical fins may need to be incorporated in the future design. This local flow distribution will only be needed at the location of maximum heat flux. Here we also assumed that the necessary MHD insulation inside all the coolant channels will function properly and will not impact either the heat transfer or the pressure drop of the design.

The second option is the helium-cooled design. In order to enhance heat transfer, surface roughening was assumed. This allows an improvement of heat transfer by a factor of two with the corresponding friction factor increased by a factor of 3 [35]. Similar to the lithium design, a twisted tape also can be used to reduce the effect from one-sided heat flux [36]. Again only local heat transfer enhancement will be needed at the location of the maximum surface heat flux.

Table 6.3-IV shows the scoping design results of the lithium and helium-cooled design options. These results show that, to meet the thermal stress limit, the V-alloy tube wall will have to be relatively thin. Correspondingly, relatively small diameter tubes will be necessary to generate high enough heat removal capacity to meet the material temperature limit. Tubes with inside diameters of 1 and 0.6 cm can be used for the lithium and helium coolant options, respectively. The coolant outlet temperatures also will have to be lower than the corresponding blanket outlet temperatures to meet the maximum temperature limit of 700 °C for the V-alloy. Relatively, the helium-cooled tubes will have to be smaller and will require higher pumping power than the lithium-cooled design.

Sputtering erosion and plasma facing material selection. Material erosion is an important consideration of in-vessel and divertor component design and affects the lifetime of the components. Unfortunately, for the V-alloy design, there is no relevant erosion data. It is also possible that V-alloy structure must be coated with another material such as C, Be, and W. Carbon has been used as the first wall material for all existing large

tokamaks, like JET, JT-60, TFTR, and DIII-D. Beryllium has been used in JET. Carbon, Be, and W are the reference plasma facing materials as reported in the fourth report for the Technical Advisory Committee (TAC) of the ITER-EDA design [37]. Comparing the materials of interest, a potential sputtering rate can be listed in the order of Be, C, V-alloy and W, where Be will have the highest erosion rate and W the lowest [38]. Highly preliminary results based on present physics and modeling assumptions indicate 2 to 3 orders of magnitude difference between Be (at tenths of a meter per full power year) and

Table 6.3-IV.
Scoping Thermal-hydraulics of V-Alloy Divertors

Coolant	Lithium	18 MPa He
Inlet temperature (°C)	300	250
Outlet temperature (°C)	450	400
Gross thermal efficiency	$\sim 39\%$	$\sim 39\%$
Tube diameter (cm)	1	0.6
Tube-wall thickness (mm)	1	1
Coolant velocity (m/s)	1.3	78
Heat-transfer coefficient, h (W/m^2°C)	3.3×10^4 $^{(a)}$	2.5×10^4 $^{(b)}$
Tube-wall maximum temperature (°C)	694	690
W-coating maximum temperature (°C)	793	790
Pumping power fraction	0.01	0.09$^{(c)}$
Primary stress (MPa)	13	54
Thermal stress (MPa)	157	157
Total stress (MPa)	170	211

(a) A Nusselt number value of 7 was used.

(b) With local heat transfer enhancement of 2.

(c) With increased friction factor of 3.

W in net erosion [39]. Due to its chemical reactivity with hydrogen, C is potentially the worst when chemical sputtering at high surface temperature is considered. Under high fusion neutron fluence, both Be and C have the additional disadvantage of significant loss in thermal conductivity and structural strength. Therefore both Be and C are projected to be unsuitable as structural and coating material for the Demo design. For V-alloy, experimental measurements from a metal-coated sample exposed to the DIII-D plasma indicated that the erosion of V can be at least an order of magnitude lower than C, possibly not as low as W [40]. While W exhibits the best properties against erosion, contamination of plasma with W as well as induced radioactivity in W are areas of concern.

6.3.2.5. Use of vanadium in the shield

Vanadium possesses salient features that are of great importance for fusion plants. Among these features are the high operating temperature capability ($\sim$ 700 °C), low afterheat generation, and low activation characteristics. However, V is a more expensive and less efficient shielding material compared to steels. Recent studies have indicated that, in order to improve the economics of V-based fusion plants, it is essential to limit the use of V to components where these features are most needed, *i.e.*, in the plasma facing components, blanket, reflector, and inner layer of the shield. Furthermore, less expensive, low activation materials (such as ferritic steels) could be used in the outer layer of the shield and the vacuum vessel where radiation flux and operating temperature are much reduced.

The economic analysis of the ARIES-II design, which employs V structure for the entire shield, has indicated that the shield is the most expensive component in the machine. The shield is well optimized for high neutronics performance and contains 15% V structure, by volume. Nevertheless, V comprises more than half of the shield cost. This has prompted the need to replace the V structure in the outer layer of the shield with less expensive steel structure in order to reduce the cost of future V-based designs. This change should not impact the safety characteristics of the design as the outer layer of the shield is subjected to low radiation flux, generating low levels of radioactivity and afterheat. The saving in the shield cost will be significant ($\sim$ 40%). This will come at some cost in the power balance since steel cannot operate at temperatures as high as V. The outer layer of the shield and the vacuum vessel will thus operate at lower temperature (<550 °C) and the small amount of nuclear heating deposited therein will not be recovered in the power cycle. The dividing boundary between the two layers of the shield

will therefore depend on how much power could be dumped as low grade heat with minor effect on the power balance (*e.g.,* 1%–5%).

To conclude, it may not be economical to use V structure in the entire shield. The inner layer of the shield, along with the first wall, blanket, and reflector, should employ V structure whereas the lower temperature outer layer of the shield and vacuum vessel should utilize stainless steel as the main structural material. This approach for designing the shield of V-based fusion power plants, along with other innovative ideas to improve the shield performance, will have significant impact on the cost of the shield and overall machine.

6.3.2.6. Use of vanadium in the heat transport loop

For use in the blanket, the cost of the vanadium can be offset by the performance of the material. For the heat transport loop design, the use of V-alloy has to be minimized to reduce the capital cost of the power plant. Stabilized ferritic steel is a possible material to be used for the primary loop. However, corrosion of ferritic steel with Li at the coolant temperature of ARIES designs can be severe. Also, mass transfer between the steel loop and the vanadium blanket may cause bi-metallic loop material problems.

The design proposed here uses double-walled tubing for the primary loop. A thick steel layer will be placed on the outside of the tube for support. A vanadium liner, about 1 mm thick, can be the inside layer facing the lithium. The intermediate heat exchanger (IHX) design also can be a double-walled design, which is similar to the ones developed for the breeder program [41]. A sketch of the proposed IHX is shown on Fig. 6.3-8. The primary coolant, lithium, will be on the tube side, which will be connected to the outer tube sheet. The outer tube of the IHX can be made of stainless steel and will face the secondary coolant, sodium. The outer tube will be connected to the inner tube sheet. The joint between vanadium and the steel can be made in the middle of the outer tube sheet. Thus, the primary coolant, lithium, will never contact the steel, while the secondary coolant, sodium, will never contact the vanadium. The potential problems associated with bi-metallic loop can thus be avoided. To fabricate this double-wall design, the vanadium will need to be welded to steel. This has been demonstrated on a small scale.

The total volume of vanadium being used in the blanket and shield is 80 m^3, while the volume used in the primary loop is estimated to be $\sim$ 13 m^3($\sim$ 0.6 m^3 for the main coolant pipes, $\sim$ 10 m^3 for the IHX tubes and $\sim$ 2 m^3 for the IHX tube sheets, see

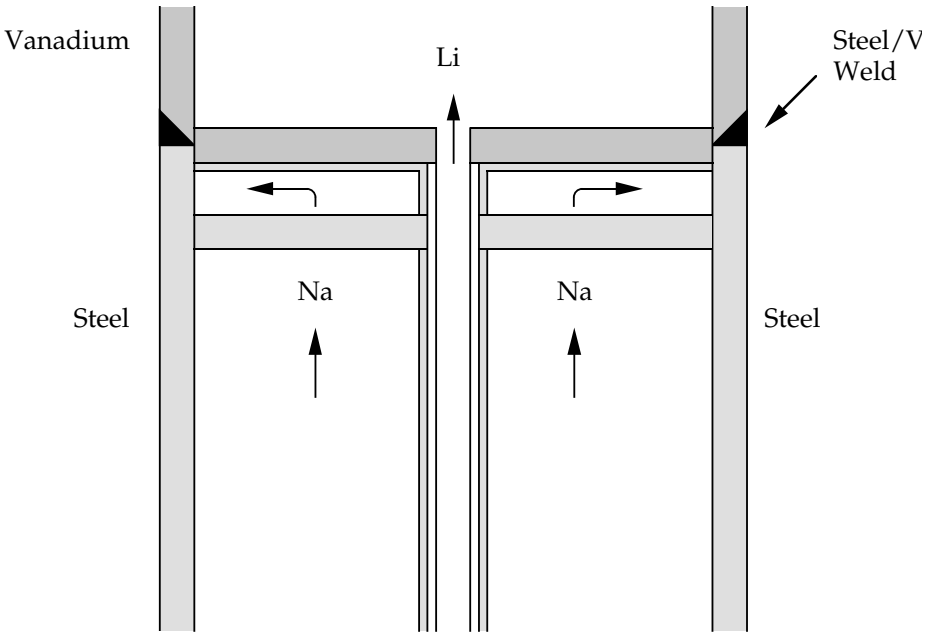

Figure 6.3-8. A proposed IHX design for self-cooled Li/W designs.

Fig. 6.3-8). Assuming a unit cost of $300/kg, the additional cost of vanadium used in the heat transport loop is 24 M$.

6.3.3. Material Properties

Several of the properties which are most important in determining the attractiveness of vanadium alloys as fusion in-vessel materials are discussed in this section. These include tensile and creep properties, irradiation effects (swelling, creep-enhancement, and hardening or softening), compatibility with gaseous and Li environments, and fabrication concerns.

A more comprehensive collection of properties is included as an appendix to this report. These cover a wider range of properties that are needed to complete the design phase of this effort.

The U.S. Fusion Materials Program has identified V-4wt.%Cr-4wt.%Ti (V-4Cr-4Ti) with 0.01 to 0.1 wt.% Si as a promising structural material for fusion reactor applications. Recent progress made on this material is summarized in the U.S. Contribution 1994 Summary Report on Task T12 [42] from which most of the following material is taken. One laboratory heat (30 kg) and one industrial-size heat (500 kg) of this alloy have been

produced for laboratory-scale and in-reactor testing. In addition to alloying elements (V, Cr, Ti, Si) and impurities (H, O, C, N, *etc.*), heat treatment plays a very important role in the performance of V-alloys.

The data base for binary (V-Ti, V-Cr) and ternary (V-Cr-Ti) alloys is much more extensive than the data base for V-4Cr-4Ti alone. This extensive data base has been used to select the current reference alloy and, for some properties (*e.g.,* thermophysical, elastic, *etc.*), it can be used directly for the reference properties. However, because heat treatment and impurities can be as important as the base alloying elements, it has sometimes been difficult to isolate the effects of each alloying element. For example, the excellent ductility of the V-4Cr-4Ti alloy as compared to a particular heat of V-5Cr-5Ti led some researchers to speculate that the properties are extremely sensitive to the sum of Ti and Cr content. Subsequent work in which the same purity of raw materials and the same heat treatment used to produce the V-4Cr-4Ti alloy was used to produce the V-5Cr-5Ti alloy resulted in similar properties for the two alloys. Also, the "optimization" which has led to the selection of V-4Cr-4Ti has been performed from a materials perspective, rather than from a design perspective. Therefore, as more experience is gained with alloys in this class and as more interaction takes place among the design engineers and the material scientists, chemistry and heat-treatment modifications will be made to the reference alloy to optimize V-Cr-Ti for design application

The V-4Cr-4Ti alloy, along with a specific heat treatment, has been chosen as the reference alloy based on an optimization with regard to tensile and impact ductility. The addition of Si, along with limiting the interstitial oxygen, carbon and nitrogen impurities to $\leq 1,000$ wppm, is important for swelling resistance. While not necessarily optimized in the reference composition, alloys with ≥ 3 wt.% Ti and about 0.5 wt.% Si promote swelling resistance through the formation of finely dispersed Ti_5Si_3 precipitates. With regard to mechanical properties, the tensile strength tends to increase with increases in Ti and Cr content, as well as Si content. However, the ductile-to-brittle transition temperature (DBTT) also increases with these additions. From a DBTT standpoint, it appears to be desirable to keep the sum of the Ti and Cr concentrations to ≤ 10 wt.%. Similarly, small increases in Si have a positive effect on strength, but tend to raise the DBTT. Historically, the emphasis on tensile and impact ductility comes from the experience with ferritic steels which have problems in these areas due to irradiation-induced hardening at the lower temperatures ($\leq 400\,^{\circ}$C). However, there is room for improvement by optimizing both the chemistry and heat treatment from the perspective of design performance. For example, optimizing the alloy composition based on maintaining a DBTT of $\sim 200\,^{\circ}$C at the expense of some other property (*e.g.,* tensile strength, creep strength,

swelling resistance) makes little sense from a design perspective, which at most requires a DBTT below room temperature. Optimizing the alloy composition to attain the highest uniform elongation may make little design sense because all that is required of this parameter is it be $\geq 5\%$ to qualify as a ductile material. Optimizing the alloy composition to improve the yield strength would be of no direct benefit, because the ultimate tensile strength (S_u) of V-4Cr-4Ti determines the allowable primary membrane stress ($S_m = S_u/3$) and the combined membrane plus bending plus thermal stress (S_u).

6.3.3.1. Thermophysical and elastic properties

The density, heat capacity, thermal conductivity, Young's modulus and shear modulus of pure vanadium are all well characterized as functions of temperature. Alloying elements Ti and Cr in the combined range of ≤ 10 wt.% have no significant effect on these properties. Similarly, non-metallic impurities in the reference range of $\leq 1,000$ wppm have no effect. Neutron damage to the bulk material should also have no significant effect. As compared to austenitic and ferritic steels, the V-4Cr-4Ti alloy is lighter (6.07 g/cm^3 at room temperature), higher in thermal conductivity, and lower in thermal expansion. When coupled with its higher yield and ultimate strength at high temperature, V-4Cr-4Ti is a better high heat-flux material than either of the steels.

6.3.3.2. Tensile and creep properties of unirradiated V-4Cr-4Ti

The ultimate tensile strength (S_u), tensile yield strength (S_y), uniform elongation (e_u) and total elongation (e_t) of V-4Cr-4Ti are reasonably well characterized from room temperature to 700 °C. More data on the industrial heat are forthcoming to add some statistical significance to the overall data base. Data are also being generated on the reduction in area (RA) at the failed neck region, which is a better measure of local failure strain than e_t. The secondary thermal creep rate and time-to-rupture of V-4Cr-4Ti are characterized at 600 °C for high stresses (380–420 MPa). Higher temperature and lower stress data are needed.

Based on the tensile and creep properties, V-4Cr-4Ti is a better high-temperature structural material than either austenitic stainless steel (*e.g.,* 316L(N)) or ferritic steel (*e.g.,* Fe-9Cr-1MoVb). Its ultimate tensile and yield strengths are relatively constant for temperatures in the range of room temperature to 700 °C. In this section, the properties of V-4Cr-4Ti are compared to those of 316L(N) and Fe-9Cr-1MoVNb in terms of two parameters which are of particular interest to the design of first-wall and high heat flux

components. The first parameter is the maximum allowable primary membrane stress (S_m). In general, S_m is defined as the minimum of 2 $S_{yd}/3$ and $S_{ud}/3$. For austenitic stainless steels, values of S_m as high as $0.9S_{yd}$ are allowed under certain circumstances (*e.g.,* $T \geq 160\,^{\circ}$C). The parameters S_{yd} and S_{ud} are "design" values for the yield and ultimate tensile strengths, respectively. The design properties are determined from the data base by bounding from below the room temperature strengths and then following the temperature dependence determined from the average of the data. In a statistical sense, the properties are neither "average" nor "lower-bound" properties over the temperature ranges of interest. However, they are consistent with what is required by design codes for determining maximum allowable stresses. For both 316L(N) and Fe-9Cr-1MoVNb, the values are taken from the French RCC-MR design code [43,44]. In the case of V-4Cr-4Ti, which is not as yet code-qualified and for which there is only a limited data base, the scaling factors for 316L(N) are used: $S_{yd} = S_y(avg.)/1.25$ and $S_{ud} = S_u(avg)/1.15$.

The results of the S_m comparison are shown in Fig. 6.3-9. Above 350 °C, V-4Cr-4Ti is a stronger material than 316L(N) against primary loads (*e.g.,* coolant pressure). Above 525 °C, V-4Cr-4Ti is stronger than Fe-9Cr-1MoVNb. These results do no take into account the long term effects of creep and fatigue.

The second parameter of interest in the design of first-wall and high-heat-flux components is the thermal stress factor (TSF). The sum of primary pressure and bending loads, along with secondary stresses such as thermal stresses, is limited to $3S_m$, which for Fe-9Cr-1MoVNb and V-4Cr-4Ti is equal to S_{ud}. The thermal stress (or maximum heat flux) factor is a measure of the maximum surface heat flux (in MW/m^2) allowed for a 1-mm-thick wall. It is calculated from the following formula which is based on the maximum allowable stress ($3S_m$) divided by an estimate of the thermal stress:

$$\text{TSF} \;=\; \frac{3S_m}{(\alpha_m E)/[k(1-\nu))]}\,, \tag{6.3-1}$$

where α_m is the mean coefficient of linear thermal expansion (in $10^6/\,^{\circ}$C), E is the Young's modulus (in GPa), k is the thermal conductivity (in W/m-°C) and ν is Poisson's ratio. The results are shown in Fig. 6.3-10 for the three materials of interest. These results can be interpreted in the following manner. At 650 °C, the thermal stress factor for both 316L(N) and Fe-9Cr-1MoVNb is about 1.8, while for V-4Cr-4Ti the factor is about 6.0. For a 5-mm first wall thickness at 650 °C, V-4Cr-4Ti can accommodate a surface heat flux as high as 1.2 MW/m^2, while the other two materials can only accommodate a surface heat flux of 0.36 MW/m^2. The results for both V-4Cr-4Ti and 316L(N) are relatively insensitive to temperature, while Fe-9Cr-1MoVNb performs much better at

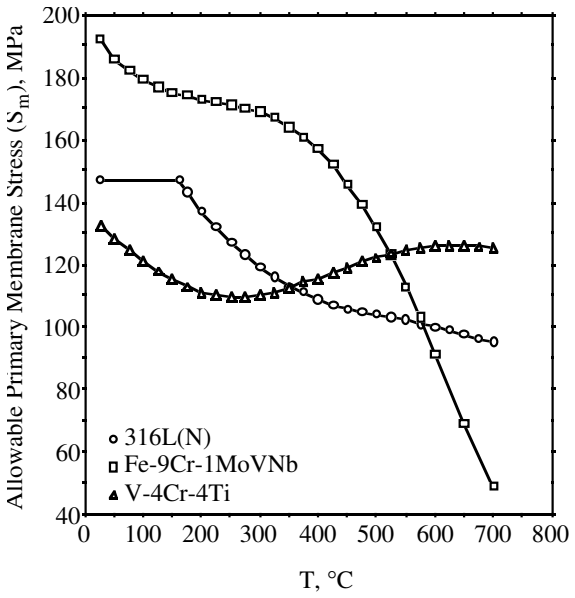

Figure 6.3-9. Comparison of the allowable primary membrane stress (S_m) for unirradiated 316L(N) stainless steel (based on RCC-MR code), ferritic/martensitic Fe-9Cr-1MoVNb (based on RCC-MR code) and V-4Cr-4Ti (based on 1/3 of the minimum ultimate tensile strength, which is taken as the average/1.15).

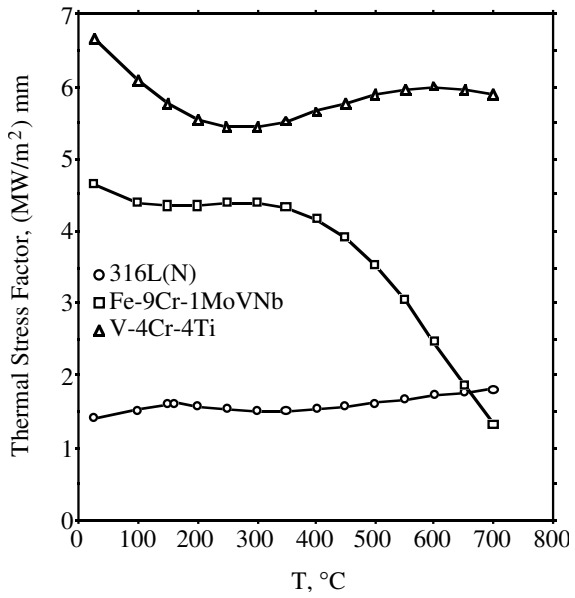

Figure 6.3-10. Comparison of the thermal stress factor for 316L(N), Fe-9Cr-1MoVNb, and V-4Cr-4Ti.

lower temperatures. These calculations assume no primary loads on the structure. A more detailed calculation would start with an assumed local coolant temperature and use iteration until a consistent set of temperature-dependent material properties and limiting heat flux were achieved for a given wall thickness.

In the previous comparisons among V-4Cr-4Ti, 316L(N) and Fe-9Cr-1MoVNb, the S_m limit to primary membrane stresses and the $3S_m$ limit to combined primary membrane, primary bending and thermal stresses were used. These limiting parameters ensure reasonable design margins excluding the possible time-dependent effects of creep and fatigue. Creep is incorporated into the analysis by making S_m time-dependent (S_{mt}) based on a limiting creep strain or time-to-rupture and a desired lifetime. Thus, the higher the creep-resistance of the structural material, the higher the S_{mt} values. While creep data for V-Cr-Ti ternary alloys are available, the thermal creep data base for V-4Cr-4Ti is limited a few high-stress data points at 600 °C. Thus, the secondary thermal creep rates of the three structural materials are compared in Fig. 6.3-11 at 600 °C. The V-4Cr-4Ti ally is clearly the most creep-resistant at 600 °C. In terms of the reduction in S_m with time (S_{mt}) over a two-year period, thermal creep tends to cause a reduction for Fe-9Cr-1MoVNb above 450 °C, for 316L(N) above 550 °C, and for V-4Cr-4Ti above

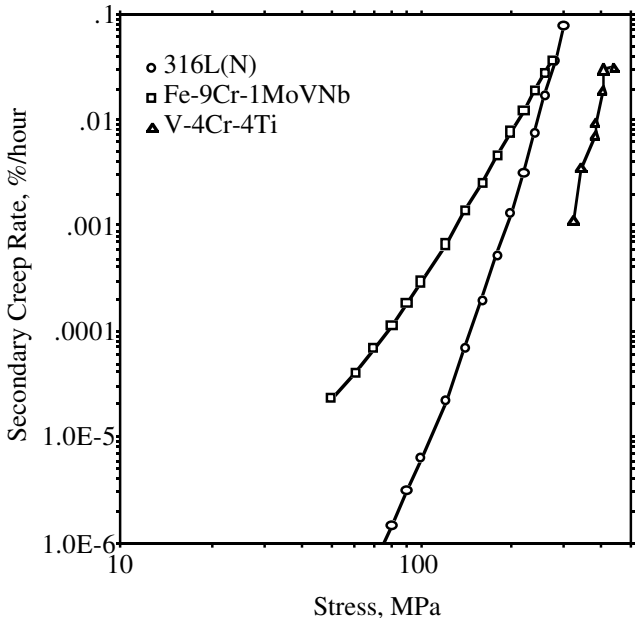

Figure 6.3-11. Secondary thermal creep rates of 316L(N), Fe-9Cr-1MoVNb, and V-4Cr-4Ti at 600 °C. The correlation plotted for Fe-9Cr-1MoVNb is actually for HT-9 (Fe-12Cr-1MoVW) which should represent an upper bound to Fe-9Cr-1MoVNb.

650 °C. For a four-year time period corresponding to a lifetime of 200 dpa, it does not appear likely that thermal creep will cause a reduction in S_m ($\sim$ 125 MPa) for temperatures $\leq$ 650 °C. Clearly, more thermal creep data for the reference alloy are needed to resolve this issue.

6.3.3.3. Irradiation effects

Irradiation effects of importance to structural materials in a fusion environment include swelling, creep-enhancement, hardening (or softening) and embrittlement. Swelling data on V-alloys have been obtained for temperatures in the range of 420 to 600 °C up to 114 dpa. Unlike the behavior of 316L(N) and Fe-9Cr-1MoVNb, V-alloy swelling tends to peak in the neutron damage range of 30–80 dpa and then to decrease. The peak volumetric swelling measured for V-15Cr-5Ti is in the range of 2%–3% at 114 dpa. Generally, a 5% design limit is placed on volumetric swelling. However, deformation limits which do not lead to failure of a component in isolation are very design dependent. In the spirit of this generalization, swelling of V-alloys should not limit the lifetime of components for the dpa range of the data base ($\leq$ 114 dpa). While there is no analytical or experimental evidence to suggest that volumetric swelling would limit operation to higher damage levels (*e.g.,* 200 dpa), this needs to be demonstrated for the reference alloy for He/dpa ratios of $\leq$ 6.5.

The swelling of the reference V-alloy (V-4Cr-4Ti) has been investigated in the temperature range of 425–600 °C up to 31 dpa with He/dpa values ranging from $\ll 1 - 4.2$. The peak swelling observed is 1.8 vol.% at 425 °C, 31 dpa and 1 appm He. Assuming that this alloy continues to perform the same as the other V-alloys tested, then peak swelling values in the temperature range of 400–600 °C should remain below 5 vol.% beyond 100 dpa.

Irradiation-enhanced creep has been studied for austenitic and ferritic steels, but not for V-alloys. Unlike thermally-induced creep, this deformation mechanism is considered to be "non-damaging" in the sense that there is no ductility limit associated with, or correlated with, failure. In a sense, it is similar to swelling in that large amounts of strain could cause geometric problems and differential strains across the component could result in significant secondary stresses. It is commonly assumed that the irradiation creep rate of V-alloys will be similar to that of austenitic and ferritic steels. Because of the complication of swelling in the austenitic steel data base, the irradiation creep correlation for low-swelling ferritic steel is usually used to represent the behavior of V-alloys. An

approximation for the creep strain for both 12Cr and 9Cr ferritic steel is [45]:

$$\epsilon_{ic} \;=\; 2.2 \times 10^2 \, D \, \sigma \, , \tag{6.3-2}$$

where ϵ_{ic} is the irradiation creep, D is neutron damage in dpa and σ is effective stress in MPa.

For V-4Cr-4Ti, $S_m = 125$ MPa for 500–700 °C. Using a 5% limit for irradiation creep means that at 125 MPa the 5% limit would be reached at 180 dpa. In order to achieve a lifetime of 200 dpa at $\leq 5\%$ irradiation creep strain, S_m would have to be reduced by 10% to 113 MPa. However, in future work, the irradiation-induced creep rate of V-4Cr-4Ti needs to be determined directly and, once a specific design has been established, an irradiation creep strain limit needs to be established based on the design details.

Thus far in the analysis, it appears that neither swelling nor irradiation creep of V-4Cr-4Ti would limit operation of V-4Cr-4Ti to < 100 dpa. Operation to damage levels up to 200 dpa may be achievable, but data are required to substantiate safe, reliable performance up to such high damage levels.

The next issues addressed are hardening and embrittlement. Within the irradiation data base available for V-4Cr-4Ti (400–600 °C, 0–31 dpa, and 0–75 appm He), the changes in tensile properties are as follows: UTS increases by 79% (400–430 °C), 35% (500–520 °C) and 8% (600 °C); YS increases by 162% (400–430 °C), 112% (500–520 °C), and 45% (600 °C); UE decreases to $1.6\% \pm 1.0\%$ (400–430 °C), $3.6\% \pm 1.3\%$ (500–520 °C) and $6.5\% \pm 1.1\%$ (600 °C). For all of these cases, the DBTT remains $\ll 0$ °C. The increase in strength should cause no problems in the design. However, the designer should not use this irradiation-strengthening to increase the allowable stresses. Overpower and undercooling events which tend to elevate the structure temperature for brief periods of time may anneal out this hardening. Also, with some materials [*e.g.,* 316L(N)] cycling has been observed to soften the irradiated material.

The decrease in uniform elongation with irradiation is significant for samples irradiated and tested at 400–430 °C. Such low uniform elongation values require the use of special design rules such as those developed for ferritic and austenitic steels which tend to embrittle to even lower UE values at 200–400 °C. They also suggest that more irradiation testing be performed to map out the temperature range, neutron damage level and He concentration at which embrittlement may become a serious design issue. In the interim, it is recommended that T ¿ 430 °C be used as a lower limit temperature for V-4Cr-4Ti alloys.

In conclusion, no irradiation effects have been observed which would limit operation of V-4Cr-4Ti to < 100 dpa as long as the component is designed in accordance with

rules for unirradiated material and the minimum operating temperature is set at 430 °C. Operation to 200 dpa may require a 10% reduction in the allowable primary membrane stress. However, the data base for V-4Cr-4Ti needs to be expanded to higher neutron damage levels, higher helium levels and lower temperatures to support these conclusions. Also, fatigue data should be generated to allow a fatigue design analysis to be performed. The final issues which need to be addressed are compatibility with the coolant and/or coating and the behavior of hydrogen isotopes which may be implanted in, generated by transmutation in, or transported to, the V-4Cr-4Ti structural material.

6.3.3.4. Compatibility issues

Compatibility of V-alloys with gaseous environments is important during fabrication, handling and maintenance, as well as operation if gas (*e.g.*, He) is used as a coolant. Compatibility with liquid Li is also important. The V-alloy/Li case is complicated by the presence of an electrically insulating layer (*e.g.,* AlN or CaO) which is required for MHD pressure drop reduction. The behavior of implanted, permeated or transmuted hydrogen isotopes must also be addressed.

The specifications for the reference V-4Cr-4Ti material call for < 30 appm H and $< 1,000$ wppm of O, C, and N. Significant increases in these non-metallic impurities can cause undesirable decreases in the tensile ductility and the impact DBTT. The main problem is caused by high interstitial levels of these impurities. The solubility limits for O, N, and C impurities in V-alloys at 500 °C are 1.1×10^4 wppm for O, 3.9×10^3 wppm for N and 400 wppm for C. Hydrogen should be treated separately from these other impurities. At 1 Pa of H_2 pressure, the solubility of H in V-alloys is about 400 appm (about 8 wppm). For a gas-cooled system (*e.g.,* He) impurity control, particularly for O_2 and H_2O has to be exceedingly tight in order to prevent embrittling oxidation. For a V-alloy/Li system, the problem is much less severe because Li has a higher chemical affinity for H and O than does V. For example, in the temperature range of 280–550 °C, the ratio of H in the Li to H in the V-alloy is about 1000/1 if the system achieves thermodynamic equilibrium. Under these same conditions, the ratio of O in the Li to O in the V-alloy is greater than 10 million to one. Thus, impurity control for the V-alloy/Li system centers around controlling the N and C levels in the coolant. In particular, N levels should be limited to < 20 wppm and C levels should be limited to about 6×10^{-8} wppm in Li. There is no conceptual or practical problem in doing so. These limits would maintain the N level in the V-alloy to below 1800 wppm and would keep the C level to below

200 wppm in the V-alloy. The role which the MHD coating plays in the impurity control and distribution of impurities needs to be addressed in future R&D work.

Impurity levels in the Li coolant can lead to enhanced corrosion of V-alloys, as well as to direct embrittlement of the V-alloy through transport of the impurities to the V-alloy. In general, if the impurity levels are controlled such that C and N transfer to the V-alloy is within design limits, the corrosion rates are very low. For a bare V-alloy/Li interface, the corrosion rate is only about 1 mm/year at 700 °C. Thus, protecting the V-alloy from embrittlement eliminates corrosion as a concern.

Excessive tritium build-up in the V-alloy is of concern from both safety and embrittlement perspectives. These problems have been addressed in past design studies. However, there is a high degree of uncertainty associated with modeling the behavior of tritium implanted or transmuted in coated V-alloys. Thermodynamically, the Li coolant has a much higher affinity for the hydrogen isotopes than does V. The central issue for coated V-alloys becomes the degree to which the electrical insulator coating acts as a barrier to hydrogen-isotope transport. More work, both analytical and experimental, needs to be performed in this area.

While most of the past R&D has focused on V-alloy/Li compatibility, future efforts need to be directed at the compatibility of the electrical-insulator coating with Li, the compatibility of the coating with the V-alloy and the compatibility of the overall system.

6.3.3.5. Fabrication

Vanadium alloys have been fabricated into a variety of shapes and sizes, including plate, sheet, tubing and wire. The major issue is to avoid environmental contamination during processing. Oxygen is a particular problem as V-alloys react rapidly with oxygen at elevated temperatures [46]. Within the fusion R&D program, most fabrication has been limited to producing small test samples. Recently, a 3-m-long tube (48-mm ID and 60-mm OD) of V-4Cr-4Ti has been fabricated with a CaO coating for the purpose of testing in a magnetic field with flowing Li. Also, V-4Cr-4Ti has been selected as a structural component for the DIII-D Radiative Divertor. This project will provide valuable experience with a larger size heat ($\sim 1,000$ kg), fabrication of different product forms, welding of similar and dissimilar materials, and non-destructive testing techniques.

Within the U.S. fusion R&D program, the welding of V-alloys has received a great deal of attention. In particular, gas tungsten arc (GTA) or tungsten inert gas (TIG), electron beam and laser welding techniques have been applied and characterized. The

GTA method presents particular problems in that a high purity atmosphere is required. Electron beam welding has produced some excellent results without the need for post-weld heat treatment (PWHT). Laser welding has produced some good results as well. The need for PWHT has not yet been established. Experience with a particular lot of V-5Cr-5Ti (BL-63) proved inconclusive in that both the base metal and the GTA-welded section improved in ductility with a PWHT at 950 °C.

In summary, it is recognized that experience with vanadium-alloy fabrication and joining is limited. This is being addressed within the R&D program.

6.3.4. Ability to Meet Demo Requirements

Several of the Demo requirements may act as discriminators between the different engineering design options. Three of them are highlighted here as they relate to the use of vanadium alloy in a power plant. These are:

1. Cost and Performance Requirements. Attractive features of vanadium include its higher temperature limit and improved thermophysical properties, which allow operation at higher plant efficiency and higher power density. However, the high material costs may offset these advantages. Analysis shows that a vanadium system which uses the alloy only where needed, and which adopts a recycling strategy, can be economically competitive.

2. Safety, Licensing and Environmental Requirements. Vanadium alloys have the potential for superior safety and environmental characteristics. Accident safety and waste management are examined to determine whether the aggressive Demo requirements can be met.

3. Reliability and Availability Requirements. There is no data on the reliability of fusion components in the fusion environment. However, analogous data from other technologies suggest that achieving the availability goal will require either significantly reduced failure rates and/or some form of in situ repair mechanism or system redundancy.

6.3.4.1. Cost and performance requirements

One of the top level requirements for the U.S. Demo power plant states that the cost of electricity must be competitive. In 1995 dollars, the goal is 80 mill/kWeh and the

requirement is 90 mill/kWeh. Sub-tier requirements are then derived from this requirement and goal. In the evaluation of advanced structural materials, attention has been given to two key sub-tier requirements: (1) the total capital cost should be less than \$5B, and (2) the gross thermal efficiency should be higher than 46%. These requirements have been evaluated for both the V/Li and He/Li/V blanket options.

The V-alloy Li self-cooled design was adapted from the ARIES-II design, modified to reduce the use of vanadium, and examined using the ARIES System Code. For this case, the first wall/blanket cost was \$69M and the shield cost was \$239M. Together, the first wall, blanket, and shield cost is approximately 15% of the total direct cost of the power plant. This figure is based on the unit cost of the V-alloy structure at \$300/kg, ferritic steel structure (HT-9) at \$68/kg, and tenelon filler at \$25/kg in constant 1992 dollars. The cost of the vanadium in the shield has been reduced substantially as compared with earlier designs by using steel filler and mechanical support structure wherever possible. (See Sec. 6.2.4.3)

Vanadium alloy is a new structural alloy. To date, there have not been major industrial applications to support its development. The three basic costing elements for structural material (cost for production of different product forms, cost for fabrication, and cost for installation) are still to be developed for V-alloy. Therefore, there is no statistical information available to project a reliable unit cost for first wall, blanket, and shield components. Only a rough estimate on the lower and upper bounds of the unit cost can be made.

Based on the application of advanced structural materials for fusion devices [47], it is observed that the product form cost will amount to about 30% of the unit cost of the final component, including labor. Taking the 1995 cost of advanced Ni-based structural materials as a starting point, the product form cost is about \$100/kg. If this is assumed to be the same for V-alloy, then the lower bound of V-alloy unit cost can be assumed to be about \$300/kg. At the other end of the spectrum, based on the recently placed DIII-D contract for the V-4Cr-4Ti alloy material necessary for the upper divertor in the Radiative Divertor Program (RDP), the finished V-alloy component cost is about \$600/kg [47]. For Demo, this unit cost can be lowered because of increased experience beyond the year 2020. But when compared to the DIII-D RDP component, which is a relatively simple water-cooled design, the unit cost may become higher because of the Demo design complexity. Considering this trade-off, it may be reasonable to assume that the upper bound for the Demo V-alloy unit cost is about \$600/kg.

6.3.4.2. Safety, licensing and environmental requirements

Vanadium alloys have the potential for superior safety and environmental characteristics when compared with other near-term structural materials. A safety evaluation of any structural material must include the impact of routine emissions, dose rates in working areas, decay heat, potential off-site doses from hypothetical accidents, and the management of end-of service material. The two safety aspects of primary importance in assessing a material for use in the DEMO reactor are the consequences of accidents and the options for waste management.

Consequences of accidental releases. Potential doses from an accidental release of activated material depend on the radioactive inventory, the volatility of the compounds containing the radionuclides, and available means of transport for the radionuclides to the facility boundary. The isotopes governing early off-site doses are ^{48}Sc, ^{42}Ar, ^{24}Na, ^{46}Sc, ^{45}Ca and ^{51}Cr. The potential for mobilization of specific elements from fusion-relevant materials in high-temperature excursions under oxidizing conditions has been investigated in experiments at INEL [48]. In the vanadium alloy volatility tests, vanadium alloys were doped with scandium, calcium and manganese to simulate the activation products. Based on the release rates observed in these experiments, elemental mobilization fractions for the alloys V-15Cr-5Ti and V-3Ti-1Si corresponding to a material thickness of 5 mm and duration of 1 h at elevated temperature were calculated.

In estimating the potential off-site radiation dose, the following pessimistic conditions are assumed: (1) 2-km site boundary radius; (2) 1 m/s wind velocity; (3) Pasquill F stability conditions; (4) near-ground-level release (0–10 m); (5) no release delay; (6) 1 h release duration; (7) 200 m height of mixing layer; (8) no rain; (9) rough (urban or forest terrain roughness index); and (10) building wake effects for a 40 × 40 m building.

Based on these conditions, the early doses to an individual at 2 km for designs employing V-15Cr-5Ti and V-3Ti-1Si were about a factor 30 below those for 316L stainless steel for a range of first wall temperatures from 900 K to 1,500 K. With the V-15Cr-5Ti alloy, ^{42}Ar dominates the dose at the lower temperatures while ^{48}Sc dominates at higher temperatures. It is assumed that all the argon is released over the 7-day duration of the accident. Other isotopes contributing more than 5% to the early dose are ^{46}Sc, ^{45}Ca, and ^{51}Cr.

With the V-3Ti-1Si alloy, off-site doses are governed by ^{24}Na at lower temperatures and ^{48}Sc at higher temperatures. A conservative value of 0.3, based on the properties of

sodium at typical accident temperatures, was used in the absence of experimental data on the mobilization fraction for sodium. Additional isotopes contributing more that 5% to the early dose are ^{46}Sc, ^{45}Ca, and ^{42}Ar.

Options for Waste Management – The waste management options for vanadium components are either recycling or direct disposal. Over the period relevant to waste disposal, the radioactive inventory of the vanadium alloys is dominated by the argon isotopes ^{39}Ar ($T_{1/2}$ = 269 y) and ^{42}Ar ($T_{1/2}$ = 33 y), generated almost entirely from the titanium. The argon inventories at shutdown for the alloy V-15Cr-5Ti exposed in first wall are 4.9×10^{-7} g of ^{39}Ar/kg(V) [6.2×10^{5} Bq/kg(V)] and 2.0×10^{-6} g of ^{42}Ar/kg(V) [1.9×10^{7} Bq/kg(V)]. For the blanket, the inventories are 2.2×10^{-9} g of ^{39}Ar/kg(V) [2.7×10^{3} Bq/kg(V)] and 1.1×10^{-8} g of ^{42}Ar/kg(V) [1.1×10^{5} Bq/kg(V)]. Inventories for V-3Ti-1Si are approximately 60% of these.

Two possible mechanisms can be envisaged for release of the argon after disposal: (1) argon may diffuse out of the metal; and (2) argon could be released during corrosion. The first mechanism is unlikely to dominate since, if the argon has remained immobile in the alloy throughout high-temperature service, it is improbable that the gas will escape in a repository where the temperature is not likely to exceed 350 K. In assessing the second mechanism, relevant corrosion information for the alloys is needed. Since that information is not available for alloys, the behavior of pure vanadium has been taken as a guide. Although vanadium should theoretically corrode under reducing, high pH conditions, in practice it is found that its corrosion behavior is similar to that of a noble metal. Thus the direct disposal of vanadium alloy is tantamount to the employment of large volumes of expensive, essentially inactive metal as a packaging medium for extremely low concentrations of activation products.

The relative volatility of the main activation products suggests a recycling process based on high-vacuum remelting or refining, with immobilization of the liberated argon isotopes in a stable metal matrix of low volume for geological disposal. With adequate initial purity control, several usage cycles should be possible, thus greatly reducing the consumption of vanadium alloy and the volume of waste. However, this approach requires geological isolation. Moreover, the use of recycled material is found not to affect the low off-site accident dose calculated for these vanadium alloys.

6.3.5. Key Issues and R&D Needs

Three critical issues associated with the use of vanadium have been examined. Since vanadium is not a common engineering material, its basic properties, especially under

14-MeV neutron irradiation, are uncertain. An extensive review of the state of our knowledge of vanadium properties is provided in Sec.6.3.3 and in the appendix. A few key areas are highlighted here. Second, some form of electrical isolation between the coolant and conducting walls is probably necessary for using of liquid metal as coolant in a tokamak. For the reference self-cooled design, a CaO coating is postulated, with AlN as a backup material. Research on MHD coatings is still in a very preliminary stage, but this issue is critical for the success of this class of concepts. Third, tritium recovery and control from both Li and He have been examined. Recovery methods have been developed, but the stringent requirements for impurity control (to prevent degradation of the vanadium properties) leads to special concerns.

6.3.5.1. Vanadium material R&D

Considerably more experience is needed in fabricating and joining of V-alloys. The largest heat of V-4Cr-4Ti produced to date within the U.S. Fusion Advanced Materials Program is 500 kg. The anticipated heat for the DIII-D radiative divertor project will be about twice that size. The project offers the potential for expansion of experience in fabricating different shapes and welding of V-4Cr-4Ti to itself as well as other metals. More work needs to be done in characterizing and optimizing welding techniques, particularly electron beam and laser welding techniques. The degree to which a post-weld heat treatment is needed must be determined because it has important design consequences for both assembly and maintenance.

The larger heats (500 and 1,000 kg) of V-4Cr-4Ti offer the important opportunity of generating a more statistically valid set of mechanical properties data for the material in the unirradiated condition. From a design perspective, at least 20 data points should be generated at room temperature for ultimate tensile strength, yield strength, uniform elongation and reduction in area. Several data points at 50 °C temperature intervals up to 700 °C should be generated for these properties in order to establish temperature trend curves. Concurrent with the generation of baseline data for the existing reference V-4Cr-4Ti, additional characterization of the tensile performance needs to be done with respect to Si alloying additions, non-metallic impurities (H, O, C, N) and heat treatment in order to optimize the material from a design perspective. In particular, a substantial improvement would be realized if the ultimate tensile strength could be improved while maintaining the DBTT at a value which is comfortably below room temperature, maintaining the uniform elongation at $> 5\%$, and the fracture toughness and fatigue properties (both yet to be determined) at acceptable levels.

In addition to baseline fracture toughness and fatigue data, thermal creep and time-to-rupture data for V-4Cr-4Ti needs to be generated for temperatures in the range of 600–700 °C and stresses in the range of 125–375 MPa. The issue which should be addressed is whether or not thermal creep limits the design allowable stresses during a period of 2–4 full-power years. Higher-stress/lower-time tests may have to be employed for practical reasons.

The attractiveness of a Li/V design depends greatly on the success achieved in developing a self-healing electrical-insulator coating. In addition to the materials tests which have already been performed, testing in a magnetic field is essential. Concurrent with this testing, laboratory-scale tests need to be performed on non-metallic impurity (*e.g.,* O, C, N) distributions in a system with coated V-4Cr-4Ti and flowing Li. The remaining issue to be addressed is the behavior of hydrogen isotopes in the same system. Depending on whether or not an additional plasma-facing material is used, deuterium and tritium will be implanted into the V-alloy and protium will be generated within the first-wall V-alloy at a rate as high as 62.5-at.%/100-dpa. Calculational models use parameters which lead to at least an order of magnitude of uncertainty in predicting inventory and permeation rates. More data are needed in order for the designer to assess the safety issues related to tritium retention and the performance issues related to hydrogen embrittlement.

The design goal of 100 to 200 dpa for V-alloys requires considerable expansion of the data base. Data on other V-Cr-Ti compositions may be used to justify a lifetime of about 100 dpa for first-wall and/or high-heat-flux components. Shielding lifetimes may be considerably longer than first-wall lifetimes because of lower He/dpa ratios, lower H generation and lower thermal stresses. For the reference V-4Cr-4Ti, the published data base is for $\leq$ 31 dpa and $\leq$ 75 appm He in the temperature range of 420–600 °C. Higher fluence data are required (at least up to 100 dpa) to see if the swelling saturates at $\leq$ 5 vol.%, to determine the irradiation creep rate, and to insure adequate tensile and impact ductility. Given that austenitic and ferritic steels suffer substantial ductility losses when irradiated at 200–400 °C in a thermal or mixed neutron-energy spectrum designed to generate 1–10 appm He/dpa, it is desirable to demonstrate that V-4Cr-4Ti maintains its good uniform elongation and DBTT for irradiation/test temperatures in the range of 300–400 °C.

The U.S. Advanced Materials Program has completed irradiation of V-5Cr-5Ti specimens in EBR-II (COBRA-1A2) up to about 30 dpa in the temperature range of 380–410 °C. The industrial heat of V-4Cr-4Ti has been irradiated to a low damage level (about 4 dpa) in EBR-II (X520) at temperatures in the range of 375–400 °C. Additional tests to higher damage levels and/or lower temperatures are planned for the U.S.

ATR facility and the RF BOR-60 reactor. The BOR-60 irradiation are scheduled for reactor-insertion in August 1995. They are estimated to be in the temperature range of 360–400 °C. V-4Cr-4Ti tubes are being fabricated for insertion into ATR in the temperature range of 200–300 °C to determine in-reactor creep rates. Longer-range ATR tests are in the planning stage for irradiation at 350, 500 and 650 °C. Other facilities are also being considered. The difficulty in planning a meaningful test has to do with transmutations. Thermal neutrons need to be filtered out of the spectrum to prevent excessive Cr build-up. The transmutations which generate He at levels as high as 6.5 appm/dpa in a fusion spectrum are difficult to simulate for the fission neutron energies available. Some success has been achieved in this latter area by allowing tritium to diffuse from the lithium thermal bond within TZM capsules into the V-alloy and then decay to ^{3}He. Aside from being facilities-limited and possibly resource-limited, irradiation testing to design-relevant damage levels is very time-consuming.

6.3.5.2. Insulator coating development

Recent analyses have demonstrated that self-cooled liquid metal blankets in high-field tokamaks are feasible only with electrically insulating coatings at the walls [49]. Without coatings, the MHD pressure drop would be too large to allow adequate heat removal. Different coating materials have been examined for both steel and vanadium structures. For the steel-PbLi system, Al_2O_3 is the preferred candidate, whereas for the V-Li system, both AlN and CaO are considered attractive candidates.

Given that compatible coating materials have been identified, the principal concerns with any coating include: (1) fabrication technology; (2) ensuring adequate resistance and adhesion as-fabricated; (3) ensuring adequate resistance and adhesion under operating conditions (including irradiation and stress fields); (4) effects of flaws on thermal hydraulic performance; and (5) self-healing.

Self-healing is an important consideration because flaws which may develop during operation could seriously degrade blanket performance and lead to failures. Material systems must naturally reestablish the coating by their inherent chemistry.

At this time, CaO is the first choice in the U.S. liquid breeder blanket development program as a coating material because it has higher electrical resistivity than AlN, is more amenable to application in complex shapes, and appears to offer superior rehealing characteristics. Recent development work has concentrated on improving the fabrication methods along with the properties of CaO.

The fabrication of the CaO coating takes place in three steps: (1) Oxygen charging of the vanadium alloy surface (nominally, 650°C in an Ar atmosphere containing 10–20 ppm oxygen. This results in a layer 30–50 mm thick that contains $\sim$ 1 at.% oxygen.); (2) Production of a pure Ca layer on the vanadium surface (nominally, 500°C in a Li-2at.% Ca mixture. This results in a Ca coating 5-10 mm thick); and 3) oxidation of the Ca layer (nominally, 625°C in an Ar atmosphere containing 5000 ppm oxygen).

The resulting coating has been examined microstructurally as well as tested in Li [50]. Initial measurements are encouraging. Additional small scale tests are now in progress to study the effects of changes from the nominal coating conditions on the properties of the coating. A significantly expanded research program is needed to fully resolve this issue.

6.3.5.3. Breeder and tritium control

Tritium recovery and control for lithium. A unique characteristic of the tritium chemistry with the lithium system is the very high solubility of tritium in lithium. At 500 °C and with a tritium concentration of 1 appm, the tritium partial pressure over lithium is only 1.5×10^{-10} torr. Thus, tritium control in a lithium system is usually not an issue. The issue is how to recover tritium from lithium if the tritium concentration is 1 appm.

Many processes have been proposed to recover tritium from lithium [51]. The most developed concept is called molten salt recovery process [52]. The key step of this process is to mix the lithium with a molten salt, during which the tritium will be transferred from lithium to the salt. The tritium from the salt can be recovered by an electrolysis process. All the steps of this process have been demonstrated in a laboratory scale. The feasibility of reducing tritium concentration in the lithium to $\sim$ 1 appm was demonstrated. A key concern for this process is that salt will be dissolved in the lithium during the salt/lithium mixing process. This salt will be carried back to the fusion core. The impact of the salt on the lithium corrosion characteristics and lithium chemistry is uncertain. Thus, the applicability of this process for a fusion reactor is in doubt.

During the ITER Conceptual Design Activity, a tritium recovery process based on cold trapping was developed to recover tritium from lithium. The cold trap process was demonstrated to be able to recover tritium from lithium to the saturation limit, as shown in Fig. 6.3-12. The key step of the process developed for ITER was to add protium in the lithium. The protium concentration was increased to about 1,000 appm. Thus, at 200 °C,

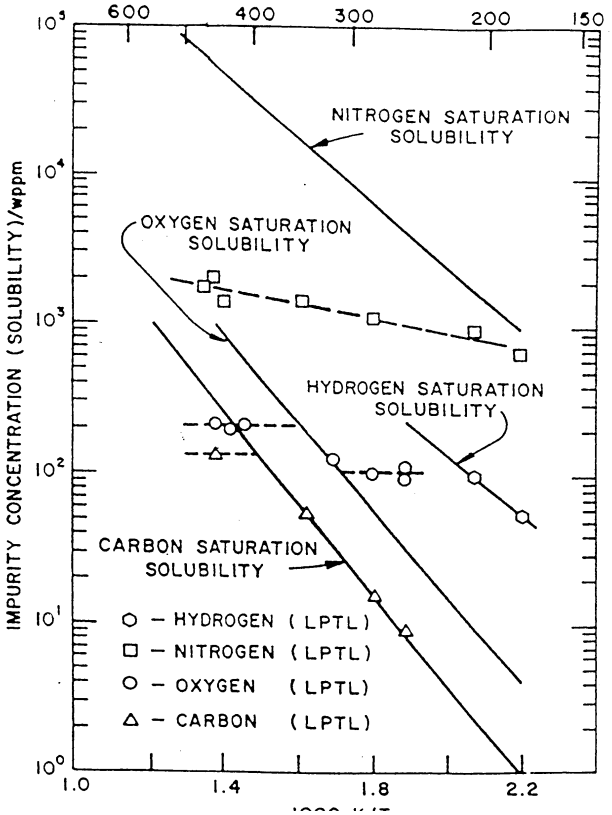

Figure 6.3-12. Cold trap process parameters.

Li(H+T) was super-saturated and would precipitate out. This process was identical to the cold trap process developed for the fast breeder program. In that process, Na(H+T) precipitate out in the cold trap and no isotope effect was observed. The Li(T+H) can be separated from the lithium by gravitational force, which was also demonstrated in the breeder program (called a meshless cold trap). The Li(H+T) will decompose in a drained cold trap to hydrogen gas at 600 °C. The T and H will be separated by an isotope separation system based on cryogenic distillation. Because the saturation limit at 200 °C is 440 appm, which is far above the design goal of 1 appm, the cold trap process was abandoned for tritium recovery from lithium in ITER.

Tritium control and recovery from He-cooled designs Tritium control and recovery from He is not a simple process when the tritium partial pressure requirement is as low as required. The tritium permeation across the first wall from the plasma has been calculated to be of the order of 10 g/d including the effect of a diffusion barrier. With a permeation rate of 10 g/d, the tritium partial pressure increase is 10^{-2} Pa per

pass. If a closed cycle gas turbine is used for energy conversion, a heat exchanger will be required for heat rejection. For a heat-exchanger temperature of 300 °C and a surface area of 20,000 m^2, which is made of 316 SS (a material with rather poor permeability of hydrogen), the tritium partial pressure has to be controlled to be lower than 3×10^{-7} Pa to limit the tritium permeation rate in the heat exchanger to no more than 10 Ci/d. If a tritium diffusion barrier can be provided on the surface of the heat exchanger, the tritium partial pressure has to be maintained at 3×10^{-3} Pa, which is still lower than the vacuum of the plasma. Thus, the increase in tritium partial pressure during each pass of the He-coolant across the reactor is higher than that acceptable by the heat exchanger, *i.e.,* the entire reactor coolant has to be processed to remove the tritium permeated across the first wall. Since the flow rate of the He-coolant is much larger than that for the purge gas, this process could be very expensive.

For He-cooled systems with liquid lithium breeder, tritium recovery from the breeder is similar to that of self-cooled Li/V designs. For systems with solid breeders, a purge system has to be utilized. Figure 6.3-13 shows the tritium process system for a solid

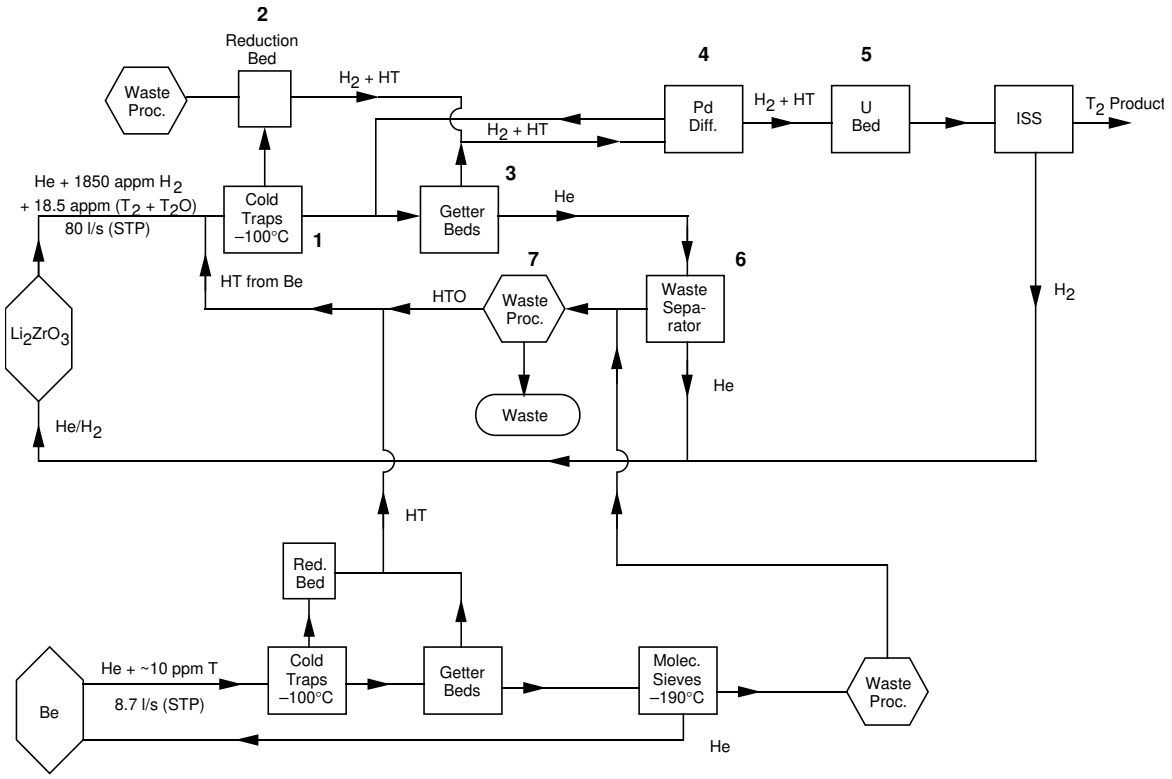

Figure 6.3-13. Tritium process system for a solid breeder blanket.

breeder blanket. The purge stream will have to be cooled to $\sim 100\,^{\circ}\mathrm{C}$ to cold trap the hydrogen isotopes in the purge. Due to the small mass flow rate of the purge gas in this case, the power requirement and the size of the equipment for this step is acceptable. However, this step could be excessively expensive if the entire coolant has to be processed this way. Tritium also can be recovered by an oxidation process to form HTO. The cold trap temperature to recover HTO does not have to be as low as for the HT. However, this method will introduce excess oxygen and cannot be recommended for the V-system.

6.4. SILICON-CARBIDE COMPOSITE DESIGNS

6.4.1. Design Options

Silicon-carbide (SiC) composite material with a projected allowable temperature capability $\geq 1000\,^{\circ}\mathrm{C}$ was selected as the structural materials for ARIES-I [2] and ARIES-IV [3] reference and alternate blanket and divertor designs. These designs have been used as the basis for assessing the advantages and issues associated with a possible Demo power plant based on SiC composites as the primary in-vessel structural material.

To take full advantages of the low activation and high temperature capability of SiC composite material, 5–10 MPa helium was used as the coolant. ARIES-I used Li_2ZrO_3 as the solid tritium breeder, Be metal sphere-pac as the neutron multiplier, and W as the divertor coating material. Based on new experimental results, Li_2O was selected as the solid breeder for the ARIES-IV designs (to eliminate Zr activation issue). If the use of W can be avoided as the divertor coating material, then an inherently safe design (LSA = 1) can be obtained. This also assumes that the Be chemical energy and toxicity concerns are resolved.

Both ARIES-I and ARIES-IV alternate designs used the toroidal flow, nested shell blanket configuration, where the SiC composite components can be made from smaller ceramic (about 1 m $\times$ 1 m) parts. Reliability of this configuration depends on the successful development of ceramics joining techniques. The ARIES-IV reference design has a poloidal flow configuration. This relies on the successful development of the fabrication of large ($>$ 1 m wide, $\sim$ 1 m deep and $>$ 7 m in height components) leak-tight SiC composite components.

Both ARIES-IV reference and alternate blanket designs satisfy all of the neutronics and thermal hydraulic performance requirements of Demo. Except for the need of Be-neutron multiplier, both designs will have excellent safety characteristics. We also found

that by increasing the helium pressure to about 12 MPa, and taking advantages of the improved recuperator performance of the closed cycle gas turbine system, at a helium outlet temperature of about 950 °C, a gross thermal efficiency of about 55% can be expected. In the evaluation of the use of SiC-composite as the structural material for the Demo design, there was no doubt of its projected benefits; the key question is on whether its development schedule can meet the projected schedule of Demo given the small R&D effort on this material in U.S.

6.4.2. Key Issues

Key issues for the application of SiC composite are in the areas of material development that can match the schedule of the U.S. Demo design, the behavior of the composites in a fusion environment, the need for electrically-conducting components for plasma stability, and the development of robust plasma facing components (PFC). Fundamental improvements in material irradiated properties, such as thermal conductivity, are needed, for example by using advanced SiC fiber and interface materials. Other material development issues include economic fabrication of large SiC-composite components, development of vacuum leak tight components, techniques for brazing ceramic parts, and the development of the joining techniques of SiC composite to metallic parts.

Most advanced tokamak scenarios require a close-fitting conducting shell to stabilize kink modes. A separate shell may be needed behind the blanket for passive stabilization of axisymmetric modes (vertical stability). If metallic shells should be used in regions of high-neutron fluence, the safety rating and thermal performance of the plant may be impacted.

Various techniques of leveling the surface heat flux, such as the use of the radiative divertor approach is essential, since it dictates the feasibility of removing surface heat flux by helium coolant and the utilization of low activation material for the PFC surface and components. The concurrent reduction in the ion energy to < 5 eV is necessary to maintain low surface erosion and therefore, adequate component lifetime and to maintain the low activation benefits of the SiC composite design without the use of high-Z surface material, such as W.

6.5. MAGNET SYSTEMS

Several magnet issues related to licensing and commercial acceptance of fusion tokamak power plants have been addressed. First, several types of faults on both the poloidal and the toroidal field systems were analyzed. Results of these studies are presented in Secs. 6.5.1 and 6.5.2. Second, because the maintainability and availability are important Demo requirements, access to the blanket and shield as well as removal and repair of the magnet system have been considered. Section 6.5.3 covers discussion of several methods to provide the dewar/cryostat system for the toroidal field system, with the investigation addressing the relevance of the possible designs to the maintenance of the magnet system and the blanket/shield. Finally, Sec. 6.5.4 deals with the structural issues on the toroidal field coil that arise from enlarging substantially the access port in the outer leg of the toroidal field coils.

6.5.1. PF Fault Analysis

In this section some failure modes of the poloidal-field coils are analyzed. Since detailed parameters necessary for this type of calculation were not available, a well documented design, TPX was chosen for carrying out the evaluation. Parameters not in that report were obtained from scientists at Princeton Plasma Physics Laboratory. One of the reasons for analyzing TPX rather than ITER was that the Demo, as well as TPX, are up-down symmetric (up-disruptions are different in ITER from down-disruptions).

In order to determine the worst loads, it is necessary to carry out an evaluation for a full, time-dependent discharge scenario. Two classes of failure modes were analyzed, each starting with a plasma disruption. In the first class, a PF system dump occurs some time after the disruption. In the second class, a short circuit in the terminal of only one PF coil occurs some time after the disruption. This short circuit is then followed by discharge of the remaining PF coils through their dump resistors. Obviously the number of combinations of these fault scenarios is very large. For the first class of faults, the PF coil dump can occur at any time after the disruption (three delay times of 0, 0.5, and 1 s were considered here). For the second class of faults, the short can occur in any PF coil (short circuit of all 14 PF coils, one at a time, were analyzed) and at any time after the disruption (three delay times of 0, 0.5, and 1 s were considered here).

The magnet system should be designed so that it can handle the largest load in a given coil or element occurring during normal operation or faults. Therefore, for each fault discharge scenario outlined above it is necessary to calculate the stresses in all

the coils and then to determine the coil with the highest stress and/or force. Due to the large number of items (stresses, forces) that need to be monitored, a limited set of parameters were chosen to represent the complex time-dependent forces and stresses in the coils. They are: (1) Maximum compressive forces on the central solenoid (CS) interfaces; (2) Maximum tensile (separating) forces on the CS interfaces; (3) Maximum differential hoop force per turn between the CS coils; (4) Maximum differential hoop force per turn between the end coils of the CS and the adjoining retaining plates; (5) Maximum compressive hoop force per turn in any individual coil of the CS; (6) Maximum tensile hoop force per turn in any individual coil of the CS; (7) Maximum and minimum vertical body forces on the CS stack; and (8) Maximum tensile/compressive/vertical/centering loads in each of the poloidal field ring coils (excluding the coils in the CS). In addition, the effects of PF coil failure on the toroidal field (TF) coils was estimated by monitoring the following: (1) Maximum out-of-plane force on either upper or lower TF coil; (2) Maximum out-of-plane moment on either upper or lower TF coil, calculated about the equator of the machine; and (3) Maximum out-of-plane moment on either upper or lower TF coil, calculated about the axis of the machine. In total, 23 quantities were calculated and monitored.

The axisymmetric model used in the calculations included the plasma, the PF coils, the inner coils, and the passive structure. The TF coils are modeled with 3-D lumped current filaments carrying a current of 2.8 MA. The programs EIGENCIRC [53] and SOLDESIGN [54] with postprocessors for force calculations were used in the studies. It was assumed that some of the coils are connected in series. The plasma disruptions were modeled using 9 discrete plasma positions. It was assumed that the time constant for the plasma drift prior to the disappearance of the plasma current (disruption) was 0.1965 s. It also was assumed that the plasma current disappeared instantaneously at the end of the plasma drift. The PF coils were flux conserving during the disruption. The current in the passive elements were assumed to be zero prior to the disruption. In order to include the finite PF currents due to currents in the passive elements after the plasma current decays to zero, the calculations were carried out 5 s after the end of the plasma decay. By this time the currents in the passive elements were essentially zero.

In order to summarize the results in the most compact and convenient manner, the maximum stress or force was normalized to the maximum loading during normal operation. This would indicate safety margins that should be included in the coil designed for normal operating conditions. Table 6.5-I shows the worst-case values for the 23 monitored quantities over all the fault discharge scenarios. The results indicates that with a few exceptions, a design based on the normal scenario operation is robust enough to

Table 6.5-I.
Maximum Normalized Force or Stress During the PF Fault
(Normalized to the Maximum Normal-Operating Quantity)

Central Solenoid:	
Compressive	1.03
Separation	1.24
Diff. hoop/turn on coil interface	2.97
Diff. hoop/turn on retaining plates	1.81
Hoop/turn - compressive	2.40
Hoop/turn - tensile	2.13
Vertical body - upward	7.63
Vertical body - downward	1.23
PF5:	
Hoop - compressive	12.12
Hoop - tensile	1.10
Vertical - centering	1.00
Vertical - launching	1.24
PF6:	
Hoop - compressive	1.34
Hoop - tensile	1.00
Vertical - centering	1.17
Vertical - launching	1.76
PF7:	
Hoop - compressive	1.70
Hoop - tensile	1.01
Vertical - centering	1.37
Vertical - launching	1.00
TF:	
Side force on half of TF coil	1.23
Moment on TF coil about equator	1.37
Moment on TF coil about major axis	1.71

handle the fault conditions. These exceptions include: (1) Hoop loads in the central solenoid; (2) Launching force in the central solenoid; and (3) Launching force on the divertor coil (PF5). The support of the compressive loads can be provided, and should be of interest mainly for preventing buckling of the coils.

6.5.2. TF Fault Analysis

The fault analysis of the TF coils was carried out in an ITER-like system, since the toroidal field coils are more similar to those presently being considered for the DEMO with poloidal shells, as opposed to radial plates (as in the ARIES-I design) or with a conductor winding inside of a case (as in TPX). The fault analyzed here is one in which a short is postulated across the terminals of one of the TF coils and the rest of the TF coils discharged through their dump resistors. This is a plausible failure mode as it could happen either when a coil short is detected and the TF coil system is shutdown, or when the short occurs shortly after the beginning of a TF coil dump.

Circuit simulations of a concurrent dump of the remaining coils results in a very high overcurrent in the shorted coil. A quench develops before the full development of this current. The coupling between the circuit equations and the thermal hydraulic calculations that model the quench behavior of the conductor is complicated. If the shorted coil does not quench, the current in the shorted coil increases to 350% of its nominal value during the discharge of the rest of the TF system. However, with these currents at TF field, the coil is likely to quench. It was determined that 5 s into the coil dump, the field and current in the shorted coil were such that the conductor went into the current sharing mode (with current in the normal conductor in parallel with the superconductor) at the operating temperature. A quench was postulated at this time, and the circuit calculation carried out from this point with "internal" dump of the shorted coil. It was assumed that either 10% or 100% of the shorted coil was in the normal state, or that 300 m of the conductor quenched with quench propagation. These assumptions will have a greater effect on the ultimate temperature of the conductor rather than on the worst case structural response. For the cases analyzed, the pack current did not increase beyond 100 kA (about 250% nominal value).

Understanding the consequences of the entire history of this event will require further simulation, and finding the limiting structural condition will require the analysis of the time of the PF scenario and the decision to discharge the PF coil. In order to estimate the structural response, two points in this scenario are analyzed. Point (A) is early in the fault when the PF coils are at their full end-of-burn currents. It was assumed that

the current in the shorted toroidal field coil was at 120% of nominal current while the currents in the other TF coils were decreased to 80% of the nominal value. Point (B) is later in the fault, when the PF coils are de-energized. At this point, there is a large overcurrent in the shorted coil and the remaining TF coils also have substantial currents, which produce significant structural interaction with the shorted coil. For this case, it was assumed that the current in the shorted TF coil was at +250% of the nominal current while the currents in the rest of the TF coils were at 50% of nominal value.

A simplified model of the entire tokamak has been constructed. The TF coil has been constructed with beam elements, and coarser plate and solid elements have been used throughout. The modeling approach eliminates credit for symmetry and adds non-linear gap elements where major structural components interact. The model is intended to be simpler than models used previously for NET, but sophisticated enough to allow the major phenomena to be identified for a full complement of loading and structural interactions. The keys are modeled as a continuous shell of plate elements. This was intended to simulate the torque-shell behavior of the assembly of keys and TF plates. It also simulates the toroidal bearing stress which results if neighboring coils are attracted to one another.

The loads in the toroidal field coils are shown in Figs. 6.5-1 and 6.5-2 and Table 6.5-II. The centering load refers to the radially inward load in the vertical section of the coil (inboard side). The upper half-bursting load refers to the integrated vertical load of the upper half of the coil. Obviously, point (B) produces the worst condition with a much increased vertical bursting loads. These loads result in increased tension in the coil. In addition, there are very large bending stresses in the shorted coil (Figs. 6.5-2). This is basically due to the fact that the system is far away from bending free, since the shorted coil is about twice the current and the neighboring coils are half the nominal value. The coil, therefore, attempts to become bending free, especially since the poloidal shells of the TF coils have very limited capability for carrying bending stresses. Only the intershell bond can carry much bending. The large bending stresses depend therefore on the integrity of the plate-to-plate bond and will probably be relieved by bond failure. The shorted coil (with 250% overcurrent) has bending stresses of about 600 MPa, while the other coils are only slightly loaded.

In summary, the failure modes analyzed here result in large deformations of the shorted toroidal field coil. It is, therefore, necessary to modify the design in order to be able to support the bending loads that result from this failure mode. This issue is addressed in Sec. 6.5.4.

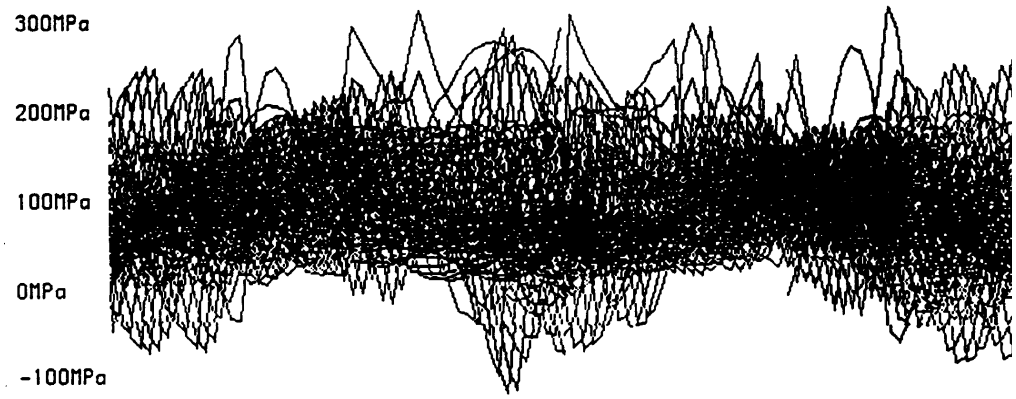

Figure 6.5-1. Bending and tension for the four corners of the beam elements for all 24 coils of the model at Point (A) during the fault.

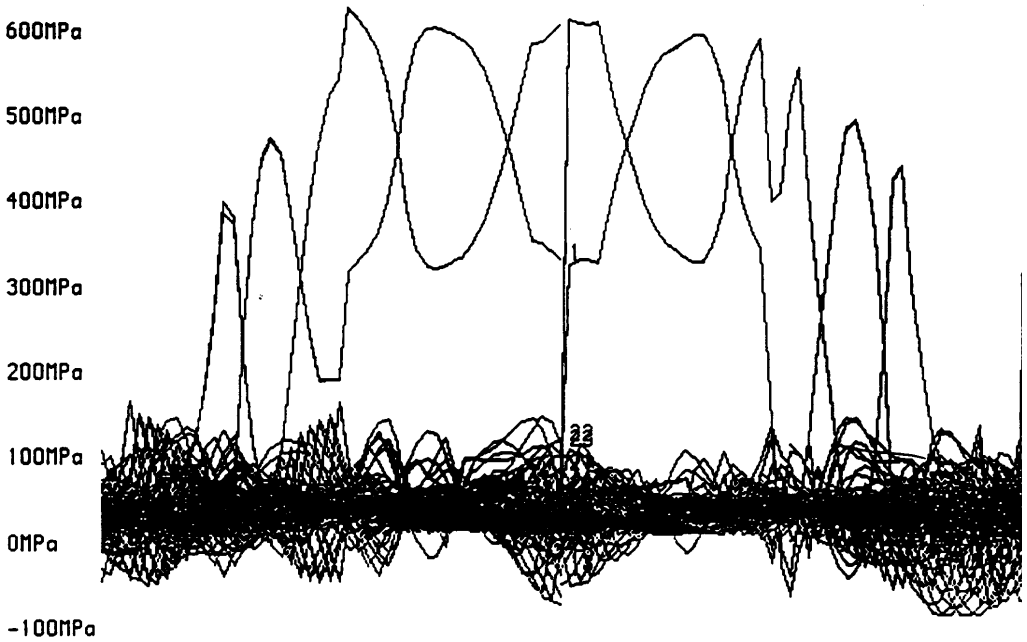

Figure 6.5-2. Bending and tension for the four corners of the beam elements for all 24 coils of the model at Point (B) during the fault.

Table 6.5-II.
Analysis of TF Coil Loads During Fault Conditions

	Centering (MN)	Upper-Half Bursting (MN)
Nominal load		
Global Model	–318	313
Point (A):		
Stick model	–278	336
Point (B):		
Single coil model	–411	700
Stick model	–372	731

6.5.3. Cryostat and Dewar Design

The maintenance scheme for ARIES-I and ARIES-IV designs included removal of an entire fusion core sector (1/16 of the torus corresponding to 16 TF coils). In ARIES-I, a separate dewar and cryostat was used for each coil. The TF coil was removed with a sector during the maintenance operation. In ARIES-IV, the entire TF coils were located in one cryostat. The outer leg of the TF coils were extended to allow removal of an entire sector radially in between the TF coils. This latter option has a larger and, thus, more expensive TF system. In this section feasibility of separate dewar/cryostat for each coils are investigated.

The ARIES-I design utilized a partial cryogenic dewar as shown in Fig. 6.5-3. There are insulating vacuum gaps only in the regions that face the warm regions. In regions that face other cold regions, only the vacuum boundary is present without the presence of insulating material (such as multi-laminar insulation, or superinsulation). The gaps in-between vacuum boundaries shown in Fig. 6.5-3 will fill up with frozen material: ice and frozen oxygen or nitrogen. It was expected that the thermal conductivity of the slush

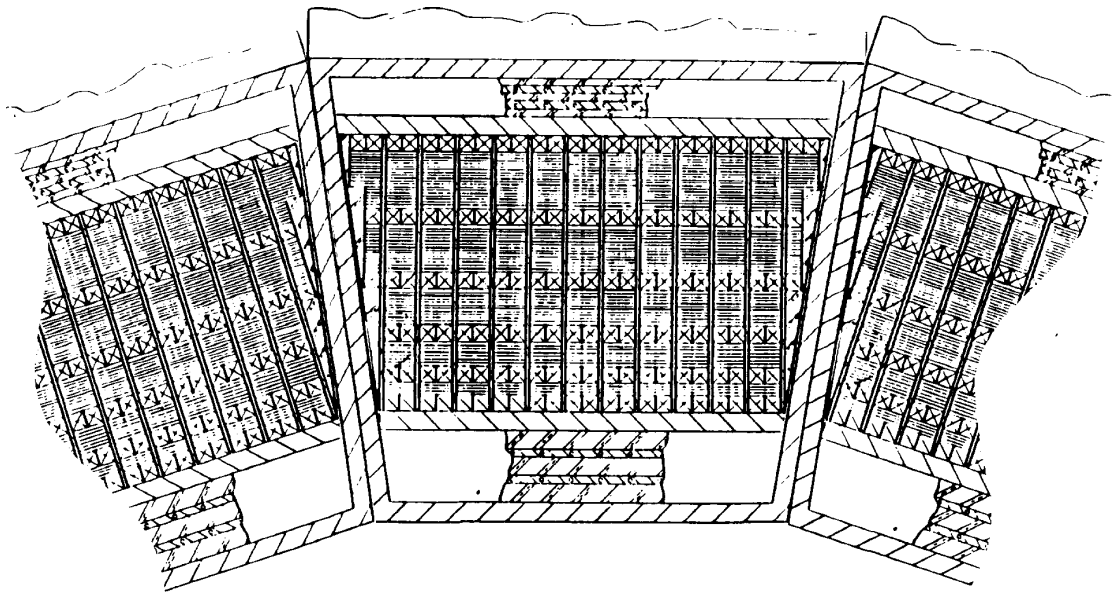

Figure 6.5-3. Design with individual cryostat over each coil, with no thermal insulation between adjacent cold coil elements (coil-to-coil, or coil-to-cap).

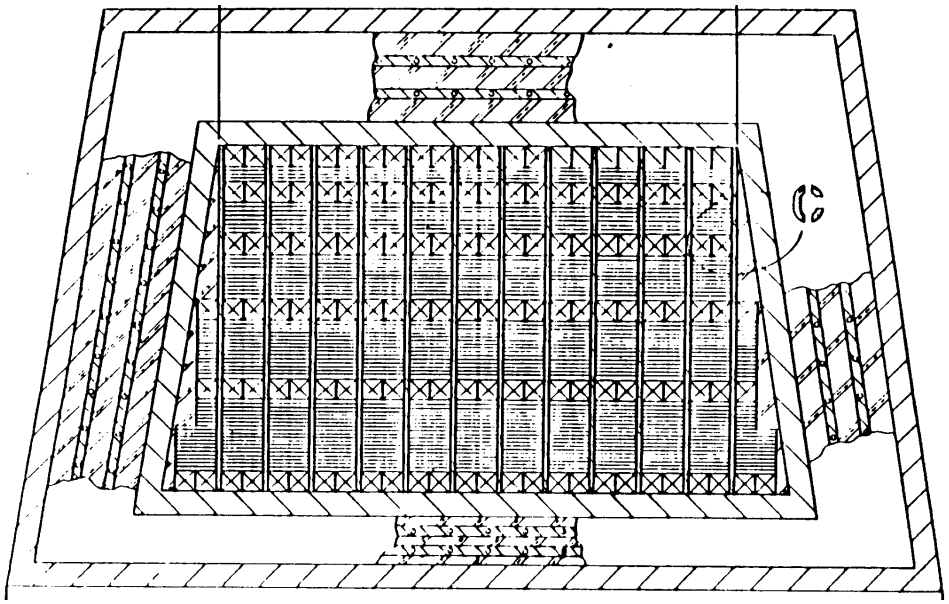

Figure 6.5-4. Design with individual cryostat over each coil, with thermal insulation between adjacent cold coil elements (coil-to-coil, or coil-to-cap).

that is formed in this manner would have very low thermal conductivity. In this manner it would be possible to prevent warm-up of the regions of the coil that are adjacent to the corner region that faces both a warm and cold region.

The alternative is shown in Fig. 6.5-4 with large insulating gaps all around the coil. The main advantage of this approach is the absence of large cross sections of the coil not filled with either structural material or conductor. In addition, it is possible to transfer loads effectively across the coil boundary (from coil to coil, or from coil to bucking cylinder or out-of-plane structure). The superinsulation or G-10 spacers are good for transferring the load in compression, but are not very effective for transferring shears.

Volume changes occur due to phase transformation and due to volume expansion as water goes from liquid to solid (a 9% increase in volume). This expansion would place both the magnet and the water in compression. As the temperature decreases, there are phase transformations of the ice. A phase diagram at 4 K is shown in Fig. 6.5-5 as a

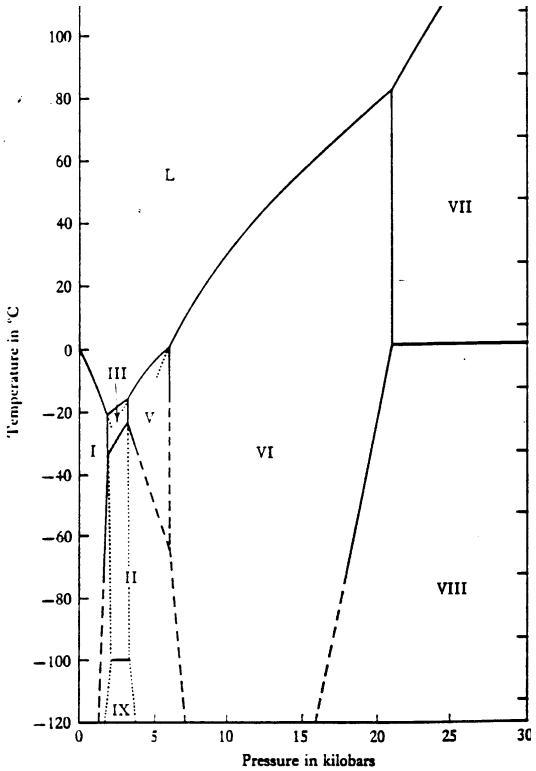

Figure 6.5-5. Phase diagram of ice. Broken lines represent presumed phase boundaries which have not yet been fully investigated. Dotted lines represent metastable continuations of one phase into a neighboring region.

function of the compressive stress. The phase Ih has a hexagonal crystal structure with density of 0.92 g/cm^2. The phase IX (and III) has a tetragonal crystal structure with a density of 1.14 g/cm^2 (as measured at -175C and 1 bar). This means a 24% volume reduction if phase changes from Ih to IX at the same conditions.

Stress strain studies were carried out at MIT in order to investigate the behavior of the ice. Tests were performed at a MTS machine with a liquid helium cryosystem. The ice in the test chamber was made from local (Cambridge) tap water by fast cooling with liquid nitrogen. Partial results of stress-strain tests are shown in Fig. 6.5-6 [55]. The results at different load rates and at different temperatures show the same features: (A) the load is released repeatedly, starting from a critical stress in the loading process; (B) the release period increases as the load increases; (C) the released load value increases as the load increases; (D) a similar phenomenon with load jumps occurs in the unloading process. The directly measured strain data of ice as a function of stress has provided support that these features are material properties of the ice. The behavior of ice in unloading process further indicates this features are due to the phase transformation of ice.

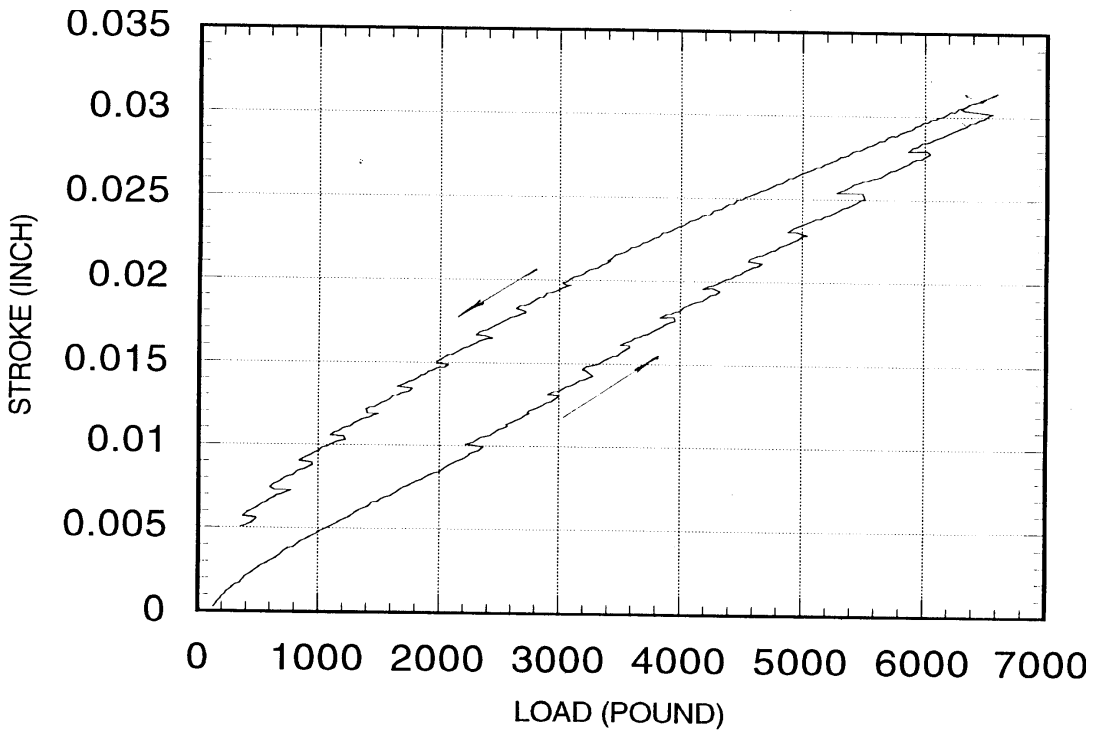

Figure 6.5-6. Ice test results at a load rate of 10 lb/s and at 77 K

As a load is applied on a cylinder of ice, there is a stress gradient due to the wall friction. As the load increases to a critical number, a top part of the ice first reaches the critical transition point, a phase change of Ih to IX leads to a volume reduction of ice and to a load release. As the load increases, the portion of ice reaching at the critical point increases. As the load is decreased, the process is symmetrical.

The thermal effects of the ice layer have been explored. Figure 6.5-7 shows the thermal conductivity of ice at the low temperatures [56]. The thermal conductivity of ice increases with decreasing temperature (approximately inversely with temperature to about 10 K). At cryogenic temperatures it is about 3 orders of magnitude larger than the heat conductivity of G-10, a good low temperature insulation material. This implies that the gap between adjacent coils has to be small. It will be necessary to add insulation at the side of the coils, as shown in Fig. 6.5-4.

A preliminary design of the insulation has been performed. There are three low thermal conductivity paths linked in series by two heat sinks stationed nominally at

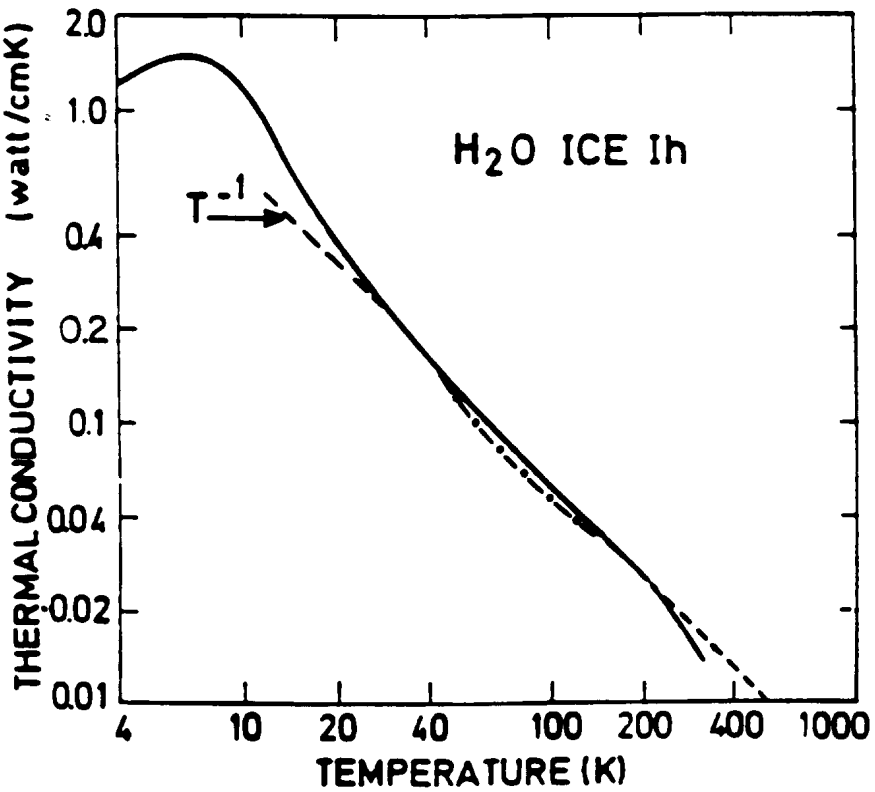

Figure 6.5-7. Thermal conductivity of ice at cryogenic temperatures.

Table 6.5-III.
Thermal Conductivity Integrals and Heat Balance Conditions

Temperature range (K)	Thermal conductivity integral (W/m)
20 to 4.2	2.212
80 to 20	20.1
300 to 80	165.0

Temperature (K)	Net heat in (W/m^2)
20	357.8
80	2,898

20 and 80 K. The out-of-plane structure need not be symmetric because the loads are asymmetric. The typical thermal conductivity integrals of G-10 in the temperature range 4.2 to 300 K is calculated. The values for the three temperature ranges are shown in Table 6.5-III.

The heat sink consists of stainless steel plates grooved and welded. Helium at 30 atm is circulated as the coolant. The G-10 spacers are on the order of 5 cm thick. The heat balance condition in the two heat sinks are shown in the bottom part of Table 6.5-III. In both these cases the cooling of the heat sinks by helium at 30 atmospheres presents no problem. Both the temperature rise in the helium and the pumping power are small.

The above discussions show that (1) Design with a cryostat as in Fig. 6.5-3 is not attractive; and (2) Design with a cryostat as in Fig. 6.5-4 is feasible, but requires about 15 cm all around each toroidal field coil. The 0.15-m dewar boundary around the each TF coil requires a large fraction of the coil cross section of the TF coil in the inboard side of the machine which increases the cost of the device dramatically. Therefore, it appears that the most cost-effective method is to locate the entire TF system in a cryostat and extend the outer leg of the TF coils to allow removal of an entire sector radially in between

the TF coils. In the next section, the impact of these large access ports in between the TF coils are discussed.

6.5.4. Structural Effects of Large Access Port

In this section a structural model is used to investigate the different methods of supporting the Lorenz loads in the toroidal field magnet. In particular, the out-of-plane loads require special attention because the structures used to support them interfere with the maintenance of the fusion core. A similar approach to the one described in Sec. 6.5.2 is used in this section. Only normal conditions (end-of-burn) have been analyzed. Four models have been investigated, aiming at removing most material in-between the outer legs of the toroidal field coils. The outer leg of the toroidal field coil has been moved sufficiently back so that an entire fusion core sector can be removed through the gap in-between the coils with a purely radial motion.

The First model is shown in Fig. 6.5-8. It includes a cap (attached to the bucking cylinder), but no additional structure in the region of the outer legs of the TF coil. The thickness of the cap is the same as the thickness of the bucking cylinder. The cap is attached to the toroidal field coil through a key that runs along the toroidal field coil and the cap. In this manner, the TF coil and the cap are locked in the toroidal direction but the coil is allowed to slide in the poloidal direction.

The stresses in the toroidal field coil are shown in Fig. 6.5-9. The peak stresses (assuming smeared properties for the toroidal field coils) are 1.4 GPa in the area where the cap ceases to support the toroidal field coil. In this case, the caps are rotating, taking along the coil (with little capability to prevent the motion). The TF coil, therefore, experiences a strain-controlled condition, and the coil takes on the typical S-curve shape. The coil experiences very large stresses across the region where the bending of the coil is maximum. In addition to the large loads in the region where the cap ends and the TF coil is self-supporting, there are large in-plane bending stresses at the top-bottom inner chord of the coil, as the coil and the structure react to the large displacement of the caps. At the inside surface, top and bottom, the stresses are 1.2 GPa. These stresses are very large, and need to be reduced.

The second model, shown in Fig. 6.5-10 includes a reinforcement of the TF coil, by placing structure directly behind the outer leg of the TF coil. This structure is connected to both the outer leg of the coil and to the upper and lower caps. The goal is to increase the structural material in the outer section of the TF coil in order to increase the moment

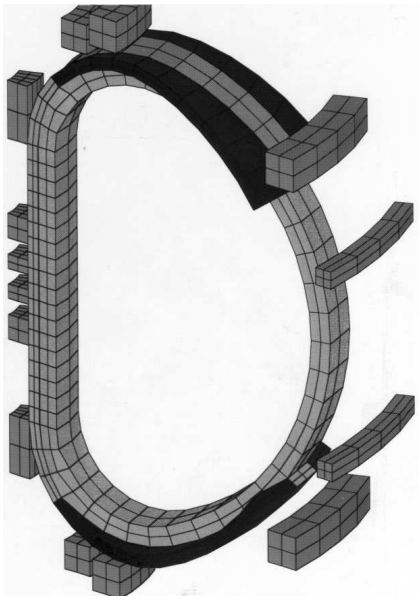

Figure 6.5-8. First model, with caps but no structure behind the outer leg of the TF coil.

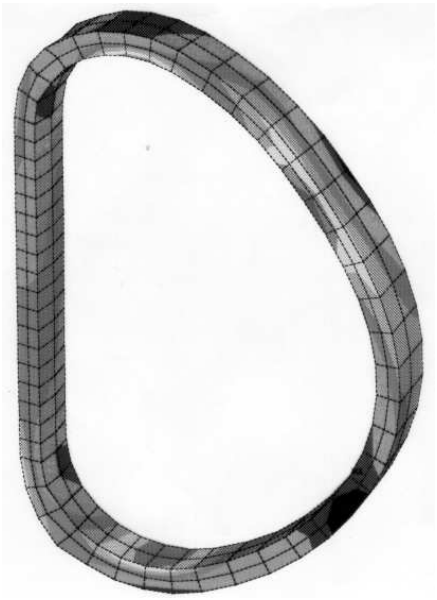

Figure 6.5-9. Stresses in the TF coil for the first model, with 1.4 GPa maximum stress in the region where the cap stops, and in the inner chord of the coil, top and bottom, due to bending.

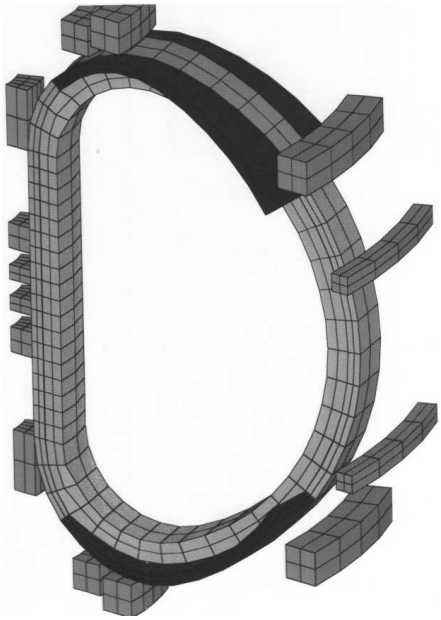

Figure 6.5-10. Second model, with caps and structure (same thickness as the caps) directly behind the outer leg of the TF coil.

of inertia, and to decrease the rotation of the caps by reacting through shear stresses in the structure directly behind the outer leg of the TF coil. The thickness of the structure in this region is the same as the thickness of the cap (which is the same as the thickness of the bucking cylinder). In addition, the cap is attached to the bucking cylinder both for rotation and for tension. In this manner, the cap helps support the in-plane tension of the coil, and provides for rigidity in the case of TF-coil failure (short of a TF coil followed by dumping of the rest of the TF coils, see Sec. 6.5.2).

The coil stresses for the second model are shown in Fig. 6.5-11. The stresses in the region where the cap stops being toroidally continuous (and where the stresses are 1.4 GPa in the previous model), are reduced to about 600 MPa. In addition, the stresses in the cap near the top and bottom of the machine are small, less than 60 MPa. The cap thickness has been kept constant, however, because making it thinner would result in larger rotation of the cap and coil in the outer legs of the toroidal field coil. It could be made thinner, however, by using truss elements, or by placing structure in-between toroidal field coils in the region underneath the caps. The peak stresses in the structure directly behind the outer leg of the toroidal field coil are about 2 GPa, as shown in Fig. 6.5-12, in the region close to the location where the full cap ceases to be toroidal

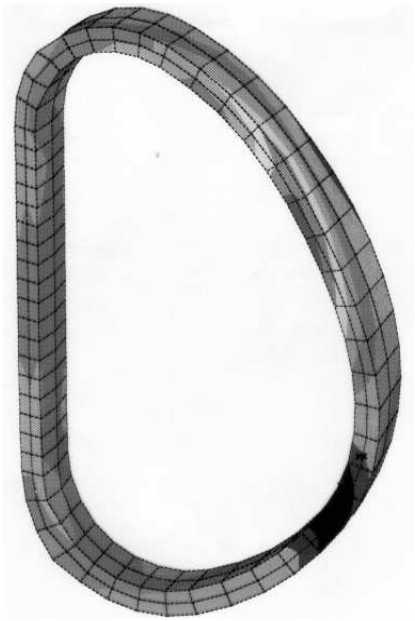

Figure 6.5-11. Stresses in the toroidal field coil for the second model, with 600 MPa bending stress in the region near the discontinuity of the cap.

Figure 6.5-12. Stresses in the external structure for the second model, with 2-GPa bending stress in the structure directly behind the outer leg of the TF coil.

continuous. It is necessary, therefore, to further reinforce the structure directly behind the outer leg of the coil, as described below.

In order to decrease the stresses, the structure directly behind the outer leg has been further increased. Two models of this case have been developed. In the first one (Fig. 6.5-13), the height of the caps is such that the inner components of the fusion core can be removed by simple radial motions. However, there is insufficient space for piping. A fourth model, shown in Fig. 6.5-14 was developed with even taller ports. The stresses in the external coil structure for the third model are shown in Fig. 6.5-15. The stresses are acceptable with the exception of the region in the inboard section of the structure in the outer leg, next to the region of discontinuity of the caps. The stresses in this region are on the order of 1.2 GPa (down from 2 GPa). This is due to the large displacement of the caps. If the port height were to be increased, the radius of curvature needed to deform the coil and the structure directly behind the outer leg would decrease, as would the stresses. However, this would occur at the expense of increased displacement (rotation).

Figure 6.5-16 shows the stresses in the TF coil for the fourth model (with larger ports). Again, the stresses peak in the region above and below the coil, but the peak stresses are only 450 MPa. The stresses in the external coil structure (cap, bucking cylinder and coil-shadow) are shown in Fig. 6.5-17. The stresses have decrease to about 700 MPa in the structure. However, increasing the height of the port (even though it decreases the stresses), increases the displacements of the cap and toroidal field coil. The displacements are shown in Fig. 6.5-18. The maximum displacement in this case is 0.05 m, while in the previous case (third model) the maximum displacement was less than 0.04 m.

In conclusion, the alternatives for supporting the TF coils have been analyzed, and one design with ports large enough for radial access to fusion core sectors has been evaluated. The structure needs to be poloidally and toroidal continuous. The caps will be keyed together, and attached to the bucking cylinder with an arrangement similar to that in the ITER design (hole and pin). The performance of this design should be established through further detailed analysis.

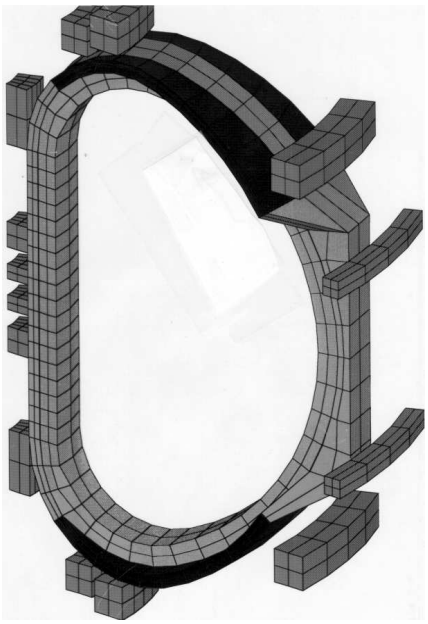

Figure 6.5-13. Third model, with caps and reinforced structure directly behind the outer leg of the TF coil.

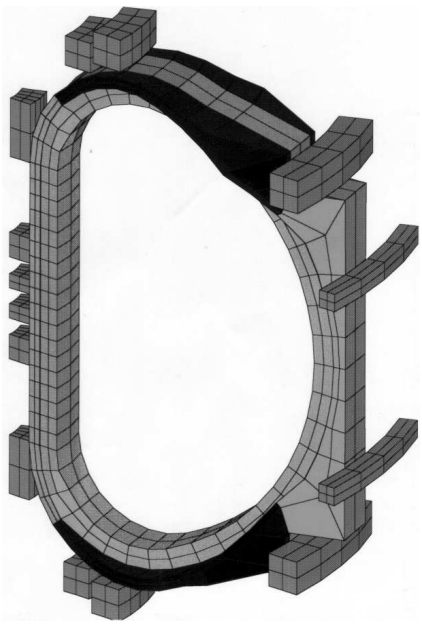

Figure 6.5-14. Fourth model, with increased port height and reinforced structure directly behind the outer leg of the TF coil.

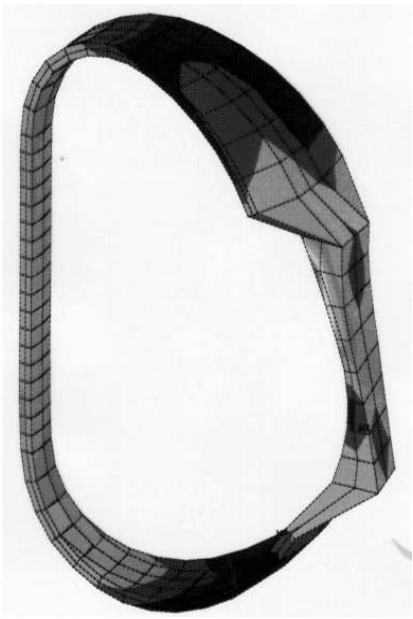

Figure 6.5-15. Stresses in the external coil structure for the third model, with 1.2 GPa maximum stress in the region where the cap stops.

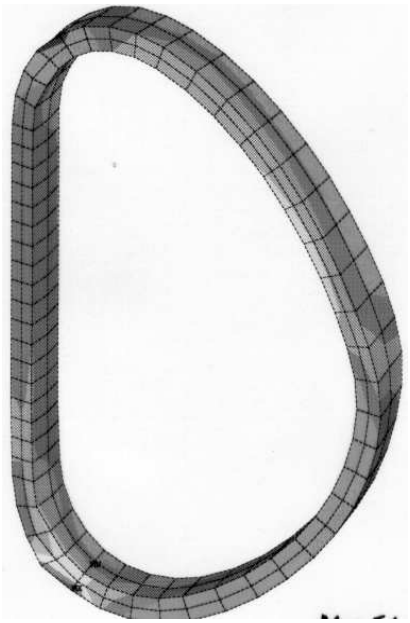

Figure 6.5-16. Stresses in the toroidal field coil for the fourth model with 450 MPa maximum stress in the inboard side to the coil, top and bottom.

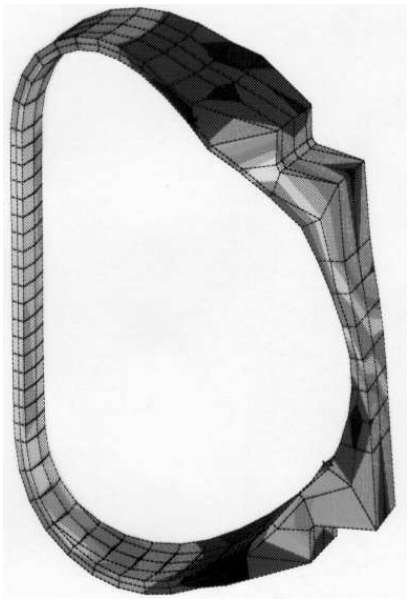

Figure 6.5-17. Stresses in the external coil structure for the fourth model with 700 MPa maximum stress in the region where the cap stops being toroidally continuous.

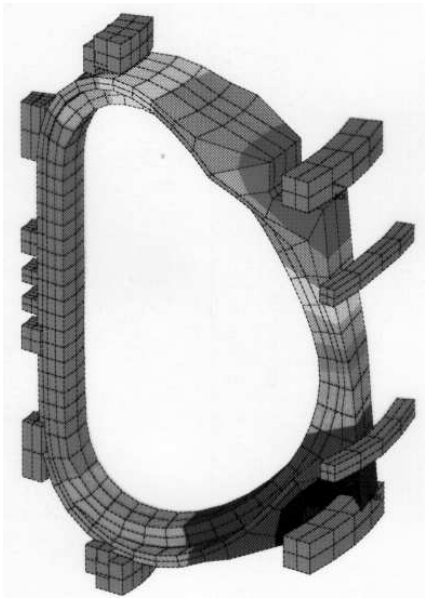

Figure 6.5-18. Displacement in the external coil structure for the fourth model with 0.05-m maximum displacement in the region where the cap stops being toroidally continuous.

6.6. SUMMARY AND CONCLUSIONS

Three major classes of engineering design options have been examined to determine if they meet the Demo requirements and to characterize the remaining technical issues. The design options were categorized according to the primary in-vessel structural material – ferritic steel, vanadium alloy, or SiC composite.

Silicon-carbide composite has a unique potential for safety and high performance, but the database requires substantial improvement in order to identify and develop a satisfactory material composition. Significant improvements are needed in the basic properties, and several key material issues such as thermal conductivity improvement, joining and hermeticity must be resolved. It was judged premature to adopt such a material for Demo, which was assumed to have a relatively near-term schedule given the small R&D effort on this material in U.S.

Ferritic steel has the largest database, and hence the smallest uncertainty in its performance. However, as with all materials, behavior after long-term operation in a fusion environment is highly uncertain. The features of ferritic steel which cause the greatest concern are its restricted temperature window, which limits the maximum achievable thermal conversion efficiency, and its loss of ductility. It is not clear how one would operate a high-power device with potentially brittle materials. Economic studies indicate that the lower cost of steel (as compared with vanadium alloy) does not completely offset the effects of lower power density and lower thermal conversion efficiency.

Vanadium offers significant advantages in its high temperature and high thermal performance capability, and its low activation. The combination of V and Li is particularly unique in material chemistry, offering good compatibility up to very high temperatures. The primary concerns with vanadium alloy, besides the obvious concerns over their behavior in a fusion neutron environment, are its high cost and liquid metal MHD effects (including the need for and feasibility of insulating coatings). Minimization of vanadium in the shield and external systems, together with lifetime extension and/or recycling is an important cost-reduction strategy. The absence of an established industrial base is also an important consideration, but not one of the top-level requirements as elaborated earlier. Due to its greater ultimate potential for attractive commercial power plants and a development path which appears practical within a 25-year time-frame, the combination of Li breeder/coolant and vanadium-alloy structure was chosen as the first design concept to undergo full system design and analysis in Starlite.

Superconducting magnet design options also were assessed. Several fault situations were analyzed in order to assess the necessary modifications in the design. Maintenance

and configurational issues place demanding constraints on the position and shape of TF coils. In one scheme, proposed for ARIES-I, one TF coil is replaced along with its fusion core module. This step requires a separate dewar/cryostat for each coil. Two schemes for dewar/cryostat system for the toroidal field system were investigated to assess the possibility of removing a TF coil during the maintenance operation. It was found that a separate dewar/cryostat requires substantial additional insulation in the inboard leg of the TF coils, making this option costly. In another maintenance scheme, proposed for ARIES-IV and PUSLAR, an entire sector is remove radially in between the TF coils (the outer leg of TF coils has to be extended outward). Several structural designs were investigated to assess the feasibility of having large access ports in the outboard side. Preliminary analysis indicates TF coil structure can be designed to allow for large access ports.

REFERENCES

[1] D. Smith *et al.*, "Blanket Comparison and Selection Study," Argonne National Laboratory report ANL/FPP/TM-122 (1984).

[2] F. Najmabadi, R. W. Conn, *et al.*, "The ARIES-I Tokamak Fusion Reactor Study—The Final Report," UCLA report UCLA-PPG-1323 (1991); also, R. W. Conn, F. Najmabadi, *et al.*, "ARIES-I: A Steady-State, First-Stability Tokamak Reactor with Enhanced Safety and Environmental Features," *Proc. 13th Int. Conf. on Plasma Phys. and Controlled Nucl. Fusion Research,* Washington, D.C. (Oct. 1990), International Atomic Energy Agency, Vienna (1991) 659.

[3] F. Najmabadi, R. W. Conn, *et al.*, "The ARIES-II and -IV Second-Stability Tokamak Fusion Power Plant Study—The Final Report," UCLA report UCLA-PPG-1461 (to be published); also, F. Najmabadi, R. W. Conn, *et al.*, "Directions for Attractive Tokamak Reactors: The ARIES-II and ARIES-IV Second-Stability Designs," *Proc. 14th Int. Conf. on Plasma Phys. and Controlled Nucl. Fusion Research,* Würzburg, Germany (Oct. 1992), International Atomic Energy Agency, Vienna (1993) 295.

[4] R. L. Klueh, *Proc. IEA Working Group Mtg. Ferritic/Martensitic Steels,* Sun Valley, Idaho (June 24, 1994).

[5] M. Dalle Donne, L. Anzidei, H. Kwast, F. Moons, and E. Proust, "Status of EC Solid Breeder-blanket Designs and R&D for DEMO Fusion Reactors," *Fusion Eng. Des.,* **27** (1995) 319-336.

[6] L. Giancarli, G. Benamati, S. Malang, A. Perujo, E. Proust, and J. Reimann, "Overview of E.U. Activities on DEMO Liquid Metal Breeder Blankets," *Fusion Eng. Des.,* **27** (1995) 337-352.

[7] R. L. Klueh and D. J. Alexander, "Embrittlement of Cr-Mo Steels after Low Fluence Irradiation in HFIR," *J. Nucl. Mater.,* **218** (1995) 151-160.

[8] R. L. Klueh, Ji-Jung Kai. and D. J. Alexander, "Microstructure-Mechanical Properties Correlations of Irradiated Conventional and Reduced-Activation Martensitic Steels," in *Fusion Materials Semiannual Progress Report for the Period Ending March 31, 1994,* U.S.-D.O.E. report DOE/ER-0313/16 (1994).

[9] L. A. El-Guebaly, C. G. Bathke, and the ARIES Team, "Cost-Effective Shield Designs for Environmentally Attractive Fusion Power Plants," *Fusion Tech.* **30**, Dec. 1996, 1058.

[10] C. Baker *et al.*, "STARFIRE - A Commercial Tokamak Fusion Power Plant Study," Argonne National Laboratory report ANL-FPP-80-1 (1980).

[11] R. O'Dell *et al.*, "User's Manual for ONEDANT: A Code Package for One-Dimensional, Diffusion-Accelerated, Neutral Particle Transport," Los Alamos National Laboratory report, LA-9184-M (1982).

[12] D. L. Henderson and O. Yasar, "DKR-ICF: A Radioactivity and Dose Rate Calculation Code Package," University of Wisconsin Fusion Technology Institute report UWFDM-714 (1987).

[13] F. M. Mann and D. E. Lessor, "REAC*3 Nuclear Data Libraries," *Proc. Int. Conf. on Fusion Nuclear Data,* Forschungszentrum Julich, Germany (May 13-17, 1991).

[14] "Standards for Protection Against Radiation," Nuclear Regulatory Commission, 10CFR part 20 (1975).

[15] H. Y. Khater, "WDR: A Code for Rad-waste Classification," unpublished.

[16] "Licensing Requirements for Land Disposal of Radioactive Waste," Nuclear Regulatory Commission, 10CFR part 61, *Federal Register*, **FR 47** (1982) 57446.

[17] S. Fetter, E. T. Cheng and F. M. Mann, "Long Term Radioactive Waste from Fusion Reactors: Part II," *Fusion Eng. Des.,* **13** (1990) 239.

[18] T. Lechtenberg, C. Dahms, and H. Attaya, "An Assessment of Magnetic Effects in Ferromagnetic Martensitic Steels for Use in Fusion Machines," *Proc. Topical Conf. Ferritic Alloys for use in Nuclear Energy Technologies,* Snowbird, Utah (June 19-23, 1983) 179.

[19] "GA TNS Project," General Atomics report GA-A15100 (1978).

[20] W. R. Becraft and P. J. Reardon, "Scope and Status of the U.S.A. Engineering Test Facility Including Relevant TFTR Research and Development," *Proc. 8th Int. Conf. on Plasma Phys. and Controlled Nucl. Fusion Research,* Brussels, Belgium (July 1980), International Atomic Energy Agency, Vienna (1981) 563.

[21] B. Badger *et al.*, "UWMAK-1, A Wisconsin Toroidal Fusion Reactor Design," University of Wisconsin report UWFDM-68 (1973)..

[22] B. Badger *et al.*, "UWMAK-III," University of Wisconsin report UWFDM-150 (1979)..

[23] D. Ehst *et al.*, "Tokamak Power Systems Study-FY 1986: A Second Stability Power Reactor," Argonne national Laboratory report ANL/FPP/86-1 (1987).

[24] F. Najmabadi, R. W. Conn, R. A. Krakowski, K. R. Schultz, D. Steiner, and the TITAN Research Group, "The TITAN Reversed-Field-Pinch Reactor Study—The Final Report," University of California Los Angeles, General Atomics, Los Alamos National Laboratory, and Rensselaer Polytechnic Institute, University of California Los Angeles report UCLA-PPG-1200 (1990); also, F. Najmabadi, R. W. Conn, R. A. Krakowski, K. R. Schultz, D. Steiner, and the TITAN Research Group, "Engineering and Physics of High-Power-Density, Compact, Reversed-Field-Pinch Fusion Reactors: The TITAN Study," *Proc. 15th Symp. Fusion Technol. (SOFT),* Utrecht, the Netherlands (Sept. 1988), *Fusion Technology 88*, A. M. Van Ingen, A. Nijsen-Vis, H. T. Klippel, Eds., North-Holland, Amsterdam (1989) 1779.

[25] Wong, C. P. C. *et al.*, "A Robust Helium-cooled Shield/Blanket Design for ITER," *Proc. IEEE 15th Symp. on Fusion Eng.,* Hyannis, MA (Oct. 1993), IEEE No. 93CH3348-0, IEEE, Piscataway, NJ (1994).

[26] E. Salpietro, "Reactor models for Safety and Environmental Assessment of Fusion Power (SEAFP)," *Proc. U.S./Japan Workshop on Fusion Power Plants,* Kyoto University, Japan (Mar. 13-17, 1995) Japan Atomic Energy Research Institute report 07-100 (1995).

[27] M. Dalle Donne *et al.*, "European DEMO BOT Solid Breeder Blanket," Kernforschungszentrum, Karlsruhe report KfK5429 (1994).

[28] K. Natesan, C. B. Reed, and R. F. Mattas, *Fusion Eng. Des.,* **27** (1995).

[29] A. Tobin and G. Busch, *J. Nucl. Mater.,* **141-143** (1986) 604.

[30] C. F. A. Cotton and G. Wilkenson, *Advanced Inorganic Chemistry,* 3rd Edition, Interscience Publishers (1972).

[31] M. Satou, "Status of V-Ti-Cr-Si (Al, Y) alloy development," *Proc. IEA Workshop Vanadium Alloys for Fusion,* Salem, OR (June 1994).

[32] Marshall, T. D. and Cadwallader, L.C., "In-Vessel ITER Tubing Failure Rates for Selected Materials and Coolants," Idaho National Engineering Laboratory report EGG-FSP-10928 (1994).

[33] C. P. C. Wong, "Analysis Supporting BOTOS Helium Related Coolant Tasks, Revision 1, with minor changes in attachment 2.2," General Atomic memo (Aug. 10, 1993) unpublished.

[34] R. A. Gardner, "Laminar Pipe Flow In a Transverse Magnetic Field with Heat Transfer," *Int. J. Heat Mass Transfer,* **11** (1968) 1081-1083.

[35] M. Dalle Donne, "Comparison of the Performance of 1000 MWe GCFR's with Two and Three-dimensional Roughnesses on the Fuel Rods," *Proc. 5th GCFR Specialist Mtg.,* Wurenlingen, Switzerland (May 14-16, 1979), OECD-NEA Coordinating Group on Gas-Cooled Fast Reactor Development (1979).

[36] S. Kakac *et al.*, *Handbook of Single-Phase Convective Heat Transfer,* John Wiley & Son (1987).

[37] "Detail of the ITER Outline Design Report, The ITER Machine," ITER TAC-4 Meeting (Jan. 10-12, 1994).

[38] J. Brooks, Argonne national Laboratory, personal communication (April 1994).

[39] "U.S. Design Support Study for the ITER Divertor," ITER report ITER/US/93/IV-PF-3 (Oct. 1993).

[40] W. R. Wampler, "Post Exposure RBS Analysis of DiMES sample 70," personal communication (Jan. 1995).

[41] D.A. Greene, D.C. Gaubatz and K.R. McMurtrie, "Leak Location in a Double Wall Tube Steam Generator," *Proc. 2nd Int. Conf. Liquid Metal Technology in Energy Production,* Richland, Washington.

[42] D. L. Smith *et al.*, "U.S. Contribution, 1994 Summary Report, Task T12: Compatibility and Irradiation Testing of Vanadium Alloys," ITER report ITER/US/95/IV MAT 10 (1994).

[43] A. A. Tavassoli, "Assessment of Austenitic Stainless Steels," *Fusion Eng. Des.,* **29** (1995) 371-390.

[44] J. Wareing and A. A. Tavassoli, "Assessment of Martensitic Steels for Advanced Fusion Reactors," *Proc. SMiRT-13,* Porto Alegre, Brazil (Aug. 13-18, 1995).

[45] F. A. Garner and R. J. Puigh, "Irradiation Creep and Swelling of the Fusion Heats of PCA, HT-9 and 9Cr-1Mo Irradiated to High Neutron Fluences," *J. Nucl. Mater.,* **179-181** (1991) 577-580.

[46] D. L. Smith, R. F. Mattas, and M. C. Billone, "Fusion Reactor Materials," in B. R. T. Frost (Ed.), *Nuclear Materials,* Vol. 10B, Chap. 10 (1994) pp 243-340.

[47] A. P. Colleraine, General Atomics, personal communication (July 1995).

[48] G. J. Butterworth, K. A. McCarthy, G. R. Smolik and C.B.A. Forty, "Safety and Environmental Aspects of Vanadium Alloys," *J. Nuc. Mater.,* **212-215** (1994) 667-672.

[49] S. Malang, H. U. Borgstedt, E. H. Farnum, K. Natesan, and I. V. Vitkovski, "Development of insulating coatings for liquid metal blankets," *Fusion Eng. Des.,* **27** (1995) 570-586.

[50] J. H. Park and T. F. Kassner, "CaO Insulator Coating and Self-Healing of Defects on V-Cr-Ti Alloys in Liquid Lithium System," *J. Nucl. Mater* **233-237**, 476 (1996).

[51] H. Moriyama, S. Tanaka, D.K.Sze,J.Riemann, and A Terlain, "Tritium Recovery from Liquid Metals," *Fusion Eng. Des.,* **28** (1995) 226-239.

[52] V. A. Maroni, R. D. Wolson, and G. G. Staahl, "Some Preliminary Considerations of a Molten Salt Extraction Process to Remove Tritium from Liquid Lithium Fusion Reactor Blankets," *Nucl. Technol.,* **25** (1975) 83.

[53] A. Radovinsky, Massachusetts Institute of Technology, Plasma Fusion Center, private communication (1995).

[54] R. D. Pillsbury, "SOLDESIGN User's Manual," Massachusetts Institute of Technology report PFC-RR-65 (1991).

[55] J. Feng, Massachusetts Institute of Technology, Plasma Fusion Center, private communication (1993).

[56] G. A. Slack, "Thermal Conductivity of Ice," *Phys. Rev. B,* **22** (1980) 3065.